RUPRECHT-KARLS-UNIVERSITÄT HEIDELBERG

Hans Patrick Eckert

The Mu3e Tile Detector

Dissertation

HD-KIP-15-08

KIRCHHOFF-INSTITUT FÜR PHYSIK

INAUGURAL - DISSERTATION
zur
Erlangung der Doktorwürde
der
Naturwissenschaftlich - Mathematischen
Gesamtfakultät
der Ruprecht - Karls - Universität
Heidelberg

vorgelegt von
Dipl.-Phys. Hans Patrick Eckert
aus Heidelberg

Tag der mündlichen Prüfung: 06.05.2015

The Mu3e Tile Detector

Gutachter: Prof. Dr. Hans-Christian Schultz-Coulon
Prof. Dr. Peter Fischer

Abstract

The Mu3e experiment is designed to search for the lepton flavour violating decay $\mu^+ \to e^+e^+e^-$ with a sensitivity of one in 10^{16} decays. An observation of such a decay would be a clear sign of physics beyond the Standard Model. Achieving the targeted sensitivity requires a high precision detector with excellent momentum, vertex and time resolution. The *Mu3e Tile Detector* is a highly granular sub-detector system based on scintillator tiles with Silicon Photomultiplier (SiPM) readout, and aims at measuring the timing of the muon decay products with a resolution of better than 100 ps.
This thesis describes the development of the Tile Detector concept and demonstrates the feasibility of the elaborated design. In this context, a comprehensive simulation framework has been developed, in order to study and optimise the detector performance. The central component of this framework is a detailed simulation of the SiPM response. The simulation model has been validated in several measurements and shows good agreement with the data. Furthermore, a 16-channel prototype of a Tile Detector module has been constructed and operated in an electron beam. In the beam tests, a time resolution up to 56 ps has been achieved, which surpasses the design goal. The simulation and measurement results demonstrate the feasibility of the developed Tile Detector design and show that the required detector performance can be achieved.

Zusammenfassung

Das Ziel des Mu3e Experiment ist es nach dem leptonzahlverletzenden Zerfall $\mu^+ \to e^+e^+e^-$ mit einer Sensitivität von Eins zu 10^{16} zu suchen. Der Nachweis eines solchen Zerfalls wäre ein klares Indiz für Physik jenseits des Standardmodells. Um die angestrebte Sensitivität zu erreicht, wird ein hochpräziser Detektor mit exzellenter Impuls-, Vertex- und Zeitauflösung benötigt. Ein Hauptbestandteil des Experiments ist der *Mu3e Tile Detektor*, der darauf ausgelegt die Ankunftszeit der Myon-Zerfallsprodukte mit einer Genauigkeit von unter 100 ps zu messen. Der Tile Detektor ist ein fein segmentiertes Hodoskop, besteht aus Szintillatorkacheln die mit Silizium-Photomultipliern (SiPMs) ausgelesen werden.
In dieser Arbeit wurde das Konzept des Tile Detektors entwickelt und getestet. Hierfür wurden umfangreiche Simulationsstudien durchgeführt, um das Ansprechverhalten des Detektors zu studieren und zu optimieren. Ein zentraler Bestandteil der Simulation ist die Modellierung des Ansprechverhaltens der SiPMs. Die Simulation wurde in mehreren Messungen überprüft und zeigt eine gute Übereinstimmung mit den Messdaten. Des Weiteren wurde ein Prototyp einer Detektoreinheit mit 16 Kanälen aufgebaut und dessen Ansprechverhalten mit Hilfe eines Elektronenstrahls gemessen. In den Teststrahlmessungen wurde eine Zeitauflösung von bis zu 56 ps erreicht. Die durchgeführten Messungen und Simulationsstudien zeigen, dass das entwickelte Detektorkonzept den Anforderungen im Mu3e Experiment genügt und dass die angestrebte Genauigkeit erreicht werden kann.

Contents

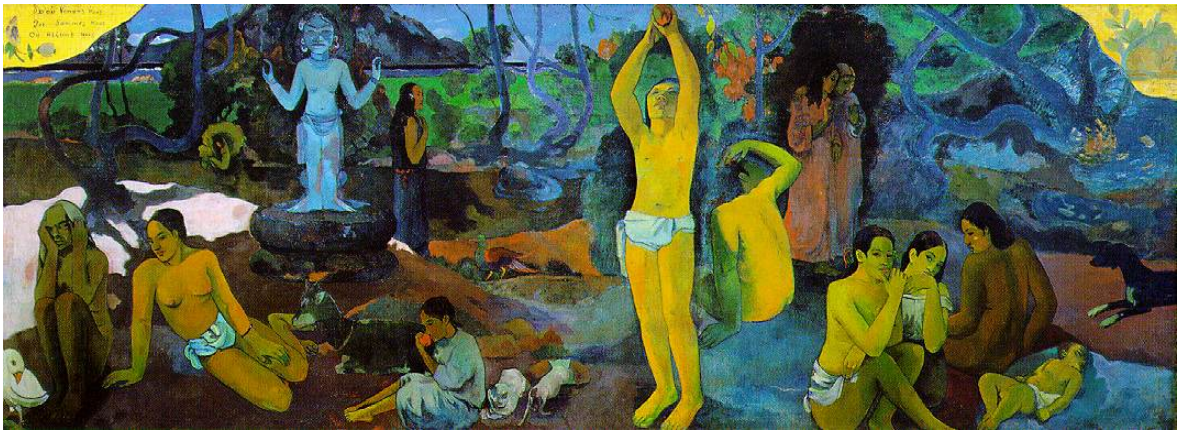

Where Do We Come From? What Are We? Where Are We Going? (Paul Gauguin, 1897) [1]

1. Introduction

Where Do We Come From? What Are We? Where Are We Going? These fundamental questions about the meaning of life, which Paul Gauguin posed in his painting of the same title, are amongst the oldest questions of mankind. From a modern scientific point of view, these questions can be interpreted as the questions about the origin and evolution of our universe and the laws of nature that govern the matter it is made of. These issues are closely linked to the physics of the elementary particles and their fundamental interactions, which are described by the *Standard Model* of particle physics. The building blocks of this theory are sketched in Figure 1.1. The interactions between the elementary particles are mediated by the so-called *gauge bosons*: the photon (γ), which mediates the electromagnetic force, the $W^{\pm}$ and Z bosons, which mediate the weak force and the gluons (g), which are the force carriers of the strong force. The gravitational force is not included in this theory, since so far there is no conclusive way to incorporate the framework of general relativity into the quantum field theory describing the physics of elementary particle. However, the gravitational interaction is significantly weaker than the other forces and is irrelevant for particle physics experiments.
The building blocks of the visible matter in the universe are elementary *fermions*. The fermions are grouped into *leptons* and *quarks*, according to their charge quantum numbers (electric charge, weak isospin and color charge), and are arranged in three generation, according to their mass. The six quarks (up, down, strange, charm, top, bottom) carry electric charge and weak isospin, as well as color charge. Consequently, they participate in all three interactions described in the Standard Model. The six leptons (electron, electron neutrino, muon, muon neutrino, tau, tau neutrino) do not carry color charge and therefore do not interact via the strong force. The three neutrinos only carry weak isospin and hence only interact via the weak force, while the three charged leptons (electron, muon, tau) also couple to photons.
The masses of the fermions and $W^{\pm}$ and Z bosons are generated via the Higgs mechanism. This mechanism involves a massive scalar particle, the Higgs boson.
Over the last decades, the Standard Model has been tested in great detail by various experiments and describes the experimental data with outstanding precision. With the discovery of a Higgs boson at the Large Hadron Collider (LHC) in July 2012, the last missing particle of the Standard Model has been found. However, there are several theoretical arguments and experimental observations which strongly suggest that the Standard Model is an incomplete theory and that there has to be physics *beyond the Standard Model* (BSM), in the following also referred to as *New Physics*. Besides the obvious shortcoming, that gravity cannot be incorporated, there are several cosmological observations that cannot be explained by the Standard Model. For instance, only about 5 % of the energy density of the universe arises from Standard Model particles. The remaining energy density is attributed to dark energy (≈69 %) and dark matter (≈26 %) [3], for which the Standard Model does not provide a good candidate particle. Furthermore, the Standard Model does not include a mechanism which can explain the asymmetry of matter and antimatter observed in the universe. Besides the strong evidence for the Standard Model being an incomplete theory, so far there is no experiment which has measured an undisputable signal of physics beyond the Standard Model. Consequently, one of the main quests of experimental particle physics today is the search for New Physics, which is persued by various experiments.

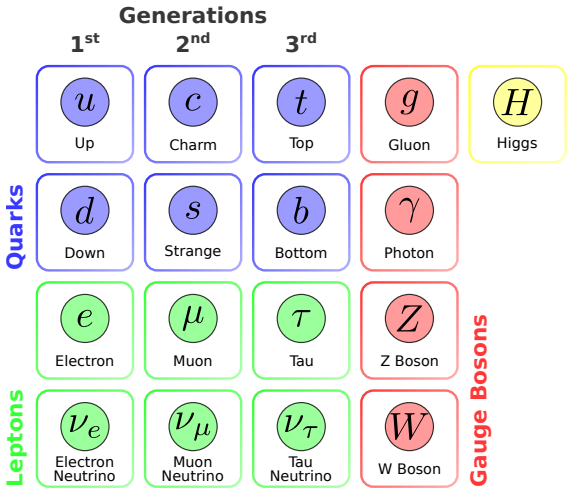

Figure 1.1.: The fundamental particles of the Standard Model of particle physics: the matter particles, which are grouped into three generations of leptons and quarks, the gauge bosons which mediate the electric, weak and strong force, and the Higgs particle. (Figure based on [2].)

There are three fundamentally different and complementary approaches to search for New Physics. The most direct way is to search for resonant production of new particles at collider experiments with an unprecedented center-of-mass energy. The observation of such a resonance would allow to study the properties of a new particle in great detail. However, these direct searches are limited to particle masses smaller than the center-of-mass energy of the collider. Currently, the strongest constraints for New Physics set by direct searches come from proton-proton collisions at the LHC with a center-of-mass energy of up to 8 TeV, which exclude new particles with a mass up to about 1 TeV[1].
Another approach is to search for dark matter particles (WIMPs) in cosmic radiation. Prominent examples are experiments which aim at detecting the recoil of a dark matter particle scattering in a large detector volume, and experiments searching for the products of dark matter annihilation.
The third approach is to search for the footprints of New Physics in precision measurements of Standard Model processes. These indirect searches are sensitive to virtual new particles occurring in loop diagrams, which can cause small deviations from the Standard Model prediction. Since the virtual particles are produced off mass shell, indirect searches are sensitive to particle masses far beyond the energy scale of the studied process and usually exceed the mass reach of direct searches. Although indirect searches can provide a clear indication for New Physics, they only allow for an indirect and usually model dependent determination of the properties of potential new particles, making them complementary to direct searches.
There are a few precision experiments which have observed a significant deviation from the Standard Model prediction. Two prominent examples are the measurement of the anomalous magnetic moment of the muon [4] and the proton radius measurement for muonic hydrogen [5]. However, the uncertainties of the theory prediction, as well as systematic uncertainties of the experiments are still under debate and there is no conclusive interpretation of the results so far. As of today, there is no experiment which has observed an unambiguously signal of physics beyond the Standard Model. Consequently, various new experiments are planned which aim at searching for New Physics with unprecedented sensitivity.
A promising experiment at the precision frontier is *Mu3e*, which is currently being developed.

[1] Assuming a coupling strength similar to the Standard Model couplings.

This experiment aims at searching for the lepton flavor violating decay $\mu^+ \to e^+e^+e^-$, which is strongly suppressed in the Standard Model with a branching ratio of $BR \approx 10^{-54}$. However, many extensions of the Standard Model predict measurable rates for this decay mode. The $\mu^+ \to e^+e^+e^-$ decay thus is an ideal process to search for New Physics at an energy scale far beyond the reach of direct searches, like those at the LHC.
The goal of the Mu3e experiment is to reach a sensitivity of one in 10^{16} muon decays, which exceeds the current exclusion limit by four orders of magnitude. The targeted sensitivity places a demanding challenges on the detector performance. This thesis is devoted to the development the *Mu3e Tile Detector*, which is a sub-detector system of the experiment, providing precise timing information of the muon decay products.

2. The Mu3e Experiment

The Mu3e experiment is designed to search for the lepton flavour violating decay $\mu^+ \to e^+e^+e^-$. The goal of the experiment is to reach a sensitivity on the branching ratio of $BR = 10^{-16}$, which is four orders of magnitude better then the current exclusion limit for this process [6]. The observation of such a decay would be a clear sign for New Physics; a non-observation would strongly restrict the parameter space of many theories beyond the Standard Model.
This chapter gives an outline of the experiment and the underlying theory of the $\mu^+ \to e^+e^+e^-$ decay. Further details can be found in the *Mu3e Research Proposal* [7]. For the sake of convenience, in the following, both electrons (e^-) and positrons (e^+) will be referred to as *electrons* (e).

2.1. Theoretical Background

Each lepton carries a quantum number named *lepton flavour* L_e, L_μ, L_τ, where e, μ, τ refers to the lepton generation, including both the charged lepton and the corresponding neutrino. The lepton flavour assigned to a particle is $L_l = +1$ and $L_l = -1$ for an antiparticle of the respective generation $l = e, \mu, \tau$, and $L_l = 0$ for leptons of other generations $l' \neq l$, as well as non-leptonic particles.
In the Standard Model of particle physics, as originally formulated by Weinberg and Salam, the lepton flavour is a conserved quantity. However, over the last decades, several experiments [8–10] have observed lepton flavour violation (LFV) in the neutrino sector in form of neutrino oscillation. This implies that neutrinos have a non-zero mass, whereas in the original Standard Model neutrinos are massless. In order to incorporate the phenomenon of neutrino oscillation into the Standard Model, neutrino mass terms can be put into the theory in an ad hoc way. However, the mechanism behind the generation of the neutrino masses is still unclear. In the following, the term *Standard Model* refers to this extended version including neutrino masses.
The mixing of the neutrino flavours, which gives rise to the oscillation, is described by a neutrino mixing matrix (PMNS matrix [11, 12]). Although the neutrino mixing angles were measured to be large, no LFV is observed in the charged lepton sector. The reason for this is, that charged lepton flavour violation (CLFV) in the Standard Model is forbidden at tree level and can only be induced by higher-order processes described by loop or box diagrams involving neutrino mixing (see Figure 2.1a as an example). The branching ratio for these processes is determined by the mass ratio between the neutrino and the W boson running in the loop to the fourth power [13]:

$$BR^{SM}_{CLFV} \propto \left| \sum_i = U^*_{\mu i} U_{ei} \frac{\Delta m^2_{i1}}{m^2_W} \right|^2 , \tag{2.1}$$

where Δm^2_{i1} are the neutrino mass-squared differences, and U_{li} are the entries of the neutrino mixing matrix, which describe the amplitude for a neutrino of flavour $l = e, \mu, \tau$ to be found in mass eigenstate $i = 1, 2, 3$. Due to the enormous mass difference[1] between the W boson and the

[1] $m_W = 80\,\text{GeV}$, $m_\nu < 2\,\text{eV}$

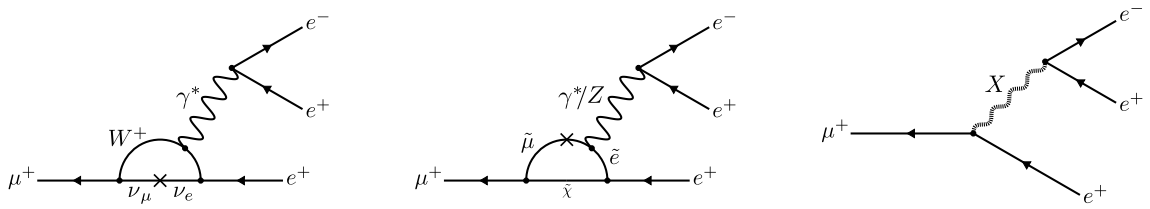

(a) Standard Model **(b)** BSM penguin **(c)** BSM tree level

Figure 2.1.: Feynman diagrams for the lepton flavour violating decay $\mu \to eee$. **(a)** In the Standard Model this decay can be induced via a penguin loop diagram involving neutrino mixing. However, the branching ratio for this process is negligible: $BR^{SM}_{\mu\to eee} \approx 10^{-54}$. **(b)** In extensions of the Standard Model, new heavy particles can occur in the loop process, which significantly enhances the $\mu \to eee$ branching ratio. **(c)** The $\mu \to eee$ decay can also be induced by new particles with lepton flavour violating couplings at tree level.

neutrinos, these processes are suppressed with a branching ratio $BR^{SM}_{CLFV} \approx 10^{-54}$, which for all experimental purposes is equivalent to zero. If new heavy particles are introduced, the branching ratio can be enhanced by many orders of magnitude. Since CLFV is naturally generated in most extensions of the Standard Model, there is a large variety of BSM theories predicting significantly enhanced and experimentally accessible rates for CLFV processes. Examples for such theories are grand unified models [14–16], super-symmetric models [17], left-right symmetric models [18–20] and models with an extended Higgs sector [21]. Consequently, CLFV decays are ideal processes to search for physics beyond the Standard Model and probe energy scales far beyond the reach of direct searches, like at the LHC.

2.1.1. The $\mu \to eee$ Decay

The dominant decay mode of a muon is the lepton flavour conserving decay $\mu^- \to e^-\nu_\mu\overline{\nu_e}$, which has a branching ratio of $BR \approx 100\,\%$. The energy spectrum of the produced electron is described by the so-called *Michel spectrum*, which has been precisely measured by the TWIST collaboration [22]. In the following, this decay mode will be referred to as *Michel decay* (MD). Other decay modes which have been measured are the radiative decay $\mu^- \to e^-\nu_\mu\overline{\nu_e}\gamma$ with a branching ratio[1] of $BR = 1.4 \cdot 10^{-2}$ and the internal conversion (IC) decay $\mu^- \to e^-\nu_\mu\overline{\nu_e}e^+e^-$ with a branching ratio of $BR = 3.4 \cdot 10^{-5}$ [23].
The Mu3e experiment is designed to search for the CLFV decay $\mu^+ \to e^+e^+e^-$. As discussed above, in the Standard Model, such a decay can only occur via neutrino mixing in higher order processes. The dominant process is described by the penguin diagram[2] shown in Figure 2.1a. According to Equation 2.1, the branching ratio of this decay is practically zero ($BR^{SM}_{\mu\to eee} \approx 10^{-54}$). In extensions of the Standard Model, new heavy particles can participate in the loop process, which significantly enhances the branching ratio. Figure 2.1b shows an example of such a diagram for a supersymmetric (SUSY) extension of the standard model. Such loop diagrams, and similar box diagrams, can occur in all models where new particles which couple to electrons and muons are introduced.
In contrast to the Standard Model, lepton flavour violating reactions involving BSM particles can also occur at tree level. An example for such a tree level process is shown in Figure 2.1c, where the propagator X can for example be a heavy new vector bosons (e.g. a Z') or an exotic

[1] This only includes events with a photon energy $E_\gamma > 10\,\text{MeV}$.
[2] A certain class of one-loop processes.

Table 2.1.: Experimental limits on CLFV in muon and tau decays.

Process	Experiment	Branching Ration Limit	Reference
$\mu \to e\gamma$	MEG	$< 5.7 \cdot 10^{-13}$	[25]
$\mu \to eee$	SINDRUM	$< 1.0 \cdot 10^{-12}$	[6]
$\mu Au \to eAu$	SINDRUM II	$< 7.0 \cdot 10^{-13}$	[26]
LFV τ decays	Belle / BaBar	$< \mathcal{O}(10^{-8})$	[27–45]

Higgs particles with lepton flavour violating coupling.
The most general Lagrangian for the $\mu \to eee$ process can be formulated as [24]:

$$\begin{aligned} L_{\mu\to eee} \;=\; -4G_F/\sqrt{2} \cdot [\; & m_\mu A_R \, \overline{\mu_R} \sigma^{\mu\nu} e_L F_{\mu\nu} \\ & + m_\mu A_L \, \overline{\mu_L} \sigma^{\mu\nu} e_R F_{\mu\nu} \\ & + g_1 \, (\overline{\mu_R} e_L) \, (\overline{e_R} e_L) \\ & + g_2 \, (\overline{\mu_L} e_R) \, (\overline{e_L} e_R) \\ & + g_3 \, (\overline{\mu_R} \gamma^\mu e_R) \, (\overline{e_R} \gamma_\mu e_R) \\ & + g_4 \, (\overline{\mu_L} \gamma^\mu e_L) \, (\overline{e_L} \gamma_\mu e_L) \\ & + g_5 \, (\overline{\mu_R} \gamma^\mu e_R) \, (\overline{e_L} \gamma_\mu e_L) \\ & + g_6 \, (\overline{\mu_L} \gamma^\mu e_L) \, (\overline{e_R} \gamma_\mu e_R) \;+\; h.c. \;]. \end{aligned} \tag{2.2}$$

The first two terms are tensor type couplings with the form factors $A_{R,L}$ and are mainly described by loop and box diagrams. The last six terms are scalar type couplings with the form factors $g_{1,2}$ and vector type couplings with the form factors g_{3-6}, which can be interpreted as four fermion contact interactions. In first approximation, these terms describe tree level couplings.

2.2. Experimental Status

Several experiments searching for LFV in the charged lepton sector have been performed over the last decades. The most prominent searches for such processes include the lepton flavour violating muon decays $\mu \to eee$, and $\mu \to e\gamma$, muon to electron conversion in nuclei $\mu N \to eN$ and lepton flavour violating tau decays (see Table 2.1).
The strongest exclusion limit on the decay $\mu \to eee$ is set by the SINDRUM experiment [6], which was operated from 1983 to 1986 at the Paul Scherrer Institute (PSI). The experiment consisted out of a thin, hollow, double-cone shaped target in a $B = 0.33\,\mathrm{T}$ magnetic field, on which muons from a continuous 28 MeV beam were stopped. The detector around the target consisted out of five layers of multi-wire proportional chambers and a trigger hodoscope [6]. The experiment accomplished to set a limit on the branching ratio of $BR_{\mu\to eee} < 1.0 \cdot 10^{-12}$ at 90 % CL. The sensitivity of the experiment was limited by the number of observed muon decays.
The goal of the Mu3e experiment is to reach an ultimate sensitivity of $BR_{\mu\to eee} = 10^{-16}$, which is four orders of magnitude better than SINDRUM.

2.2.1. Comparison to $\mu \to e\gamma$

The $\mu \to eee$ process probed by the Mu3e experiment is to a certain extent related to the lepton flavour violating decay $\mu \to e\gamma$. This decay is mediated by loop processes similar to the one shown in Figure 2.1b, where a real photon is emitted in the loop. Consequently, this decay

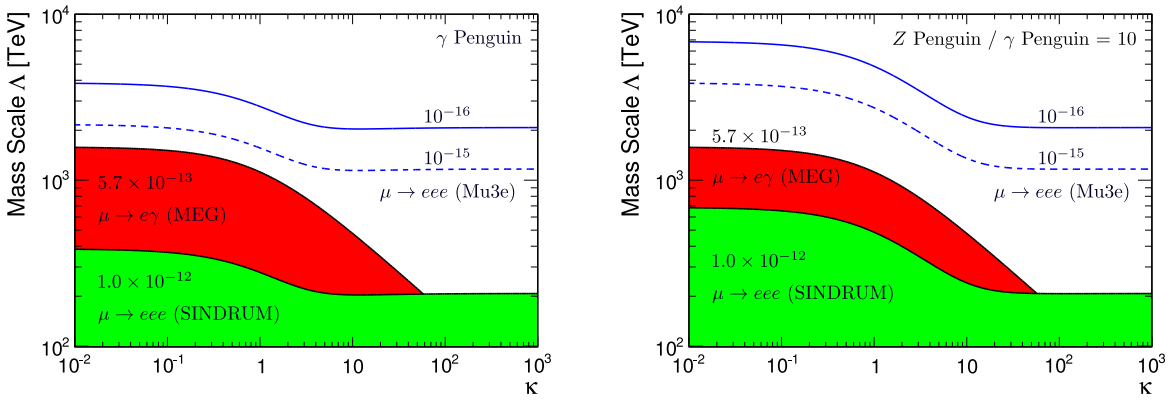

(a) γ penguin only

(b) Z penguin / γ penguin = 10

Figure 2.2.: Limits on the CLFV mass scale Λ as a function of the parameter κ (see Equation 2.4). **(a)** No contribution from Z penguin diagrams is assumed. **(b)** Contribution from Z penguin diagrams are assumed to be ten times larger than the photon contribution. (Updated versions from [7].)

is sensitive to the same physics as the photon penguin induced $\mu \to eee$ decay. Considering only such processes described by photon penguin diagrams, a quasi model independent relation between the $\mu \to e\gamma$ and $\mu \to eee$ decay rate can be derived [7]:

$$\frac{BR_{\mu\to eee}}{BR_{\mu\to e\gamma}} = \frac{\alpha}{3\pi}\left[\ln\left(\frac{m_\mu^2}{m_e^2}\right) - \frac{11}{4}\right] \approx 0.006. \tag{2.3}$$

However, the $\mu \to e\gamma$ decay is not sensitive to Z penguin diagrams, box diagrams and tree level processes, which can be probed with the $\mu \to eee$ decay.
In order to compare the mass scale reach of the two decay modes, a simplified effective Lagrangian with the common energy scale Λ can be formulated, assuming only contributions from photon penguin diagrams (see Figure 2.1b) and tree level diagrams (see Figure 2.1c) [13]:

$$\begin{aligned} L_{LFV} &= \left[\frac{1}{(\kappa+1)\Lambda^2}\; m_\mu \overline{\mu_R}\sigma^{\mu\nu} e_L F_{\mu\nu}\right]_{\gamma\text{ Penguin}} \\ &+ \left[\frac{\kappa}{(\kappa+1)\Lambda^2}\; (\overline{\mu_L}\gamma^\mu e_L)\,(\overline{e_L}\gamma_\mu e_L)\right]_{\text{Tree}}. \end{aligned} \tag{2.4}$$

The parameter κ determines the ratio between amplitudes for the tensor (γ penguin) and vector[1] (tree level) type coupling. Figure 2.2a shows the exclusion limits on the mass scale Λ for $\mu \to eee$ and $\mu \to e\gamma$ derived from the current experimental bounds on the respective branching ratio (see Table 2.1). CLFV processes mediated via penguin diagrams (small κ values) are best constrained by the $\mu \to e\gamma$ decay, while CLFV at tree level (large κ values) is only constrained by the $\mu \to eee$ decay. In this respect, searches for $\mu \to eee$ and $\mu \to e\gamma$ are complementary.
In the limits shown in Figure 2.2a, as well as in Equation 2.3 and Equation 2.4, it is assumed, that only the photon penguin diagram contributes to the dipole amplitude. However, in many models, contributions from Z penguin diagrams significantly enhance the $\mu \to eee$ decay rate by several orders of magnitude [46–52]. Figure 2.2b shows this effect, where the Z penguin contribution is enhanced by a factor ten relative to the photon penguin contribution.

[1] Exemplary a left-left vector coupling is chosen.

The best experimental exclusion limit of $BR_{\mu\to e\gamma} < 5.7 \cdot 10^{-13}$ on the $\mu \to e\gamma$ decay is currently set by the MEG experiment [25], with an analysis of the data taken in 2009 to 2011. This limit is expected to improve with the additional data taken in 2012 and 2013. The final sensitivity of this experiment will be limited mainly by the accidental background rate, where a high energy photon from a radiative muon decay or Bremsstrahlung overlays with a high energy positron from a Michel decay. Therefore, an upgrade of the experiment with improved timing, tracking and energy resolution is currently being prepared, aiming at an order of magnitude improvement in sensitivity.
According to Equation 2.3, the MEG experiment is a factor $BR_{\mu\to e\gamma}/BR_{\mu\to eee} \approx 166$ more sensitive to dipole couplings than searches for $\mu \to eee$, assuming that contributions from Z penguin diagrams can be neglected. Therefore, a sensitivity on the branching ratio of about 10^{-15} is required for Mu3e experiment, in order to be competitive to the MEG experiment, with respect to probing loop induced CLFV (see Figure 2.2a). The aimed sensitivity of 10^{-16} hence would exceed the current mass scale reach of the MEG experiment by one order of magnitude. The mass scale reach for the Mu3e experiment is even larger for models which predict an enhanced $\mu \to eee$ decay rate due to additional Z penguin contributions.

2.3. Experimental Signature

The decay $\mu \to eee$ has several characteristic features distinguishing it from background processes. A sketch of the decay topology in the $r - \phi$ plane is shown in Figure 2.3a. Since $\mu \to eee$ is a prompt decay, the three resulting electron tracks are coincident and have a common vertex. In the Mu3e experiment the muon decays essentially at rest after being stopped in a target. Due to energy and momentum conservation, the energy sum of the electrons consequently equals the muon rest energy and the vectorial sum of the momenta vanishes:

$$E_{tot} = \sum_{i=1}^{3} E_i = m_\mu \tag{2.5}$$

$$\vec{p}_{tot} = \sum_{i=1}^{3} \vec{p}_i = \vec{0}. \tag{2.6}$$

The latter implies that the three tracks lie in one decay plane. In order to precisely measure these decay characteristics and suppress background processes, the Mu3e experiment aims at an excellent momentum, vertex and time resolution.
The maximum electron energy is given by half the muon rest mass: $E_e^{max} = m_\mu/2 \approx 53\,\text{MeV}$. The energy of the lowest energetic electron in the $\mu \to eee$ decay ranges from $E_e \approx 0\,\text{MeV}$ to $E_e = m_\mu/3 \approx 35\,\text{MeV}$. The design goal for the Mu3e experiment is to cover an energy range of $E_e = (10 - 53)\,\text{MeV}$, which corresponds to a signal acceptance of about 50 % for most BSM theories [7].

2.4. Backgrounds

The background processes for the $\mu \to eee$ decay can be categorised into irreducible and accidental (or combinatorial) background.

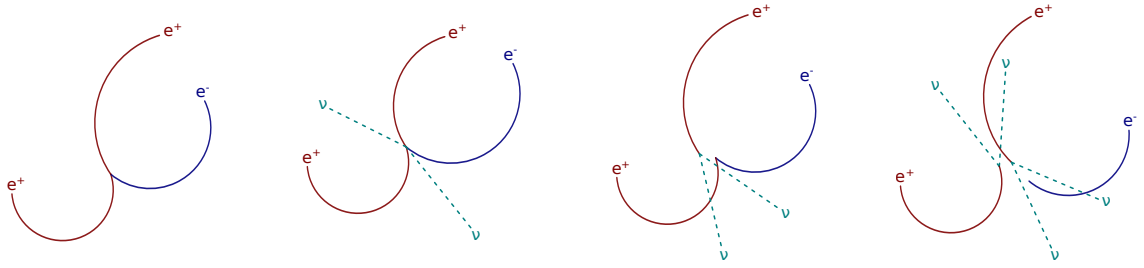

(a) Signal **(b)** Internal Conversion **(c)** 1 MD + e^+e^- **(d)** 2 MD + e^-

Figure 2.3.: Sketch of the signal and background event topologies in the $r-\phi$ plane. **(a)** Signal decay. The three electron tracks are in coincidence originate from a common vertex. **(b)** Irreducible background from internal conversion. This process is distinguished from a signal decay by the energy which is carried away by the neutrinos. **(c & d)** Accidental background from one Michel decays and a e^+e^- pair (c) and two Michel decays and a e^- (d). The accidental background is suppressed by requiring a coincident signal and a common vertex of the tracks.

2.4.1. Irreducible Background

The main irreducible background comes from the internal conversion decay $\mu \to eee\nu\nu$, which has a branching ratio of $3.4 \cdot 10^{-5}$ [23]. The Feynman diagram for this decay is shown in Figure 2.4a, and the event topology is sketched in Figure 2.3b. Similar to the signal decay, the signature of this process features a three-prong signal, which is coincident in space and time. However, internal conversion decays can be distinguished from the $\mu \to eee$ process by the kinematical properties of the electron triplet, due to the energy which is carried away by the neutrinos. Consequently, $\mu \to eee\nu\nu$ events can substantially be suppressed by requiring the momentum sum of the electrons to be zero and the energy sum to equal the muon mass. Figure 2.4b shows the background from internal conversion decays which pass this selection for a certain reconstructed mass resolution. In order to suppress the $\mu \to eee\nu\nu$ background in the 2σ region around the signal to a level of below 10^{-16}, a resolution of $\sigma_{p,3e} \approx 0.5\,\text{MeV}$ is required. This corresponds to a momentum resolution of $\sigma_{p,1e} = 0.5\,\text{MeV}/\sqrt{3} \approx 0.3\,\text{MeV}$ for a single track.
In principle, certain decays of pions, especially $\pi \to eee\nu$ and $\pi \to \mu\gamma\nu$, with the photon converting in the target region, are also indistinguishable from signal events, if the momenta of the decay products match the kinematic properties of the signal. However, the pion contamination in the muon beam is estimated to be in the order of 10^{-12}. Considering the small branching ratio of $BR = 3.2 \cdot 10^{-9}$ for $\pi \to eee\nu$ and $BR = 2.0 \cdot 10^{-4}$ for $\pi \to \mu\gamma\nu$ [23] in combination with the small probability for the decay products to be in the kinematic region of interest, this background can be neglected.

2.4.2. Accidental Background

The accidental background, also referred to as combinatorial background, arises from the accidental overlay of two or three uncorrelated muon decays. This background strongly depends on the muon decay rate, which determines the number of possible track combinations within the considered time interval. In order to have a signal-like event topology with an $e^+e^+e^-$ signature, an additional negatively charged particle (e^-) track has to be present, which is not produced in ordinary μ^+ Michel decays. A signal event can be either faked by a Michel decay overlayed with a coincident e^+e^- pair (1 MD + e^+e^-), or by the overlay of two Michel decays and a single e^- (2 MD + e^-). These two processes are sketched in Figure 2.3c and Figure 2.3d.

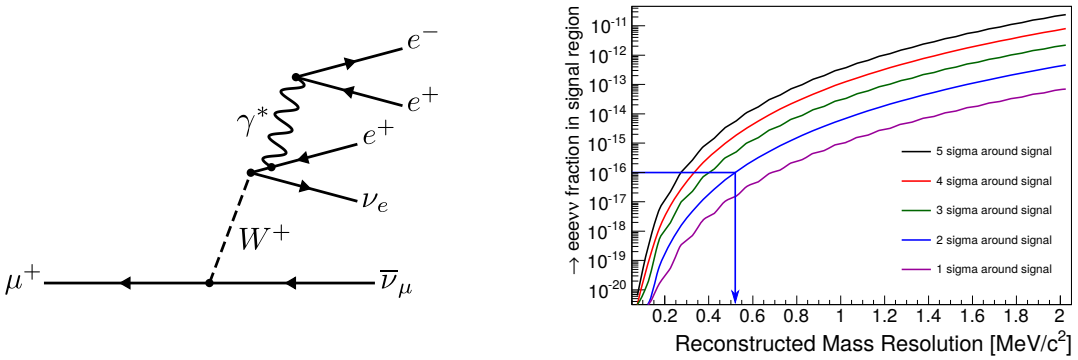

(a) **(b)**

Figure 2.4.: (a) Feynman diagram for the internal conversion decay $\mu \to eee\nu\nu$. **(b)** Branching ratio as a function of the missing energy (Figure taken from [7].)

The dominant production process of e^+e^- pairs is Bhabha scattering of a positron with an electron in the detector material. Other e^+e^- sources are internal conversion decays, where one of the positrons is not reconstructed, and photons which convert in the inner detector region. Photons can be produced either via Bremsstrahlung or in the radiative muon decay $\mu^+ \to e^+\gamma\nu_e\bar{\nu_\mu}$. Events with photon conversions outside the target region can be suppressed by requiring a common vertex of the electron triplet.
Single e^- tracks can be produced by three different processes: Compton scattering of photons in the detector material, wrongly reconstructed tracks to which a negative charge is assigned, or e^+e^- pairs where the positron is not reconstructed, e.g. if the track is outside the detector acceptance.
In order to suppress the accidental background to a level below 10^{-16} per muon decay, a high momentum, vertex and time resolution is required. The accidental background fraction (per muon decay) which passes the kinematic, vertex and timing selection is approximated by the following equation:

$$BG = \begin{cases} \binom{n}{1} \cdot p_x \cdot \eta'_{k_x} \cdot \eta'_v \cdot \eta'_t, & \text{for 1 MD + } e^+e^- \\ \binom{n}{2} \cdot p_x \cdot \eta''_{k_x} \cdot \eta''_v \cdot \eta''_t, & \text{for 2 MD + } e^-. \end{cases} \tag{2.7}$$

The first term describes the number of possible track combinations[1], where n is the average number of tracks in the time frame considered for the event reconstruction, in the following referred to as *readout frame* Δt_{rf}. The average number of tracks is proportional to the muon decay rate R_μ, the geometrical acceptance of the detector A_{geo} and the length of the readout frame: $n = R_\mu \cdot \Delta t_{rf} \cdot A_{geo}$. The second term p_x describes the probability to generate an e^- or e^+e^- pair. Depending on the specific background process x, this ranges from $p_x = \mathcal{O}(10^{-6})$ to $p_x = \mathcal{O}(10^{-4})$. The last three terms $\eta_{v,t,k}$ are the background efficiencies of the vertex, time and kinematic selection criteria. The factor η''_t describes the probability for the three uncorrelated tracks of a 2 MD + e^- event to occur within the a certain coincidence window Δt_{cw}. This probability is given by: $\eta''_t = (\Delta t_{cw}/\Delta t_{rf})^2$. Considering 1 MD + e^+e^- events, the background efficiency η'_t is given by $\eta'_t = \Delta t_{cw}/\Delta t_{rf}$, since the two tracks of the e^+e^- pair are coincident. The factor η'_v (η''_v) is defined by the probability for two (three) uncorrelated tracks to be assigned

[1] For $n < 1$, the binomial coefficient has to be replaced by the probability for at least 2 (1 MD + e^+e^-) or 3 (2 MD + e^-) decays to occur within one readout frame: $\sum_{i=2/3}^{\inf} \left(n^i/i! \cdot \mathrm{e}^{-n}\right)$.

to a common vertex, which depends on the pointing resolution and the vertex reconstruction algorithm. The probability for an accidental $e^+e^+e^-$ triplet to pass the kinematic selection is given by η'_{k_x} (η''_{k_x}), which depends on the specific production process x of the e^+e^- (e^-). A preliminary estimate of the background efficiencies and the resulting accidental background rate for different processes is presented in section 2.5.1.

2.5. Design of the Experiment

One of the main requirements for reaching the targeted sensitivity is a high intensity muon source, allowing to observe well above 10^{16} muon decays within a few years. This can be realised at the PSI facility in Switzerland, which provides a continuous high intensity beam of low energetic muons. The muon beam is powered by a 590 MeV cyclotron with a proton current of 2.2 mA. The protons are brought to collision with a rotating carbon target. In this collision pions (π^+) are produced, which subsequently decay to muons (μ^+). For the Mu3e experiment, low energetic muons are required, which can efficiently be stopped in a thin target inside the detector. These so-called *surface muons* are produced in pion decays at rest, close to the surface of the production target. The resulting muon beam is essentially 100 % polarised and has a momentum of about $p_\mu = 28$ MeV per muon, which is close to the kinematic edge of the pion decay.

The muon beam is transported to a target in the center of the Mu3e experiment. The target is designed as a thin, hollow double cone made out of a polyester film[1] with a length of 100 mm, a radius of 19 mm and a thickness of 75 µm in the upstream direction and 85 µm in the downstream direction[2]. This geometry provides a high stopping efficiency of about 90 %, while keeping the material budget as small as possible to avoid multiple scattering of the electrons.

The target is surrounded by a 2 m long, cylindrically shaped detector system with an outer diameter of about 15 cm, which is located inside a 1 T magnetic field of a solenoid (see Figure 2.5). The detector is longitudinally segmented into five stations. The central station around the target consists out of two double layers of silicon pixel detectors used for particle tracking. The inner double layer close to the target allows a precise determination of the vertex, while the outer double layer provides a large lever arm for precise momentum measurement. In addition to the pixel detector, a scintillating fibre tracker (SciFi), which is located directly inside of the outer pixel layers, provides precise timing information of the particle tracks. The detector is completed by two so-called *re-curl stations* on either side of the central detector segment. These stations are build up of two layers of pixel sensors, identical to the outer double layer in the central detector, surrounding a timing hodoscope made out of scintillator tiles, referred to as *Tile Detector*.

The experiment is designed for a background free measurement, which requires a background suppression below the level of 10^{-16} per muon decay. As discussed in the previous section, this implies an excellent momentum resolution to suppress background from internal conversion decays, and a high vertex and time resolution, in order to suppress accidental background. The momentum will be measured via the particle trajectories in the magnetic field. For the energy range of interest, the limiting factor for the momentum resolution is multiple Coulomb scattering in the detector material. Therefore, a crucial point in the detector design is to reduce the material budget as far as possible. Furthermore, it can be exploited, that due to the relatively low electron energy of $E_e^{max} = 53$ MeV, all tracks will curl back in the magnetic field towards

[1] Mylar®

[2] In the downstream direction the target is slightly thicker, in order to have a similar muon stopping rate in the two cones.

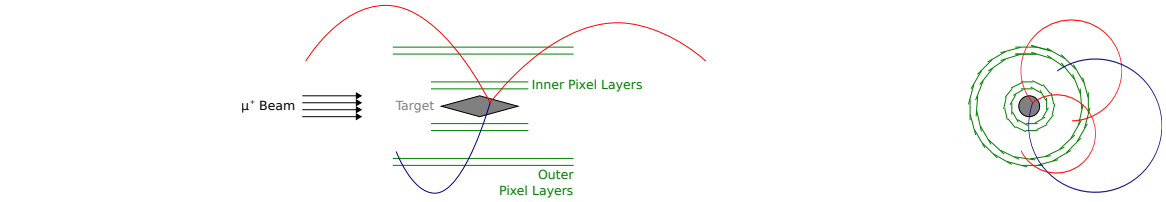

(a) Phase Ia

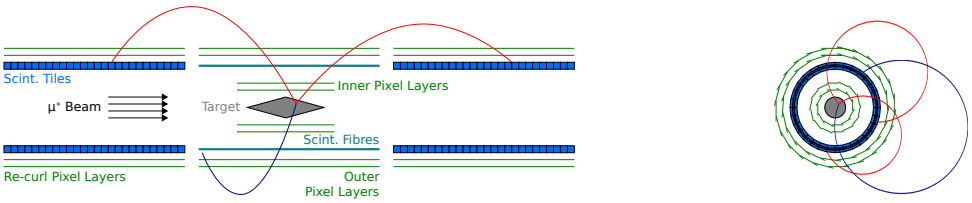

(b) Phase Ib

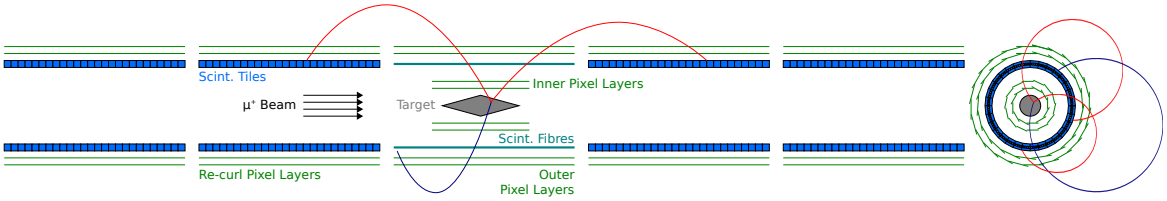

(c) Phase II

Figure 2.5.: Sketch of the Mu3e detector (not to scale) for the different stages of the experiment. (Figure based on [7].)

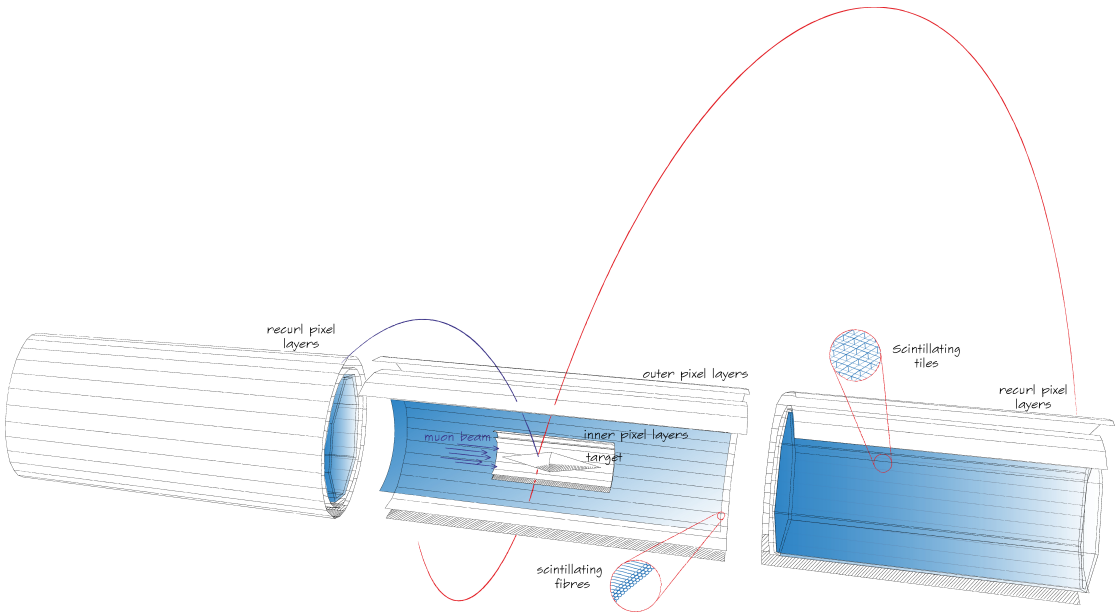

Figure 2.6.: Drawing of the Mu3e experiment in phase Ib. (Figure taken from [53].)

the central axis. This not only provides a large lever arm for the momentum measurement, but also allows to exploit the fact that the effect multiple scattering approximately cancels out after half a turn [7]. Therefore, the detector concept is optimised to measure re-curling tracks, which results in a narrow, long, tube design.
The time resolution which can be achieved with the tracking detector is in the order of $\sigma_t = 10\,\text{ns}$. This is not sufficient to effectively suppress accidental background at high decay rates. Therefore, the tracker is complemented by the two dedicated timing detectors, the SciFi and the Tile Detector, which provide a time resolution in the order of $\sigma_t = 100\,\text{ps}$. In the next section, the three detector systems will be discussed in detail.
The experiment is planned in three stages with increasing sensitivity. Each stage corresponds to approximately one order of magnitude improvement. The detector configuration in the different stages is sketched in Figure 2.5. In the first running phase Ia, the detector only consists out of two double layers of silicon pixel detectors. In this commissioning phase, the experiment is foreseen to run with a moderate muon stopping rate of $2 \cdot 10^7\,\text{Hz}$.
In the second phase Ib, the experiment will be complemented by two re-curl stations (see Figure 2.5b) and the scintillating fibre tracker in the central detector module. The precise timing information gained from the additional timing detectors permits to increase the muon stopping rate to about $1 \cdot 10^8\,\text{Hz}$. This is the maximum rate which can be provided by the current muon beam line at PSI. The additional pixel layers of the two re-curl stations increase the instrumented volume for re-curling tracks. This results in a significantly improved momentum resolution, since about 50 % of the tracks re-curl outside of the central detector station.
In the final phase II, the detector will be completed by two additional re-curl stations to further increase the acceptance for re-curling tracks. In this last phase, the experiment is planned to run with a muon decay rate of about $2 \cdot 10^9\,\text{Hz}$. To reach this intensity, a new muon beam line concept is required, since such a high-intensity beam cannot be provided by the current beam line at PSI, nor by any other facility world-wide. A promising concept for a next-generation high-intensity muon beam is the HiMB[1] project at PSI [54], which is currently being elaborated.

2.5.1. Sensitivity

The ultimate sensitivity of the Mu3e experiment is determined by the number of observed muon decays. This is shown in Figure 2.7a for the three stages of the experiment. In order to reach this sensitivity, the background has to be sufficiently suppressed to achieve a background free measurement.
The irreducible background from internal conversion decays can be rejected with a momentum resolution of 0.3 MeV (see Figure 2.4b), which is the design goal for the pixel detector. The suppression of the accidental background requires a vertex resolution of about $\sigma_v \approx 200\,\mu\text{m}$ and a time resolution of about $\sigma_t \approx 100\,\text{ps}$ in addition. Table 2.2 shows a preliminary estimate for the accidental background per muon decay for different processes (see section 2.4.2), which is determined via Equation 2.7. Here, a coincidence window of $\Delta t_{cw} = 250\,\text{ps}$ and a readout frame of $\Delta t_{rf} = 50\,\text{ns}$ is assumed. This results in a background efficiency of the timing selection of $\eta_t' = 5 \cdot 10^{-3}$ and $\eta_t'' = 2.5 \cdot 10^{-5}$. For the vertex selection, this factor is estimated to be about $\eta_v' = 10^{-4}$ and $\eta_v'' = 10^{-6}$, respectively. Depending on the specific process, the background efficiency of the kinematic selection ranges from $\eta_{k_x} = 10^{-6}$ to $\eta_{k_x} = 10^{-9}$.
The most critical background arises from the overlay of a Michel decay with an e^+e^- pair from Bhabha scattering. The contribution from mis-reconstructed tracks is currently not known, however it is expected to be negligible. Figure 2.7b shows the number of background events

[1] High Intensity Muon Beam

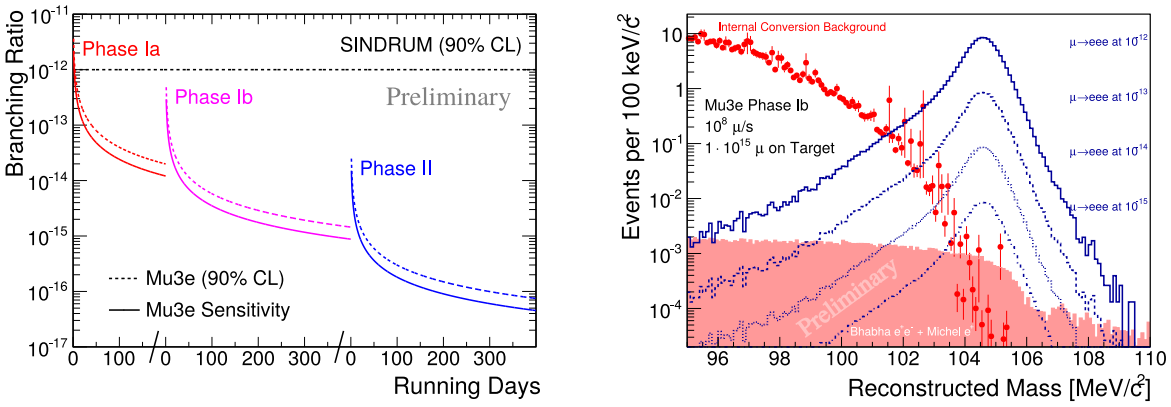

(a) **(b)**

Figure 2.7.: (a) Projected sensitivity and limit (90 % CL) of the Mu3e experiment as a function of the running time. (Reprint from [7].) **(b)** Expected number of background events from internal conversion decays and Bhabha scattering together with potential signal events for phase Ib. The background contamination in the signal region is well below the targeted signal sensitivity. (Reprint from [53].)

Table 2.2.: Preliminary estimate of the accidental background contribution per muon decay. The dominant background is given by the overlay of a Michel decay (MD) with an e^+e^- pair from Bhabha scattering. The contribution from mis-reconstructed tracks is currently not known; however it is expected to be negligible.

Parameter	Phase Ia	Phase Ib	Phase II
1 MD + e^+e^- (Bhabha)	$3 \cdot 10^{-15}$	$5 \cdot 10^{-16}$	$6 \cdot 10^{-16}$
1 MD + e^+e^- (Rad.)	$1 \cdot 10^{-16}$	$2 \cdot 10^{-17}$	$2 \cdot 10^{-17}$
1 MD + e^+e^- (IC)	$4 \cdot 10^{-18}$	$6 \cdot 10^{-19}$	$7 \cdot 10^{-19}$
2 MD + e^- (Bhabha)	$2 \cdot 10^{-16}$	$1 \cdot 10^{-18}$	$3 \cdot 10^{-17}$
2 MD + e^- (Rad.)	$3 \cdot 10^{-18}$	$2 \cdot 10^{-20}$	$5 \cdot 10^{-19}$
2 MD + e^- (IC)	$1 \cdot 10^{-18}$	$8 \cdot 10^{-21}$	$8 \cdot 10^{-20}$
2 MD + e^- (Compton)	$6 \cdot 10^{-18}$	$4 \cdot 10^{-20}$	$9 \cdot 10^{-19}$
2 MD + e^- (Mis-Rec.)	n.k.	n.k.	n.k.

from internal conversion and Bhabha scattering together with potential signal events for a data taking period of about 100 days in phase Ib. It can be seen, that for the targeted detector resolution, the expected background is reasonably below a signal with $BR = 10^{-15}$, which is the targeted sensitivity for in phase Ib. For phase II, the current estimation of the Bhabha related background is of the same order as the targeted sensitivity. However, it should be noted that the detector design and event reconstruction is still being optimised; especially the vertex reconstruction is being refined, in order to improve the background suppression.

2.6. Detector Systems

2.6.1. Pixel Tracker

The tracking detector is a crucial part of the experiment, which has to provide a momentum resolution better than $\sigma_{p,1e} = 0.3\,\text{MeV}$ and a vertex resolution of $\sigma_v \approx 200\,\mu\text{m}$, in order to

suppress the background processes. The detector consists out of two 36 cm long double layers of silicon pixel sensors, which are based on the High-Voltage Monolithic Active Pixel (HV-MAPS) technology [55]. Due to the high bias voltage operation ($V > 50\,\mathrm{V}$) of these sensors, the ionisation charges are collected via drift, in contrast to conventional pixel sensors where the charge is collected mainly by diffusion. This results in significantly faster signals and thus provides high rate capability and a time resolution of better than $\sigma_t = 15\,\mathrm{ns}$. The small depletion zone also allows for thinning of the sensors down to 50 µm, which corresponds to a radiation length of $X/X_0 < 0.1\%$ per layer. As discussed above, this minimal material budget is crucial for achieving the desired momentum resolution. The individual sensors have a size of $2 \times 2\,\mathrm{cm}^2$ and consist out of roughly 62 500 pixels with a size of about $80 \times 80\,\mu\mathrm{m}^2$. The intrinsic sensor resolution associated with the pixel size is negligible compared to the contribution from multiple scattering. Each pixel contains an integrated readout circuit, which processes the signals and sends out zero suppressed digitised hit information. The hit information of the sensors is read out with a 20 MHz clock; all hits in a readout cycle are thus grouped into 50 ns readout frames. The sensors are mounted on strips of 50 µm thin polyimide film[1], which serve as a support structure and host aluminium traces for the electrical connection of the sensors. The heat produced by the sensors will be dissipated via a flow of gaseous helium.

2.6.2. Timing Detectors

In addition to the tracking system, there are two scintillator-based timing detectors, which will be added to the experiment in phase Ib. Due to the high muon decay rate in phase Ib and II, precise timing information of the particle tracks is required, in order to suppress combinatorial background.

Scintillating Fibre Tracker

The SciFi is located directly below the outer pixel layers and is planned to consist out of three layers of scintillating fibres with a diameter of 250 µm and a length of 36 cm. The scintillation light is read out at both ends of the fibres using Silicon Photomultiplier arrays, which cover several fibres per channel. Currently also the option of single fibre readout is studied, which would allow for a better time resolution and lower occupancy.
The goal for this detector is to achieve a time resolution of a few times 100 ps, while keeping the material budget as low as possible, in order to minimise multiple scattering. Besides the suppression of accidental background, the timing information gained by the SciFi is also important for the track reconstruction[2]. The time resolution provided by the SciFi detector alone is not sufficient for the desired suppression of accidental background. Therefore, a second complementary timing detector is required.

Tile Detector

The Tile Detector is located in the re-curl stations inside of the pixel layers. It is a scintillator hodoscope detector, which is segmented into roughly 10 000 small tiles. Each scintillator tile is coupled to a Silicon Photomultiplier for the readout of the scintillation light. The basic principle of scintillators and Silicon Photomultipliers are discussed in chapter 3 and chapter 4. For the fraction of particles which reach the re-curl stations (roughly 50 %), the Tile Detector is the

[1] Kapton®
[2] For example, the charge, i.e. the direction of the circular motion, of tracks which re-curl in the target region can only be determined via the time-of-flight information.

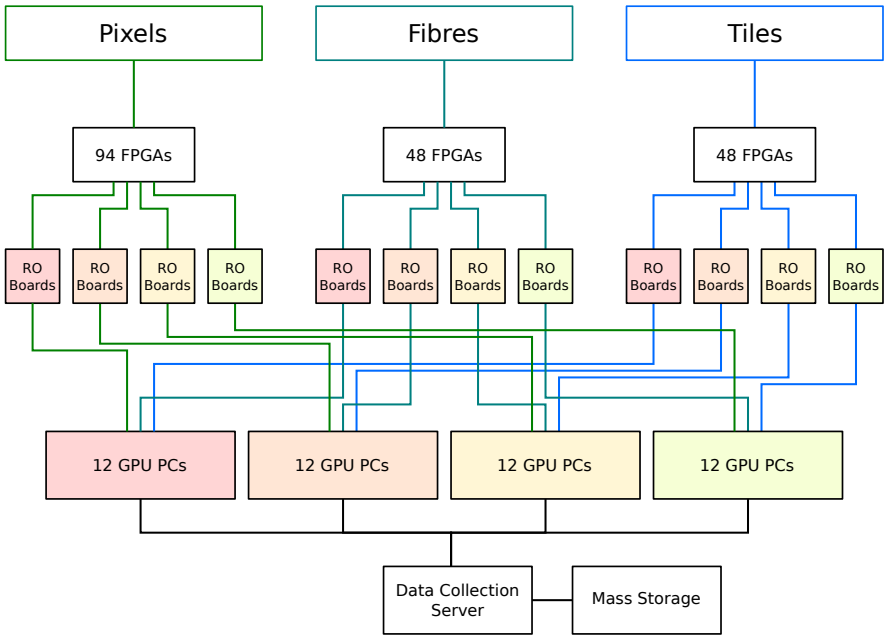

Figure 2.8.: Mu3e readout scheme for phase Ib.

last detector system in the particle trajectory. The measurement of the momentum is thus already completed once the particle reaches the Tile Detector, which allows for a much thicker scintillator layer compared to the SciFi. Consequently, a significantly better time resolution of below $\sigma_t = 100\,\text{ps}$ can be achieved.
Within the scope of this thesis, the concept of the Tile Detector has been developed and tested for feasibility. A detailed description of the detector design is presented in section 6.2.

2.6.3. Data Acquisition

In contrast to other experiments, the Mu3e is designed without a hardware trigger; instead, the data from all detector systems is continuously send to the data acquisition system (DAQ). As depicted in Figure 2.8, the DAQ consists out of three stages: front-end FPGAs inside the detector, readout boards in the periphery of the detector and a computer cluster.
In the first stage, the data from the three detector systems is collected by the front-end FPGAs. The data is grouped in $\Delta t_{rf} = 50\,\text{ns}$[1] readout frames, which corresponds to the readout cycle of the pixel sensors. From the FPGAs, the data is transmitted to the readout boards outside of the detector via optical fibres. The main task of the readout board is to buffer the data and distribute it via optical links to the individual PCs of the computer cluster, where the events are reconstructed. The data flow is organised in such a way, that the full event information, i.e. the data from all sub-system within a certain time slice, is send to one PC. On the PCs, the events are reconstructed and selected using high-performance graphics processing units (GPUs).

[1] Currently also shorter frames of 25 ns are considered.

3. Introduction to Scintillators

Scintillators are amongst the oldest detectors for ionising radiation and are still used in a large variety of applications. In particle physics experiments, scintillators are commonly used for calorimetric applications, tracking and triggering purposes, as well as fast timing measurements. The basic detection principle is based on the conversion of the energy deposited by ionising radiation in the scintillator material into luminescence light, which then can be measured by a photo-sensor. The number of photons emitted in this process is proportional[1] to the deposited energy.
There is a large variety of different scintillator materials, including solids, liquids and gases. A distinction is drawn between organic and anorganic scintillator materials, which exhibit different scintillation mechanisms and have different fields of application. This chapter will focus on organic scintillators, which are utilised in the Mu3e Tile Detector and SciFi tracker. For the sake of completeness, also anorganic scintillators are briefly discussed.
The content of this chapter for the most part represents a summary of [56, 57].

3.1. Anorganic Scintillators

Anorganic scintillators are usually anorganic crystals, typically with an addition of a trace amount of dopants. Due to their usually high atomic number, anorganic scintillators are commonly used for the detection of gamma rays or in monolithic calorimeters. There is a large variety of crystal materials with different scintillation properties. A few of the most common ones are listed in Table A.1. Amongst the various scintillator materials, there are several different scintillation mechanisms, which are all based upon the crystallin state of the material and the resulting electronic band structure. In the following, the most common mechanism is discussed, which relies on impurities in the crystal structure, so-called *luminescence centers* or *activator states*. These impurities are produced via a small amount of dopants added to the material.

[1] Plastic scintillators typically feature a small non-linearity in the response for high energy densities. This quenching effect is described by *Birks law* [56].

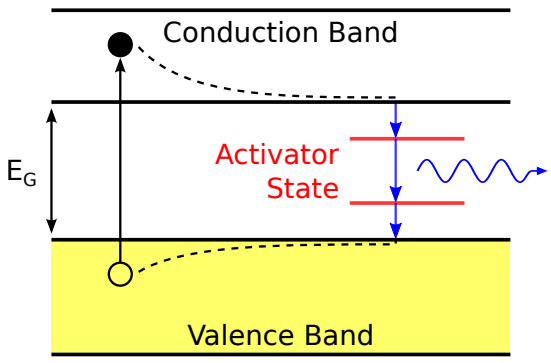

Figure 3.1.: Scintillation mechanism in anorganic scintillators. The activator states are created by doping of the crystal. (Sketch based on [58].)

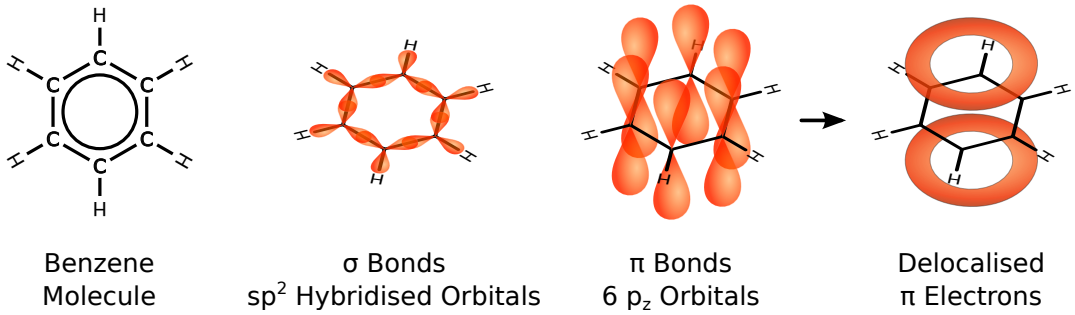

Figure 3.2.: Structure of a benzene molecule. Six carbon atoms with sp^2 hybridised orbitals form a planar ring. The π electrons in the p_z orbitals are delocalised. (Sketch based on [59].)

The scintillation mechanism is sketched in Figure 3.1. The process is triggered by the energy deposition of an ionising particle in the scintillator material. The deposited energy can excite electrons from the valence band to the conduction band and thus create free electron-hole pairs. The electrons (holes) lose energy via elastic scattering with phonons and end up in the lowest energetic state in the conduction (valence) band. At this point an electron-hole pair can form a long-lived exciton state, which can freely move through the scintillator. At the luminescence centers, the exciton state can decay, i.e. the electron-hole pair recombines, under the emission of scintillation light. Since this transition occurs in several steps via the intermediate activator states, the energy of the emitted photons is smaller than the band gap energy. This prevents instantaneous reabsorption of the photons.

3.2. Organic Scintillators

Organic scintillators are based upon aromatic hydrocarbon compounds, which contain benzene ring structures. The structure of a benzene molecule (C_6H_6) is shown in Figure 3.2. The molecule consists out of six carbon atoms with sp^2 hybridised orbitals, which form a planar ring. The electrons in the sp^2 orbitals of a carbon atom form three covalent σ bonds with two other carbon atoms and one hydrogen atom. The remaining electrons in the p orbitals are delocalised, which means that they are distributed equally between the six carbon atoms.
The luminescence properties of organic scintillators are based upon the energy levels of these delocalised electrons, which are sketched in Figure 3.3a. The energy levels are divided into singlet states S_i, with the ground state S_0, and triplet states T_i. The vibrational and rotational degrees of freedom of the molecule lead to a splitting of these levels into a series of sub-levels ν_i. The energy deposited by an ionising particle can lift π electrons from the ground state to a vibrational sub-level of an excited single state $S_{i>0}$. Transitions from S_0 to a triplet state T_i are highly suppressed due to spin conservation. The excitation process typically commences from the lowest vibrational level ν_0 of the ground state S_0, which is highest populated. Since the transition between different states occurs on a very fast timescale, the internuclear distance associated with the different bonding orbitals does not change. This is known as the Franck-Condon principle, which is sketched in Figure 3.3b. Consequently, the excitation is most likely to result in a higher vibrational state $\nu_{i>0}$. The exited state will quickly transition to the vibrational ground state of S_i, since the timescale for thermal relaxation of a vibrationally excited molecule is much shorter than the timescale for the radiative transition back to S_0. The vibrational ground states of $S_{i>1}$ usually overlap with higher vibrational states of the adjacent state S_{i-1} (see Figure 3.3a). This allows for a very efficient non-radiative transition between adjacent states $S_{i>0}$ and S_{i-1},

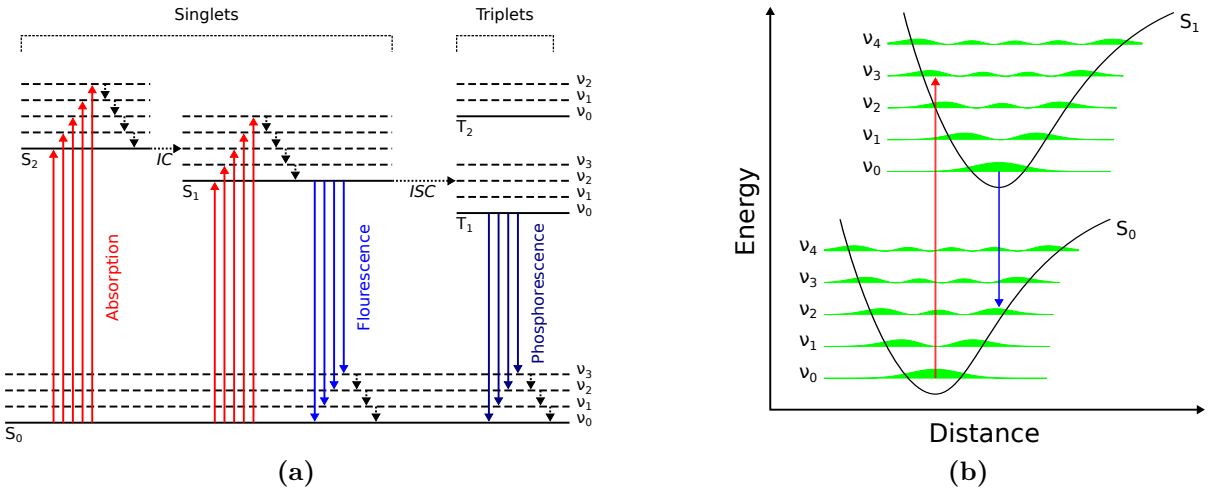

(a) (b)

Figure 3.3.: (a) Fluorescence and phosphorescence mechanism in an organic scintillator. The luminescence is based on the energy levels of a π electron system of the organic molecule. (Figure based on [60].) **(b)** Sketch of the Franck-Condon principle: since the transitions occur on a very fast timescale, the internuclear distance associated with the different bonding orbitals does not change. In combination with the fast thermal relaxation of higher vibrational states, this is responsible for the Stokes shift. (Figure based on [61].)

which known as *internal conversion* (IC). Due to the fast thermal relaxation and the internal conversion process, any excited state will quickly relax to the lowest vibrational state of S_1 before the radiative transition to S_0 via the emission of a fluorescence photon. This fluorescence process typically occurs on a timescale in the order of a few nanoseconds.
Similar to the initial excitation, the fluorescence process will result in a vibrationally excited state of S_0 and subsequently relax to the lowest vibrational level (see Figure 3.3b). The fast thermal relaxation, both after absorption and emission, leads to a shift of the fluorescence spectrum relative to the absorption spectrum (see Figure 3.4b), which is referred to as *Stokes Shift*. This effect prevents the immediate reabsorption of the photon, thus making the scintillator transparent to its fluorescence light. At room temperature, not only the lowest vibrational state of S_0 is populated but also levels with slightly higher vibrational energy, which leads to an overlap of the emission and absorption spectrum.
Besides the primary fluorescence mechanism, there are two suppressed luminescence processes: *phosphorescence* and *delayed fluorescence*. The basis for phosphorescence is a spin-dependent internal conversion transition from a singlet to a triplet state, referred to as *intersystem crossing* (ISC). The radiative transition from the T1 state to the ground state violates spin conservation and is thus suppressed. This results in a much longer time scale of about 10^{-4} s to 10 s for the phosphorescence process. The long lifetime of the triplet states also allows for back-transitions to a singlet state, which gives rise to a delayed fluorescence emission.
In contrast to anorganic scintillators, the scintillation mechanism in organic scintillators does not depend on the crystallin state but is present in solid, liquid and gaseous form. There are three widely used types of organic scintillators: crystalline, liquid and plastic scintillators. While crystalline scintillators consist out of a single molecule, e.g. Anthracene ($C_{14}H_{10}$), liquid and plastic scintillators are mixtures of several different organic scintillating materials. The most prominent and versatile type are plastic scintillators, which are commonly used in particle physics experiments, e.g. for calorimetry[1], particle tracking and timing applications.

[1]Due to their low, density plastic scintillators are primarily used in sampling calorimeters.

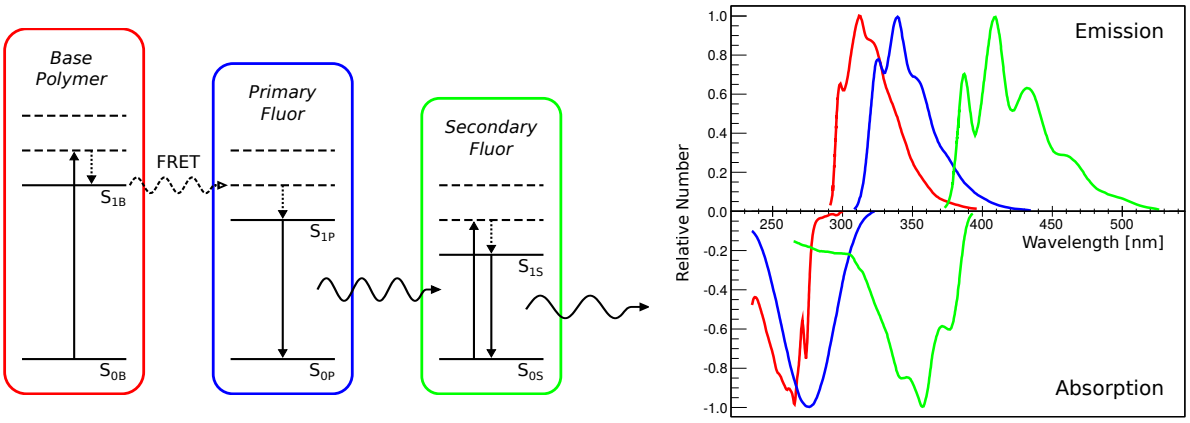

(a) **(b)**

Figure 3.4.: (a) Energy transfer in a plastic scintillator with a primary and secondary fluorescence emitter. The transition between the excited base molecules and the primary fluor proceeds predominantly via Förster resonance energy transfer (FRET); the transition from the primary to the secondary fluor is radiative. **(b)** Absorption and emission spectra of the different plastic scintillator components. The base polymer is Polyvinyl Toluene (red curves), the primary fluor is p-Terphenyl (blue curves) and the secondary fluor is POPOP (green curve). (Data taken from [62].)

3.2.1. Plastic Scintillators

Plastic scintillators are based upon organic polymers, usually with aromatic rings as pendant groups. Commonly used base materials are Polyvinyl Toluene (PVT) and Polystyrene (PS). In contrast to crystalline scintillators, which are difficult to machine and to grow in large size, these materials can be produced in almost any desired shape and possess a high degree of durability. The plastic base material by itself usually has a low fluorescence quantum efficiency (typically below 20 %) and exhibits a rather large overlap of the emission and absorption spectrum, which results in a low light yield. In order to increase the light output, a second scintillator material with high quantum efficiency, referred to as *primary fluor*, is suspended in the polymer base material. This is typically accomplished via dissolution of the fluor in the base material prior to the polymerisation process.
Since the primary fluor concentration is typically in the order of $\mathcal{O}(1\,\%)$, the probability for direct excitation by the incident ionising radiation is negligible. Consequently, an efficient energy transfer from the excited molecules of the base material to the primary fluor molecules is necessary, in order to exploit the high quantum yield of the primary fluor. This can be achieved, if the primary fluor concentration is sufficiently high, so that the average distance between the molecules of the base polymer and the molecules of the fluor is smaller than the wavelength of the fluorescence light. The dominant energy transfer mechanism at such distances is the so-called *Förster resonance energy transfer* (FRET), which is a resonant dipole-dipole coupling (see Figure 3.4a). This process is significantly more efficient and faster than radiative energy transfer.
The fluorescence light of the primary fluor is typically in the UV range, where the detection efficiency of standard photo-sensors is relatively low. In order to match the spectral sensitivity of the photo-detectors, many plastic scintillators contain a secondary fluor in addition, shifting the fluorescence light to the blue spectral region. The concentration of the secondary fluor is typically in the order of $\mathcal{O}(0.01\,\%)$. The low concentration causes the energy transfer from the primary to the secondary fluor to proceed predominantly via radiative interactions. The

Table 3.1.: Properties of different plastic scintillators and Anthracene. (Data taken from [63, 64].)

Scintillator	Base Mat.	ρ [g/cm^2]	τ_r/τ_d [ns]	LightYield [phot./MeV]	λ_{peak} [nm]
Anthracene	-	1.25	- / 30	16000	440
BC404	PVT	1.03	0.7 / 1.8	10400	408
BC408	PVT	1.03	0.9 / 2.1	10000	425
BC418	PVT	1.03	0.5 / 1.4	10200	391
BC420	PVT	1.03	0.5 / 1.5	9700	391
BC422	PVT	1.03	0.35 / 1.6	8400	370

complete energy transfer chain for a plastic scintillator with primary and secondary fluor is sketched in Figure 3.4a.
Table 3.1 lists the main characteristics of the scintillator materials which have been studied for the application in the Mu3e tile detector (see section 6.3). In addition, the properties of Anthracene, which has the highest light output of all organic scintillators, are specified for comparison. All listed plastic scintillators are based on PVT, and therefore have a similar density. However, due to diverse admixtures of primary and secondary fluors, the materials show a different scintillation behaviour. The light yield is in the range between 8400 and 10 400 photons per MeV, which is about (50-65) % of the light yield of Anthracene. The scintillation light is in the blue and near ultraviolet spectral range, with a peak wavelength of $\lambda_{peak} = (370 - 425)$ nm. In contrast to Anthracene, the scintillation process in plastic scintillators is significantly faster, with a rise and decay time $\tau_{r,d}$ in the order of one nanosecond. This makes plastic scintillators well suited for timing applications, like in the Mu3e experiment.

4. Silicon Photomultipliers

Photo-detectors are used in a vast variety of scientific and commercial applications. In experimental particle physics, the two main applications of photo-sensors are the detection of scintillation and Cherenkov light. These applications require sensors which are sensitive to low photon flux.
In general, photo-detectors can be categorised into vacuum based sensors and solid-state detectors based on semi-conducting materials. The most common type of vacuum photo-sensor is the *Photomultiplier Tube* (PMT), which for a long time was uncontested in the area of low photon flux detection. Over the last decade, silicon based solid-state detectors have rapidly advanced and today surpass conventional PMTs in several aspects.
In the Mu3e experiment, the scintillation light in the Tile Detector and the SciFi is detected by *Silicon Photomultipliers* (SiPMs). This is a state-of-the-art type of solid-state photo-sensor, which has become increasingly popular over the last years. This chapter gives an overview of the working principle and operation parameters of SiPMs.

4.1. History of Development

Over the last decade, significant progress has been made in the development of silicon based photo-sensors, resulting in a large variety of different detector types with steadily increasing performance in terms of photon counting capability and time resolution. In the following section, the photon detection principle of two sensors, the PIN photodiode and the Avalanche Photodiodes, are discussed, which build the basis for the development of SiPMs.

4.1.1. PIN Photodiodes

Although there is a large variety of solid-state photo-detectors with different properties, the underlying working principle is similar for all devices. The photon detection is based on the properties of a *p-n junction*, which is an interface between n-type and p-type semiconductor material, most commonly silicon. Applying a reverse bias voltage, the junction becomes depleted of charge carriers. This so-called *depletion region* acts as the sensitive detector volume. A photon which is absorpt in the semiconductor material can excite an electron from the valence band to the conduction band via the internal photoelectric effect, thus creating a electron-hole pair. If the electron-hole pair is produced in the depletion region, the charges drift in the electric field to the anode and cathode, respectively, generating a photo-current.
One of the simplest types of solid-state photo-sensor utilising this principle is the PIN photodiode. Figure 4.1a shows the schematic structure of such a device. It consists out of a highly doped n^+ and p^+ layer and a layer of intrinsic silicon in between. Due to the intrinsic layer, only a small reverse bias voltage is required to fully deplete the sensor, resulting in a large sensitive volume. An advantage of PIN diodes is the linear response, e.g. the photo-current is directly proportional to the incoming photon flux. Furthermore, the sensor response is not influenced by fluctuations in the operation voltage and temperature, as long as the intrinsic layer is fully depleted. However, PIN diodes are not suited for applications with low photon flux, since there is no internal

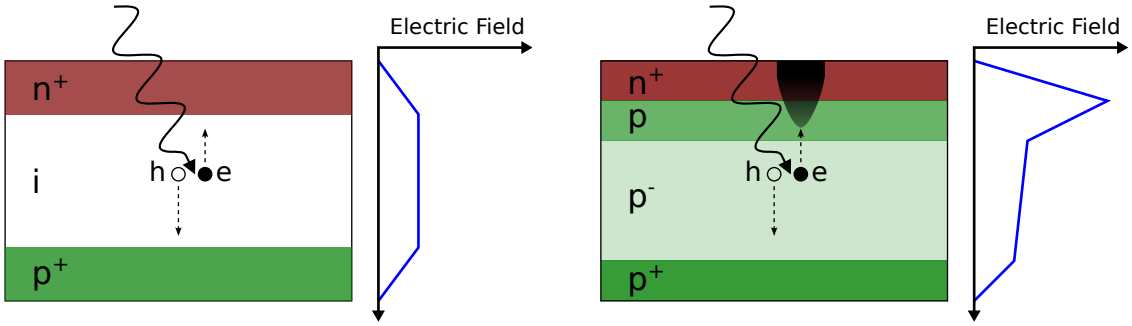

(a) PIN diode **(b)** Avalanche Photodiode

Figure 4.1.: (a) Schematic doping structure of a PIN diode. The sensor consists out a large intrinsic silicon layer in between a heavily doped n^+ and p^+ layer. Photons which are absorpt in the intrinsic layer generate a photo-current. **(b)** Schematic doping structure of an Avalanche Photodiode. Due to the high electric field at the p-n junction, a charge carrier can trigger an avalanche multiplication process via impact ionisation.

amplification mechanism, making the detection of single photons practically impossible.
Another drawback, especially for the application in particle detectors, is the so-called *nuclear counter effect*, which describes the sensor response to ionising radiation. The energy deposition of an ionising particle in silicon is typically in the order of several MeV/cm, which is six orders of magnitude larger than the energy required to create an electron-hole pair. Consequently, ionising radiation can fake large signals, equivalent to several thousand detected photons. In applications where the PIN diode is used to read out scintillation light, this effect can counterfeit a large energy deposition in the scintillator.

4.1.2. Avalanche Photodiodes

One of the main drawbacks of PIN diodes is the missing amplification, which significantly limits the sensitivity to low light levels. This problem is resolved in *Avalanche Photodiodes* (APDs), which feature an internal amplification mechanism allowing for single photon sensitivity.
The schematic structure of such a device is shown in Figure 4.1b. In contrast to PIN diodes, APDs have a high electric field in the depletion layer, which is achieved with a high doping gradient at the p-n junction and a reverse bias voltage of $\mathcal{O}(100\,\mathrm{V})$. In the high electric field, charge carriers gain enough energy to create secondary electron-hole pairs via impact ionisation, which results in an avalanche multiplication process.
The number of secondary electron-hole pairs created per unit length is given by the ionisation coefficient, which is shown in Figure 4.2. This parameter depends on the electic field, charge carrier type and the semiconductor material. For silicon, electrons have a significantly larger ionisation coefficient than holes, which has important consequences for the APD operation.
Conventional APDs are operated with a moderate reverse bias voltage below the breakdown voltage of the diode. In this mode of operation, the avalanche is induced only by electrons. The holes do not contribute to the multiplication process, due to the lower ionisation coefficient. The avalanche therefore only propagates in one direction (towards the anode) and the multiplication process stops once all electrons have left the high field region. The resulting signal is proportional to the initial number of electron-hole pairs; therefore this mode of operation is often referred to as *linear mode*. The avalanche multiplication process in the linear mode operation yields a gain of up to 1000, which allows to detect low light fluxes of a few photons using conventional amplifiers. The signal to noise ratio which can be achieved is limited by fluctuations in the

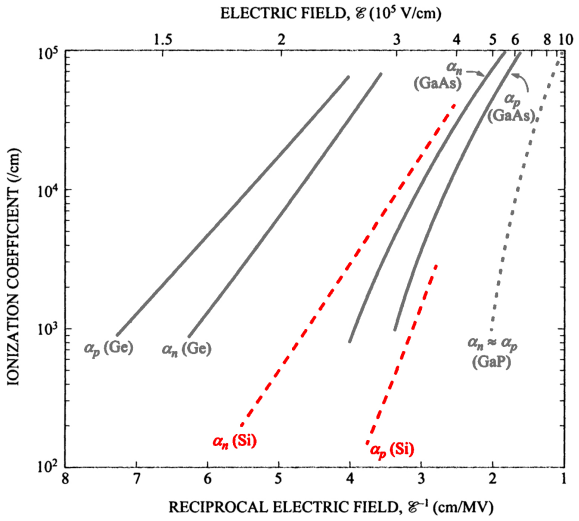

Figure 4.2.: Impact ionisation coefficient for electrons (α_n) and holes (α_p) in different semiconductor materials, as a function of the electric field. (Modified reprint from [65].)

multiplication process, which usually precludes a single photon sensitivity. In the linear mode operation, APDs exhibit the same nuclear counter effect as PIN diodes.

Geiger-Mode APDs

A special type of APD is the so-called *Geiger-mode avalanche photodiode* (G-APD), also referred to as *single-photon avalanche diode* (SPAD). These devices are designed to operate above the breakdown voltage V_{bd} of the diode. In this so-called *Geiger-mode*, the electric field is large enough that also holes do participate in the multiplication process. Consequently, the avalanche propagates in both directions: the electron avalanche towards the anode and avalanche of the holes towards the cathode. This results in a self sustaining multiplication process, which leads to large current flowing through the device. This process is referred to as *Geiger discharge*.
In order to be sensitive to subsequent photons and achieve a finite gain, the avalanche process has to be quenched. The most common and simple quenching mechanism is *passive quenching*, where the photodiode is connected to the bias voltage via a quench resistor of $\mathcal{O}(100\,\mathrm{k\Omega})$. The working principle of this quenching scheme is depicted in Figure 4.3. If no avalanche is in progress, no current is flowing through the quench resistor and thus the full bias voltage is applied on the diode. However, if a Geiger discharge is triggered, the avalanche current causes a voltage drop over the quench resistor $V_q = R_q \cdot I$, which in turn reduces the voltage over the diode $V_d = V_{bias} - V_q$. This negative feedback mechanism causes a steady decrease in the avalanche current, which approaches a final value of:

$$I(t \to \infty) = (V_{bias} - V_{bd})/R_q = V_{ov}/R_q, \tag{4.1}$$

where the so-called *over-voltage* V_{ov} is the difference between the bias voltage V_{bias} and the diode breakdown voltage. If the final current is sufficiently small, the number of charge carriers traversing the high field region can drop to zero, due to statistical fluctuations in the avalanche process. This mechanism efficiently stops the avalanche, if the current is below $I \approx 20\,\mu\mathrm{A}$ [66]. Consequently, the maximum over-voltage for which the avalanche can reliably be quenched is $V_{ov}^{max} = R_q \cdot 20\,\mu\mathrm{A}$, which is typically in the order of a few Volts. After the avalanche has been stopped, the voltage over the diode slowly recharges to its initial value.

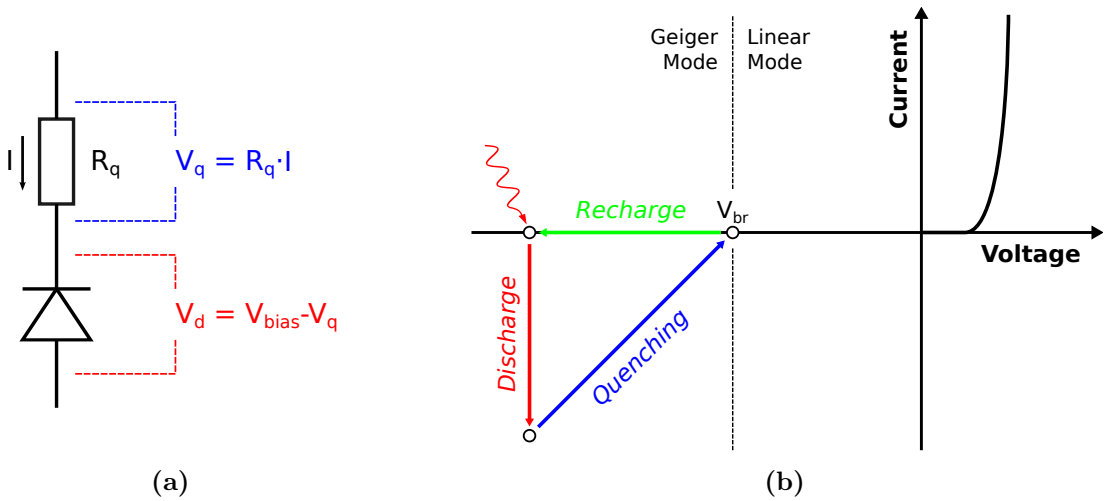

Figure 4.3.: Passive quenching in a G-APD. **(a)** Passive quenching circuit: the APD is connected to a high resistance. **(a)** Schematic description of the quenching mechanism: after a Geiger discharge, the voltage over the p-n junction V_d drops down to the breakdown voltage, which stops the avalanche process. After this, the voltage recharges to the applied bias voltage.

An alternative quenching mechanism is *active quenching*. This approach relies on an external electrical circuit which can sense the Geiger discharge and subsequently reduces the bias voltage below the breakdown voltage, in order to stop the multiplication process. After a short time, the bias voltage is reset to the initial value. This method allows for a fast avalanche stopping and device recovery, which is advantageous for high rate applications. However, the implementation is significantly more complex compared to the passive quenching scheme.
The main advantage of G-APDs is the high gain of $\mathcal{O}(10^6)$ which can be achieved in the avalanche process. A major limitation arising from the Geiger-mode operation is the limited photon counting capability, since the signal produced in a Geiger discharge does not depend on the number of detected photons. This limitation has been resolved by the development of the Silicon Photomultiplier.

4.2. SiPM Working Principle

One of the latest developments in the field of solid-state photo-detectors are multi-pixel G-APDs, also referred to as *Silicon Photomultipliers*[1] [69] (SiPM). Due to various advantageous properties, these sensors have become increasingly popular in high energy physics, as well as medical imaging and astrophysical applications [70–72].
Silicon Photomultipliers are pixelated sensors, which consist out of an array of Geiger-mode APDs, each connected to a quench resistor. A simplified equivalent circuit of a SiPM is shown in Figure 4.4b. The typical sensor size ranges from 1 mm^2 to a few 10 mm^2, with a pixel density ranging from 100 to 10 000 G-APDs per mm^2. Figure 4.4a shows an example of a 1 mm^2 device with 400 pixels.
Due to the Geiger-mode operation, each pixel operates as a binary counter, i.e. the pixel signal does not depend on the number of photons which trigger the Geiger discharge. The pixelation of the device allows to detect multiple photons simultaneously, assuming the photons are distributed

[1] There are numerous names for different devices, such as SiPM, MPPC, PPD, SSPM, MRS-APD, AMPD, etc. In this thesis, the name SiPM is used to generically refer to them all.

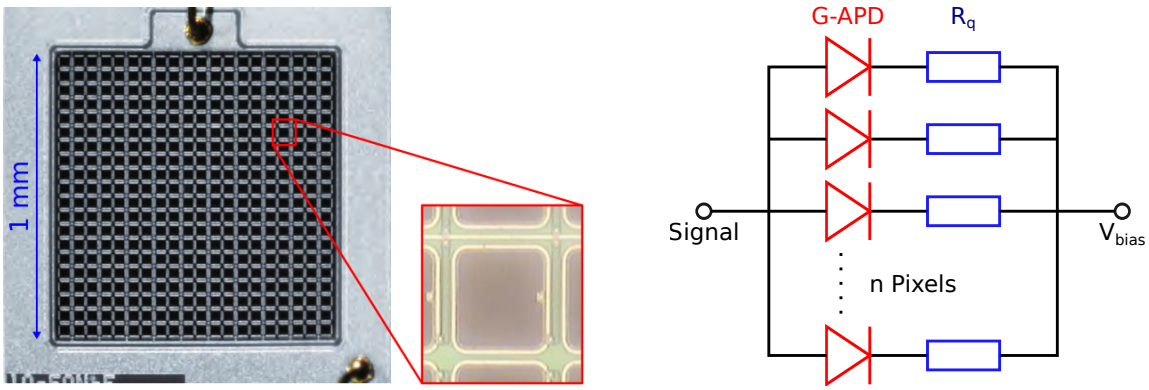

Figure 4.4.: (a) Picture of a SiPM with 400 pixels (MPPC S10362-11-050C) and a magnified view of a single pixel. (Taken from [67,68].) **(b)** Simplified equivalent circuit of a SiPM. The individual G-APDs are connected to a common output over a quench resistor.

over the sensor surface. This resolves one of the main limitations of single G-APDs. Since the individual cells are connected in parallel to a common output (see Figure 4.4b), the signal produced by a SiPM is given by the sum of the individual pixel signals. In first approximation, this signal is proportional to the number of detected photons. A more detailed description of the response is given in section 4.3.

Figure 4.5 shows a typical structure of a SiPM. The avalanche multiplication occurs in a thin region of a few micrometer around the strongly doped n^+-p^+ junction. In this so-called *Geiger region*, the electric field is large enough to support the impact ionisation process for both electrons and holes. A guard ring around the n^+-p^+ structure prevents excessive electrical fields at the edges, which would lead to undesired electrical discharge. The weakly doped p^- layer below the junction enhances the sensitivity to red and infrared light, which can penetrate several ten micrometers deep into the silicon. The electrons and holes created in this layer drift in the low electric field to the electrodes and can trigger an avalanche breakdown when reaching the high field region. This low field region is also referred to as *drift region*.

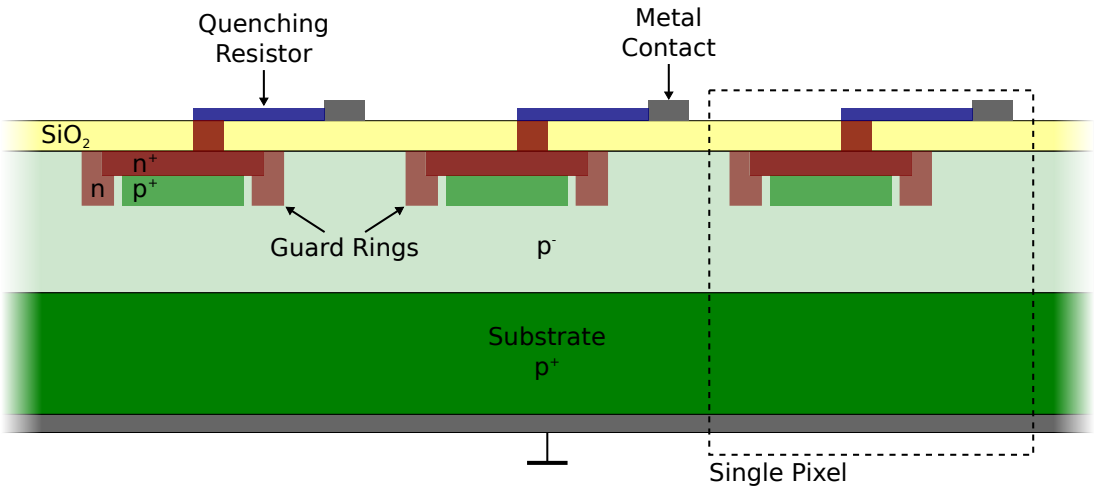

Figure 4.5.: Typical structure of a SiPM. The shown architecture is know as *reach-through structure*. There are several variations of this architecture used in different devices. (Figure based on [73,74].)

There are several variations of the structure shown in Figure 4.5 used in different devices. In particular, a distinction is made between devices with a n-on-p structure, as shown in Figure 4.5, and devices with a p-on-n structure, where the p^+ layer is on top of the n^+ layer. A sketch of the doping structure of the SiPMs[1] which are proposed for the Tile Detector and are used in the measurements presented in the following sections can be found in Figure A.1.
The unique micro-pixel binary counter structure makes the SiPM an excellent photon-counting device, featuring a high photon detection efficiency of up to 50 % and a high gain of $\mathcal{O}(10^6)$, which is similar to the performance of conventional PMTs. Due to the Geiger mode operation, the fluctuations in the avalanche process are small compared to linear mode APDs, which results in an excellent single photon sensitivity. Two major advantage over PMTs are the insensitivity to magnetic fields and the compact dimension of the sensors. These properties make SiPMs well suited for the application in highly granular particle detectors, like the Mu3e Tile Detector. Another advantage of SiPMs is the negligible nuclear counter effect. Due to the Geiger mode operation, an ionising particle traversing a pixel generates the same signal as a single optical photon, independent of the amount of energy deposited in the pixel. For most applications, this additional single pixel signal is negligible. However, there are also some drawbacks, like the limitation in the dynamic range and several noise sources. In the following sections, the properties of SiPMs are discussed in detail.

4.3. SiPM Characteristics

4.3.1. Single Pixel Signal

The signal generated by a single pixel can be determined from the equivalent circuit of the SiPM shown in Figure 4.6b [66, 75]. An APD cell is represented by the pixel capacitance C_{pix}, a voltage source V_{br}, which determines the breakdown voltage, a switch which initiates the Geiger discharge and a resistor R_d, which describes the internal resistance of the avalanche. The physical quench resistor is represented by R_q and the associated parasitic capacitance C_q between the resistor and the APD cell. Considering a single pixel signal, the remaining inactive pixels are described by $C_q^* = C_q \cdot (N-1)$, $C_{pix}^* = C_{pix} \cdot (N-1)$ and $R_q^* = R_q/(N-1)$, where N is the total number of pixels. The stray capacitance introduced by the electrical traces is represented by C_s.
The single pixel signal is in first approximation determined by the components R_q, C_q, C_{pix} and R_d of the active pixel, while the passive components can be neglected. When the avalanche is initiated, which is represented by the closing of the switch, the full bias voltage is applied to the p-n junction. This results in a large transient avalanche current $I(t \to 0) = V_{ov}/R_d$. Due to the passive quenching, the avalanche current will decrease exponentially and approach a final value of $I(t \to \infty) = V_{ov}/(R_d + R_q)$. The time constant of the exponential decrease is given by [76]:

$$\tau_{rise} \approx R_d \cdot (C_{pix} + C_q). \tag{4.2}$$

Once the current is sufficiently small, the avalanche is quenched, as described in section 4.1.2, which abruptly stops the current. Up to the quenching time t_q, the avalanche current is given by [76]:

$$I(t) = [I(t \to 0) - I(t \to \infty)] \cdot \mathrm{e}^{-\frac{t}{\tau_{rise}}} + I(t \to \infty). \tag{4.3}$$

[1] Hamamatsu MPPC

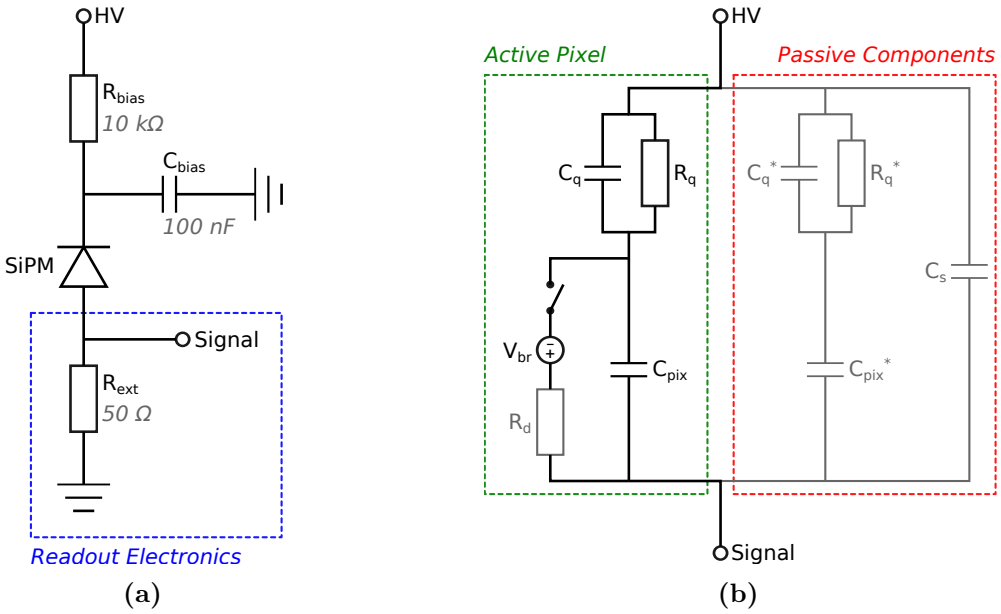

Figure 4.6.: (a) Typical SiPM readout circuit. **(b)** Equivalent circuit diagram of a SiPM for a single firing pixel.

The resulting output charge generated in the Geiger discharge of a single pixel is given by the integral of the avalanche current:

$$\begin{aligned} Q_{pix} &= \int_0^{t_q} I(t)\,dt \\ &\approx \frac{V_{ov}\cdot R_q(C_{pix}+C_q)}{R_d+R_q} + \frac{V_{ov}\cdot t_q}{R_d+R_q} \\ &\approx V_{ov}\cdot(C_{pix}+C_q), \end{aligned} \tag{4.4}$$

where the approximations are based on the assumptions $\tau_{rise} \ll t_q$, $R_d \ll R_q$ and $t_q/R_q \ll C_{pix}$. After the avalanche is quenched, the voltage at the G-APD exponentially recharges to the initial bias voltage with a time constant of [76]:

$$\tau_{rec} = R_q \cdot (C_{pix}+C_q) \approx R_q \cdot C_{pix}, \tag{4.5}$$

which determines the recovery time τ_{rec} of the pixel.
The voltage pulse measured over the load resistance R_{ext} of an external readout circuit (see Figure 4.6a) is characterised by a fast rise time, which in first approximation (neglecting bandwidth limitations) is determined by τ_{rise} and a slow signal tail. For a low input impedance $R_{ext} \ll R_q$, the signal tail can be approximated by [77]:

$$V(t) \approx V_{ov}R_{ext}\cdot\left(\frac{C_{pix}}{\tau_{rec}}\cdot \mathrm{e}^{-\frac{t}{\tau_{rec}}} + \frac{C_q}{\tau_{para}}\cdot \mathrm{e}^{-\frac{t}{\tau_{para}}}\right). \tag{4.6}$$

The first term in the bracket is related to the recovery of the SiPM cell with the time constant τ_{rec}. The second term is introduced by the parasitic capacitance of the pixel C_q. The associated decay constant is $\tau_{para} = R_{ext}\cdot C_{tot}$, where C_{tot} is the total capacitance of the device.

4.3.2. Dynamic Range

The dynamic range of a single SiPM cell is related to the pixel recovery process. After the quenching of an avalanche breakdown, the voltage over the pixel exponentially recharges to its initial value:

$$V_{ov}(\Delta t) = V_{ov} \cdot (1 - \mathrm{e}^{-\frac{\Delta t}{\tau_{rec}}}), \tag{4.7}$$

where Δt is the time interval after the avalanche and $V_{ov} = V_{ov}(t \to \infty)$ is the nominal over-voltage. If a photon is absorpt during this recovery phase, the reduced over-voltage most notably results in a lower detection efficiency and, in case an avalanche is triggered, a reduced gain. In case of simultaneously impacting photons, a single SiPM pixel consequently can only provide binary information, i.e. if at least one photon was detected or not. In order to obtain the photon-counting capability, a high density array of pixels is necessary, which is a key characteristic distinguishing SiPMs from other photo-sensors. If the number of photons N_{phot} impacting the sensor is much smaller than the number of pixels N_{pix}, the probability for several photon to hit the same pixel is small, given a homogenous distribution of the photons. The resulting signal charge thus is in good approximation proportional to N_{phot}. For an increasing number of impacting photons, this proportionality breaks down and the SiPM signal saturates as the number of detected photons approaches N_{pix}. Assuming a homogenous illumination of the sensor with a light pulse duration much shorter than the pixel recovery time and neglecting noise contributions, the number of fired pixels is given by:

$$N_{fire} = N_{pix} \cdot (1 - \mathrm{e}^{-\frac{\mathcal{E}_{pde} \cdot N_{phot}}{N_{pix}}}), \tag{4.8}$$

where $\mathcal{E}_{pde}$ denotes the photon detection efficiency, which is discussed below.

4.3.3. Gain

The gain is defined by the total charge created in the avalanche process. Following Equation 4.4, this is given by:

$$G = \frac{Q_{pix}}{q_e} = \frac{V_{ov} \cdot (C_{pix} + C_q)}{q_e}, \tag{4.9}$$

where q_e is the elementary charge. The gain of a device strongly depends on the pixel size, which is related to the pixel capacitance C_{pix}. For devices with large pixels, gain values in the order of $\mathcal{O}(10^6)$ are achieved.

The charge created in an avalanche is subject to statistical fluctuations σ_G, which primarily originate from cell-to-cell variation in the pixel capacitance and breakdown voltage, as well as fluctuations in the quenching time. These gain fluctuations are often refered to as *excess noise*[1]. The resulting fluctuation of the total signal charge of n firing pixels is given by:

$$\sigma_Q^2 = \sigma_{en}^2 + n \cdot \sigma_G^2, \tag{4.10}$$

where σ_{en} is the electronic noise, which is associated with the SiPM leakage current and the noise of the readout electronics.

The gain fluctuations in the Geiger discharge are intrinsically small compared to photo-sensors with a linear multiplication mechanism. Consequently, SiPMs exhibit an excellent single photon resolution.

[1] There are also other definitions used which include contributions from cross-talk and after-pulses. However, these contributions are not intrinsic and can in principle be corrected for.

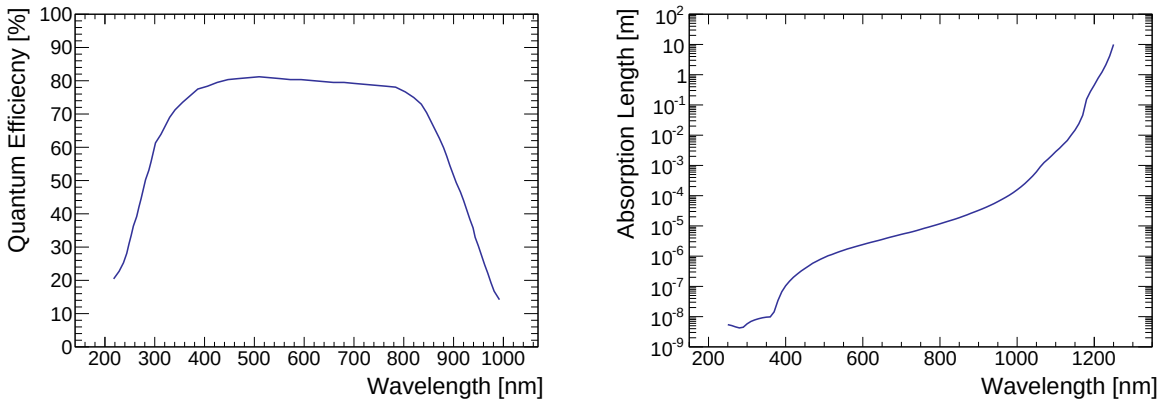

(a) **(b)**

Figure 4.7.: (a) Quantum efficiency of silicon. (Data taken from [78].) **(b)** Photon absorption length in silicon. (Data taken from [79].)

4.3.4. Photon Detection Efficiency

The *photon detection efficiency* (PDE) is one of the key parameters of a photo-sensor. For a SiPM, the PDE can be factorised in the following way:

$$\mathcal{E}_{pde}(\lambda, V, T) = (1 - R(\lambda)) \cdot QE(\lambda) \cdot P_{ff} \cdot P_g(\lambda, V, T), \tag{4.11}$$

where $R(\lambda)$ is the probability for a photon to be reflected off the sensor surface, and $QE(\lambda)$ is the wavelength dependent quantum efficiency of silicon, which is shown in Figure 4.7a. The geometrical fill factor P_{ff} describes the ratio between the sensitive surface and the total area[1] of the sensor. The fill factor is limited by the minimum spacing required between the pixels, which is mainly determined by the guard ring structure. Further limitations arise from the intransparent quench resistors[2], the metal lines on the sensor surface and optical trenches between the cells (see below). Consequently, the fill factor typically scales with the pixel size. For modern devices a fill factor of up to 80 % can be achieved.
The Geiger efficiency P_g describes the probability for a photoelectron to initiate an avalanche breakdown, which depends on the temperature, bias voltage and the photon energy. The latter determines the photon absorption length in silicon, which is shown in Figure 4.7b. Since electrons have a larger impact ionisation coefficients than holes, P_g is larger when the photon is absorpt in the p^+ layer. SiPMs with a n-on-p structure therefore typically have the maximum sensitivity for light in the green or red spectral region, which can penetrate deep enough to reach the p^+ layer. Devices with a p-on-n structure have an enhanced sensitivity to blue/UV light, which is absorpt within a few micrometers and less.

4.3.5. Dark-rate

The dark-rate is defined by the rate of avalanche breakdowns in the absence of light. The two main mechanisms generating the dark-rate are thermal excitation and quantum tunnelling. The process of thermally induced generation of electron-hole pairs is sketched in Figure 4.8a. Electrons from the valence band can be excited to the conduction band via interaction with

[1] Not including the sensor package.
[2] There are novel sensor with (semi-)transparent metal quench resistors.

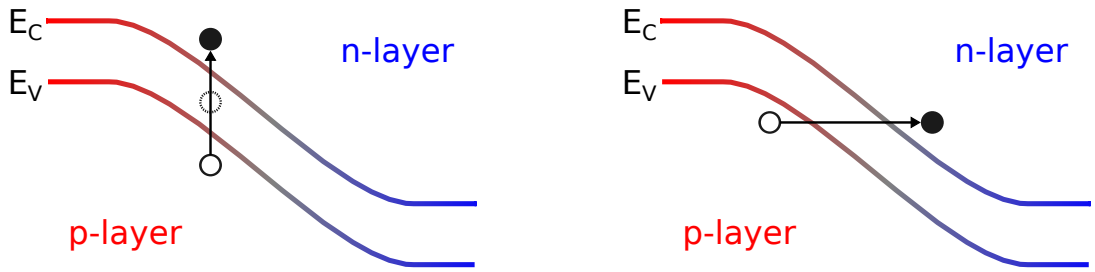

(a) Thermal generation **(b)** Tunnelling assisted generation

Figure 4.8.: Sketch of the two processes generating dark-rate signals. **(a)** An electron-hole pair can be produced via thermal excitation. This process is significantly enhanced by defects in the silicon lattice, which introduce intermediate energy levels in the band gap. **(b)** Generation of an electron-hole pair via quantum tunnelling. The tunnelling probability strongly depends on the electric field strength at the p-n junction.

phonons. This process is significantly enhanced by lattice defects, which introduce intermediate states in between the band gap. The thermally induced dark-rate therefore strongly depends on the purity of the silicon and on the temperature.
The tunnelling assisted electron-hole pairs generation is sketched in Figure 4.8b. Electrons in the p-layer can tunnel across the junction into the conduction band of the n-layer and thus trigger an avalanche. The tunnelling probability strongly increases with the electric field at the p-n junction and therefore is the dominating process at high over-voltage. In contrast to the thermal excitation, the tunnelling process does not depend on the temperature and hence cannot be suppressed by cooling.
In addition to the primary dark-rate pulses generated by thermal and tunnel excitation, secondary pulses from after-pulsing (see below) also contribute to the total dark-rate. In general, the dark-rate scales with the active surface of the sensor. Furthermore, the dark-rate depends on the doping structure of the SiPM. As the Geiger efficiency for electrons is larger than for holes, n-on-p type devices, which usually feature a large p^- drift region, have a higher dark-rate than p-on-n devices with a large n^- drift region. For modern SiPM devices a dark-rate of less than $100\,\mathrm{kHz/mm^2}$ can be achieved.

4.3.6. Optical Cross-talk

The avalanche process is accompanied by the emission of optical photons [80]. The underlying process which generates these photons is not precisely known. Possible mechanisms which are being discussed are the recombination of electron-hole pairs, intra-band transitions and Bremsstrahlung of charge carriers in the high field region. The probability for emission of a photon with sufficient energy to create a secondary electron-hole pair is about $3 \cdot 10^{-5}$ per charge carrier [81, 82]. For a typical gain of 10^6, this results in about 30 photons created in an avalanche. These photons can propagate into nearby pixels and initiate an additional coincident[1] avalanche breakdown. This phenomenon is known as *optical cross-talk*. In many SiPM devices, this effect is suppressed by introducing trenches in between the pixels, which act as an optical barrier. With this technique, optical cross-talk can be significantly reduced down to the level of a few percent.

[1] The propagation time of the photon can be negligible compared to the timescale of the SiPM signal.

4.3.7. After-pulsing

The phenomenon of a delayed secondary avalanche is refered to a as *after-pulsing*. There are two processes currently being considered to give rise to after-pulsing. The first process is related to impurities in the silicon lattice, which can trap free charge carriers [83]. These impurities are most likely related or even identical to those giving rise to the thermally induced dark-rate. The electrons and holes captured in these so-called *trapping centers* are released after a certain time and can trigger a secondary delayed avalanche. In general, there can be different types of trapping centers, e.g. for electrons and holes, with different characteristic trapping times.
The second process is related to the optical photons produced in the avalanche breakdown. If such a photon is absorbed in the silicon bulk, the generated electron/hole can diffuse into the depleted area on a timescale of several nanoseconds, and in this way trigger a delayed Geiger discharge [84]. This process is much faster than the impurity-assisted after-pulsing, which typically occurs on a timescale of several ten to hundred nanoseconds.
Generally, after-pulses trigger the same pixel where the primary avalanche occurred, except for photon-induced after-pulses where the photon is absorbed in the bulk of a neighbouring pixel. Therefore, the effect of after-pulses is suppressed if the pixel recovery time is larger than the characteristic after-pulsing time. This is for example the case for devices with a large quench resistor. However, this also results in a longer dead-time of the sensor.

4.3.8. Temperature Dependence

All SiPM properties discussed above depend on the temperature. Most notably is the temperature dependence of the breakdown voltage, which typically increases by about 25 mV to 50 mV per Kelvin. This can be explained by the increasing energy loss of electrons and holes in the interactions with phonons. In order to assure a stable detector operation, it is hence crucial to correct for temperature variations by adjusting the applied bias voltage. A detailed study of the temperature dependence of the main SiPM parameters can be found in [85].

4.4. Time Resolution

The time resolution of SiPMs is determined by a multitude of effects, which are summarised in the following sections. A detailed discussion of the SiPM timing behaviour can be found in [76].

4.4.1. Leading Edge Discrimination

Besides the intrinsic detector resolution, the timing performance depends on the method which is used to extract the timestamp of the SiPM signal. One of the most common and simple techniques is the *leading edge discrimination*, which is also used in the measurements and simulation studies presented in the following chapters. In this method, the timestamp is generated when the signal crosses a certain fixed threshold, as depicted in Figure 4.9.
A feature of the leading edge discrimination is, that the assigned timestamp depends on the amplitude of a signal. This effect is known as *time-walk*. Depending on the amplitude distribution, the time-walk can significantly degrade the time resolution. However, if the correlation between the signal amplitude and the assigned timestamps is known, this effect can be corrected for.
There are other techniques for extracting the timestamp which in first approximation are not sensitive to the time-walk effect. An example is the *constant fraction* method, where the discrimination threshold is set relative to the signal amplitude. This method is used in measurements presented in section 7.1.

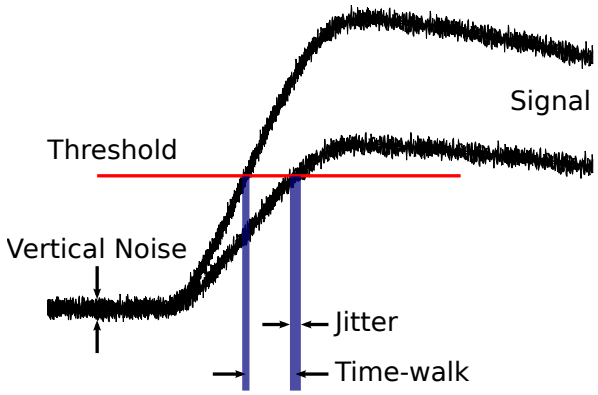

Figure 4.9.: Time-walk and jitter for leading edge timing discrimination.

4.4.2. Vertical Noise

In general, the time jitter of a system is related to the signal rise-time and the total noise on the signal:

$$\sigma_j = \frac{\sigma_{vn}}{S}, \tag{4.12}$$

where σ_{vn} is the vertical noise and S is the slope of the signal at the discrimination time. In many applications, this jitter is one of the dominant factor limiting the time resolution. SiPMs intrinsically exhibit a good time resolution due to the fast signals and the high gain, which result in a steep signal slope. The main contribution to the vertical noise is usually given by the electronic noise σ_{en}. In addition, also SiPM related effects like the dark-rate and fluctuations in the avalanche buildup process contribute to the vertical noise.

4.4.3. Photon Detection Statistics

The time resolution of a photo-sensor is affected by the statistical nature of the photon detection process. Due to the limited PDE, not every photon in a light pulse is detected. The time of the first detected photons can thus fluctuate within the duration of the light pulse. The influence of this effect decreases with larger light intensities and shorter pulse duration. Usually, the contribution to the total time resolution is rather small.

4.4.4. Avalanche Process

The avalanche process is rather complex and underlies statistical fluctuations, which influence the time response behaviour of the SiPM. If a photon is absorpt in the depletion region, the electron (hole) drifts to the n side (p side) with a saturation velocity of about 0.1 µm/ps [86] and initiates an avalanche process when reaching the high field region. The exact starting point of the avalanche can vary, due to the statistical nature of the impact ionisation process. For a typical depletion thickness of a few micrometers the fluctuation in the starting point is in the order of 10 ps and is a negligible contribution to the overall time resolution. However, for photons which are absorpt in a non-depleted region, the electron/hole only reaches the high field region via diffusion, which happens on a timescale of several nanoseconds [86]. Due to the wavelength dependent absorption length, this effect is more pronounced for low energy photons which can penetrate deep into the silicon.
After the initial impact ionisation of the seed charge carrier, the avalanche builds up in longitudinal and transversal direction. This process is depicted in Figure 4.10. The longitudinal

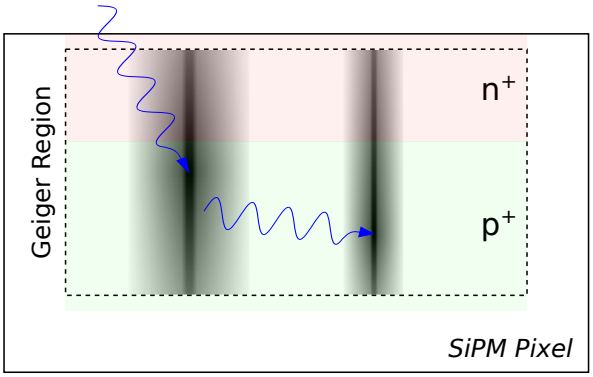

Figure 4.10.: Sketch of the avalanche buildup process. Following the initial impact ionisation, the avalanche quickly extends in longitudinal direction, forming a thin filament, which reaches through the high field region. The slow longitudinal spread of the filament is supported by multiplication assisted diffusion. In addition, photons emitted in the multiplication process can form secondary avalanche filaments.

spread develops exponentially until the avalanche has extended to a thin filament reaching through the high field region. This longitudinal multiplication occurs within a few picoseconds; therefore the associated uncertainty in the time development is negligible [86].
The transversal avalanche spread, occurring on a time scale of a few 100 ps, is much slower than the longitudinal spread. The two main mechanism involved in the transversal avalanche development are photon assisted propagation [87] and multiplication assisted diffusion [88].
The photon assisted propagation has the same origin as optical cross-talk. The photons generated during the avalanche process can be re-absorpt in the pixel and form a secondary avalanche filament. The transversal spread of a filament occurs via diffusion of the charge carriers, which is enhanced in the multiplication process. This is typically the dominant process for the transversal avalanche spread. The diffusion speed is given by $v_d = 2\sqrt{D/\tau_m}$ [88], where D is the diffusion coefficient and $1/\tau_m$ is the multiplication rate. Typical values are in the order of $\mathcal{O}(10\,\mu\text{m/ns})$. Fluctuations in the diffusion speed lead to variations in the rise time of the avalanche current, which can result in a time jitter in the order of 100 ps. This jitter decreases for larger operating voltage, due to the higher multiplication rate.
The diffusion spread also depends on the seed position of the avalanche. It has been shown in [88,89], that the time resolution is significantly degraded for photon absorption at the edges of a pixel compared to photon absorption at the center of a pixel. Furthermore, the time resolution depends on the pixel position relative to the metal contacts of the common anode and cathode, as shown in [89]. Pixels far away of the common metal contacts have a larger serial resistance due to the longer connection path. This results in a reduced avalanche current and rise time, compared to pixels close to the metal contacts. In addition, inhomogeneities in the doping concentration and quench resistance can also lead to pixel-to-pixel variations in the avalanche time response.
In the following, the time resolution associated with the avalanche buildup process is referred to as *avalanche jitter* σ_{av}, which includes all contributions described above. Considering a certain number of detected photons N_{pe}, the time resolution associated with the avalanche jitter is described by Poisson statistics:

$$\sigma_{av}^{tot}(N_{pe}) = \frac{\sigma_{av}}{\sqrt{N_{pe}}}, \tag{4.13}$$

which has been verified in [73,90].

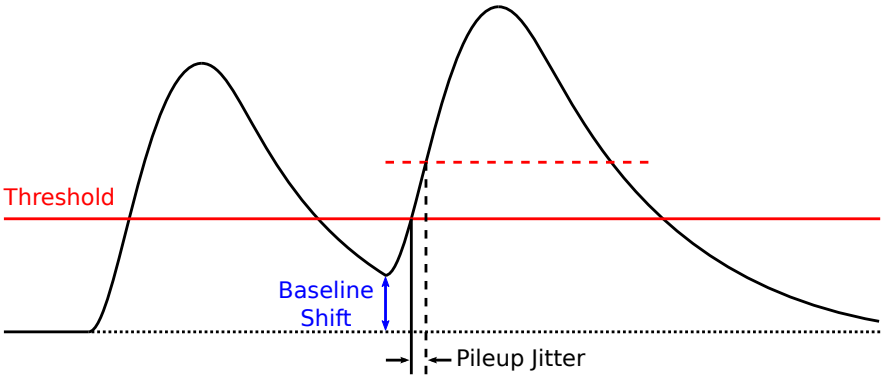

Figure 4.11.: Time jitter introduced by baseline fluctuations due to signal pileup. The red dashed line indicated the threshold corrected for the baseline shift.

4.4.5. Pileup Effects

The pileup of consecutive signals, either from photons or dark-rate, can significantly degrade the time resolution, since the signal overlap changes the baseline of the later signal. This effect is sketched in Figure 4.11. The pileup of dark-rate pulses is often one of the main parameters limiting the single pixel time resolution. For applications with hight light intensities, this is usually negligible. There are several techniques to reduce the influence of pileup, including software correction methods [91] and electronic compensation circuits [92].

5. Silicon Photomultiplier Simulation

The response behaviour of SiPMs is relatively complex compared to other photo-sensors, in particular due to the pixel recovery and correlated noise from cross-talk and after-pulses. For the design and operation of a SiPM-based particle detector, a deep understanding of the SiPM response is crucial. Within the scope of this thesis, the SiPM simulation framework GosSiP[1] has been developed, which provides a detailed model of the SiPM response. This simulation tool provides the basis for the Mu3e Tile detector simulation presented in section 6.3. This chapter presents the GosSiP simulation framework, as well as validation measurements for the SiPM charge and timing response. These studies, excluding the time response validation, have been published in JINST[2] [93].

5.1. The GosSiP Simulation Framework

The GosSiP framework is designed to provide a detailed model of the SiPM response. The simulation is not specifically designed for the Mu3e application, but rather is a universal simulation tool, which can be used for a large variety of applications and essentially allows to model any type of SiPM by specifying the corresponding device parameters. The task of the simulation is to generate the SiPM signal waveform and output charge for a given incident light pulse. The simulation concept is based on Monte Carlo methods, which allows to model all the different noise sources and saturation effects in a native way. Besides the SiPM simulation, the framework includes a simplified simulation of a light source and data acquisition, as well as a graphical user interface (see Figure A.2) for convenient use.
The input for the simulation comprises the information about the incoming light pulse and the basic parameters describing the SiPM properties: PDE $\mathcal{E}_{pde}$, gain G, single pixel amplitude A_{sp}, excess noise σ_G, thermal pulse time constant τ_{tp}, after-pulsing probability $P_{ap_{s,f}}$, after-pulse time constant $\tau_{ap_{s,f}}$, cross-talk probability P_{ct}, pixel recovery time τ_{rec}, avalanche jitter σ_{av}, electronic noise σ_{en}, the single pixel pulse shape, as well as the number of pixels and the detector size. Most of these parameters are related to the avalanche process, which in principle can be modelled using an advanced semiconductor simulation. However, this requires a detailed knowledge about the specific pixel design and doping profile of the SiPM, which is usually not available. Therefore, the SiPM parameters have to be determined in basic characterisation measurements, which are described in section 5.2.1.
The light pulse information enters the SiPM simulation via a *photon list*, which contains information about the wavelength, impact position and time of each photon hitting the sensor surface. This photon list can be generated by a simple toy Monte Carlo simulation of a light source, which is included in the framework. The time distribution of the light pulse can be parameterised by either a flat, gaussian or exponentially decaying profile with a certain pulse duration. For the spatial distribution, a rectangular or elliptic shape with arbitrary dimensions can be specified. The number of photons in the light pulse can either be fixed or randomised according to a Poisson distribution. Alternatively to the integrated light source simulation,

[1] **G**eneric framew**o**rk for the **s**imulation of **Si**licon **P**hotomultipliers
[2] Journal of Instrumentation

a custom photon list can be specified, which allows to interface the framework with external simulation tools, like Geant4 [94].
The photon list is passed to the main SiPM simulation, which models the response of the sensor to the incident light pulse within a certain time period. The basic simulation flow is sketched in Figure 5.1. Each photon can trigger an avalanche with a certain probability, which is determined by the wavelength dependent PDE parameter. The information about the time and the pixel position of each avalanche is stored in an *avalanche list*, which is sorted chronologically with respect to the avalanche time. In addition to the photon induced signals, randomly distributed avalanches are added to the list, in order to account for the primary dark-rate pulses generated by thermal excitation and quantum tunnelling. For the sake of convenience, all primary dark-rate pulses will in the following be referred to as *thermal pulses*, since the thermal excitation is usually the dominant process. The time interval distribution of the thermal pulses is characterised by the thermal pulse rate parameter.
Each avalanche in the list is processed according to the following steps. First of all, the recovery state of the pixel is determined, which is defined by the momentary over-voltage of the pixel (see Equation 4.7):

$$V_{ov}(t) = V_{ov} \cdot R(t), \tag{5.1}$$

where $V_{ov} = V_{ov}(t \to \infty)$ is the nominal over-voltage, $R(t) = 1 - \mathrm{e}^{-\frac{t}{\tau_{rec}}}$, and t denotes the time to the previous avalanche in the pixel. A fully recovered pixel is described by $R = 1$, whereas $R = 0$ corresponds to a completely unrecovered pixel. The pixel recovery state has an effect on the gain, PDE, excess noise, thermal pulse rate, as well as the cross-talk and after-pulse probability, which is related to the over-voltage dependence of these parameters. Since the gain is directly proportional to the over-voltage (see Equation 4.9), the recovery behaviour of the gain is given by:

$$G(t) = G \cdot R(t), \tag{5.2}$$

where $G = G(t \to \infty)$ is the nominal gain value for a fully recovered pixel. In general the other parameters do not exhibit a linear dependence on the over-voltage. However, in the simulation a linear approximation is utilised, which allows to use the relation in Equation 5.2 for all parameters. This significantly simplifies the number of input parameters required for the simulation. As shown in the validation measurements presented in the next section, this simplification yields a good approximation of the SiPM recovery behaviour.
In the next simulation step, the output charge produced in the avalanche process and the associated signal amplitude are determined from the gain $G(t)$. The excess noise is considered by randomising the obtained value according to a Gaussian distribution.
Each avalanche can trigger cross-talk and after-pulse signals with a respective probability of $P_{ct}(t) = P_{ct} \cdot R(t)$ and $P_{ap}(t) = P_{ap} \cdot R(t)$, where P_{ct} and P_{ap} denote the nominal cross-talk and after-pulse probability. The information about the additional secondary avalanches is inserted into the avalanche list. This natively allows for higher-order noise cascades of cross-talk and after-pulse events. A simplified cross-talk model is implemented, which only considers the four direct neighbours of a pixel for cross-talk events. This model yields an accurate description of the cross-talk process, as demonstrated in [95, 96] and the measurements presented below. Avalanches generated by cross-talk are assumed to start at the same time as the original avalanche, whereas after-pulses exhibit a certain delay. The delay is randomised according to the specified after-pulse time constant. A fast and a slow after-pulse component can be specified in order to account for two different kinds of trapping centers.
In the last simulation step, the resulting signal waveform is generated, which is defined here as the voltage signal measured over the external resistance of the readout circuit (see Figure 4.6).

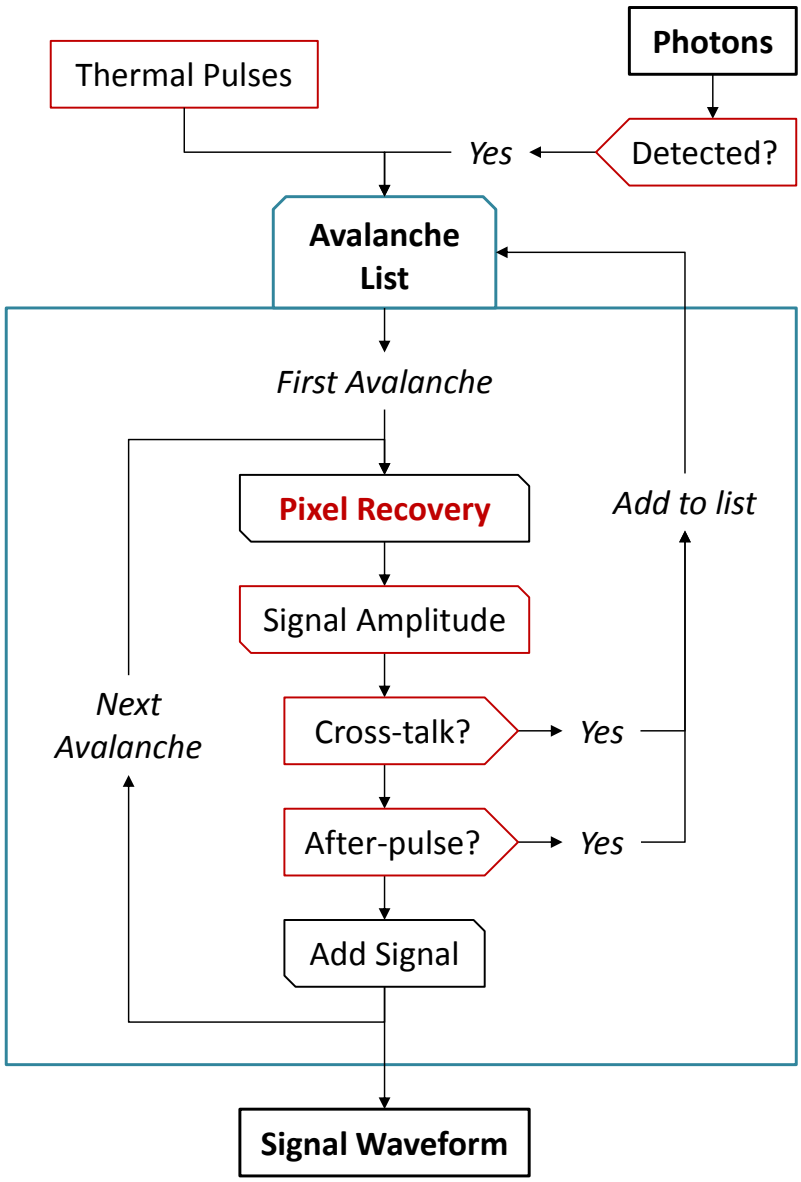

Figure 5.1.: SiPM simulation flow. The steps in the red boxes are influenced by the recovery state of the pixel.

In general, this signal shape depends on many parameters. A detailed modelling of the output waveform would require a full simulation of the SiPM equivalent circuit presented in Figure 4.6, including bandwidth limitations and the electrical properties of the readout electronics. However, this would result in a significant computational effort. Therefore, the simulation relies on a simplified model, where the output pulse is generated by adding up the single pixel signals for all processed avalanches in the list. This approach yields a good approximation of the signal waveform, which is verified in the validation measurements presented in section 5.3. The single pixel pulse shape can be parameterised by an arbitrary function. This function can either be determined from the capacitance and resistance values of the SiPM, as discussed in section 4.3.1 (see Equation 4.2 and Equation 4.6), or the pulse shape can be measured directly with an oscilloscope. By default, the pulse shape is described by a simple double exponential function with the rise time τ_r and decay time τ_d:

$$V(t) = \frac{A_{sp}}{\mathcal{C}} \cdot (\mathrm{e}^{-\frac{t}{\tau_d}} - \mathrm{e}^{-\frac{t}{\tau_r}}), \tag{5.3}$$

where A_{sp} is the single pixel amplitude and $\mathcal{C} = (\frac{\tau_d}{\tau_r})^{-\frac{\tau_r}{\tau_d - \tau_r}} - (\frac{\tau_d}{\tau_r})^{-\frac{\tau_d}{\tau_d - \tau_r}}$. In order to save computation time, each single pixel waveform can be cut off after the signal tail is below a certain adjustable value (typically $\mathcal{O}(0.1\,\%)$). The starting point of each single pixel signal is randomly generated according to a Gaussian distribution, which emulates fluctuations in the avalanche buildup time. It should be noted, that this is a very simplified model of the avalanche timing behaviour and does not reflect the full complexity of the avalanche buildup process described in section 4.4.4.
The generated output waveform can optionally be processed by a simplified simulation model of a data acquisition system used for the most common SiPM characterisation measurements, which are discussed in section 5.2.1.
In the following sections, measurements of the SiPM charge and timing response are presented, which allow to study the accuracy and predictive power of the SiPM simulation. Furthermore, the simulation is used to quantitatively study the impact of different SiPM parameters on the response behaviour.

5.2. Charge Response

One of the primary applications of SiPMs is photon-counting, which is related to the signal charge generated by the SiPM in response to a light pulse. In the Mu3e Tile Detector, the signal charge is primarily required for time-walk correction.
In this section, a measurement of the SiPM charge response to a short light pulse is presented. The charge is measured as a function of the light intensity, up to the saturation level of the SiPM. A SiPM device from Hamamatsu[1], also referred to as MPPC[2], is used for this measurement. The used sensor (MPPC S10362-11-100C) has 100 pixels and an active area of $1 \times 1\,\mathrm{mm}^2$. Two series of measurements are done: one with an over-voltage of $V_{ov} = 0.5\,\mathrm{V}$, corresponding to a low noise level, and one with an over-voltage of $V_{ov} = 1.0\,\mathrm{V}$, corresponding to a high noise level. The measurement data is compared to simulation, which allows the validation of the simulation model for the whole dynamic range.

[1] http://www.hamamatsu.com
[2] Multi Pixel Photon Counter

Table 5.1.: Simulation input parameters determined by the characterisation measurements. The PDE is measured for $\lambda \approx 658\,nm$. The maximum sensitivity of the used sensor is at $\lambda \approx 460\,nm$. The single pixel pulse shape input is given by the measured signal waveform. The parameters A_{sp} and σ_{av} are not required for this measurement. (Published in [97]).

Parameter	$V_{ov} = 0.5\,\mathrm{V}$	$V_{ov} = 1.0\,\mathrm{V}$
$\mathcal{E}_{pde}$ [%]	4.8 ± 0.3	11.6 ± 0.6
$G \cdot 10^6$	0.99 ± 0.03	2.37 ± 0.07
σ_G/G [%]	13.2 ± 0.3	5.8 ± 0.3
σ_{en}/G [%]	6.4 ± 0.3	9.1 ± 0.3
τ_{tp} [ns]	6632 ± 66	2821 ± 28
τ_{ap_s} [ns]	211 ± 26	181 ± 6
τ_{ap_f} [ns]	61 ± 7	61 ± 2
P_{ap_s} [%]	2.3 ± 0.1	13.0 ± 0.6
P_{ap_f} [%]	3.6 ± 0.2	16.3 ± 0.4
$P_{ct}^{n\geq 1}$ [%]	2.4 ± 0.1	14.3 ± 0.6
τ_{rec} [ns]	38.4 ± 1.8	38.4 ± 1.8

5.2.1. Simulation Input

For the simulation input, the following SiPM parameters are required: PDE, gain, excess noise, electronic noise, thermal pulse time constant, cross-talk probability, after-pulse probabilities and time constants, recovery time and the single pixel pulse shape. The SiPM parameters are determined via characterisation measurements, which are summarised in this section. A detailed description of the characterisation procedure is given in [58, 85, 97]. The data acquisition used for the SiPM characterisation, as well as for the measurement of the charge response, is based on modular crate electronics (NIM, CAMAC and VME modules). The SiPM parameter values obtained from the characterisation measurements are summarised in Table 5.1.

Recovery Time

There are several methods to determine the recovery time of a pixel. For this study, a basic method is used, where the recovery time is measured indirectly via the pixel capacitance and quench resistance according to Equation 4.5: $\tau_{rec} \approx C_{pix} \cdot R_q$. The value of the quench resistance is obtained from the $I - V$ curve in forward bias operation, shown in Figure 5.2a. The slope of the curve is defined by the total resistance $R_{tot} = \Delta V/\Delta I$, which is given by N_{pix} quench resistors connected in parallel and the external load resistance R_{bias} (see Figure 4.6a) in the readout circuit:

$$\begin{aligned} R_{tot} &= R_q/N_{pix} + R_{bias} = \Delta V/\Delta I \\ \Rightarrow R_q &= (\Delta V/\Delta I - R_{bias}) \cdot N_{pix}. \end{aligned} \tag{5.4}$$

The internal resistance of the p-n junction can be neglected. A linear fit to the data points above $V = 1\,\mathrm{V}$ yields a quench resistance of $R_q = (96 \pm 3)\,\mathrm{k\Omega}$. The pixel capacitance $C_{pix} = (400 \pm 14)\,\mathrm{fF}$ is determined from the voltage dependence of the gain shown in Figure 5.2b, using Equation 4.9. The gain measurement is discussed in the next paragraph. The resulting value for recovery time is $\tau_{rec} = (38.4 \pm 1.8)\,\mathrm{ns}$.

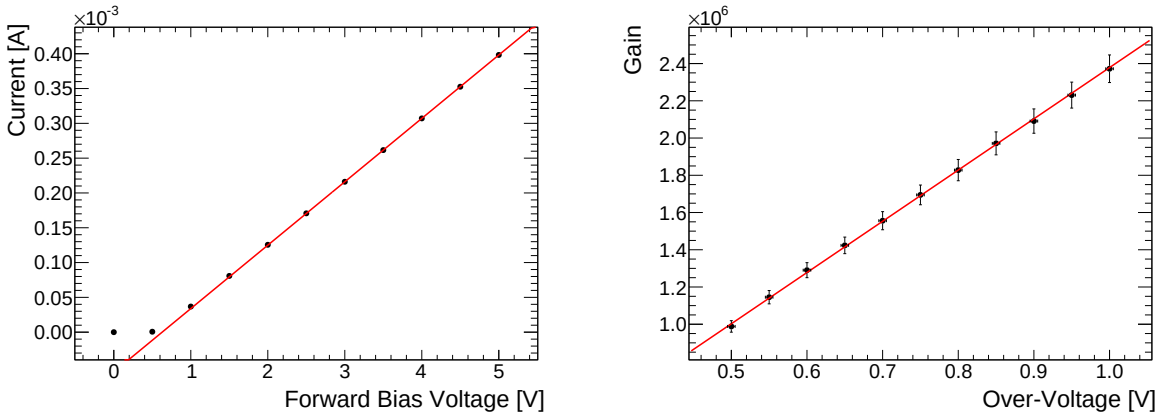

(a) **(b)**

Figure 5.2.: (a) SiPM $I-V$ curve for forward bias operation. The quench resistance is determined from a linear fit to the data above 1 V. (Published in [93].) **(b)** SiPM gain as a function of the over-voltage. The pixel capacity is determined by $C_{pix} \approx \Delta G/\Delta V_{ov} \cdot q_e$. The systematic error of the gain is about 3 %, which arises from the uncertainty in the charge gain of the pre-amplifier.

PDE and Gain

The SiPM charge spectrum for low light levels, also referred to as *single photon spectrum* (SPS), contains information about various SiPM parameters, making it an important tool for the SiPM characterisation. It is obtained by illuminating the sensor with a short $\mathcal{O}(1\,\text{ns})$ light pulse and measuring the integrated signal charge. Figure 5.3 shows a typical single photon spectrum, which is acquired using a Charge-to-Digital Converter[1] (QDC) and a pre-amplifier[2] with a nominal voltage gain of 50. The spectrum shows several well separated peaks, which correspond to a certain number of avalanche breakdowns, also referred to as photoelectron equivalents (pe). The first peak corresponds to the pedestal value, where no pixel has fired (0 pe). The second peak corresponds to a single pixel signal (1 pe), the third peak corresponds to two pixel signals (2 pe), and so on. The difference between two adjacent peaks therefore is associated with the charge produced in an avalanche, in the following referred to as *single pixel charge* Q_{pix}. It should be noted, that this definition includes the charge amplification by the pre-amplifier. The single pixel charge is directly proportional to the SiPM gain: $G = Q_{pix}/(q_e \cdot \mathcal{A})$, where $\mathcal{A}$ is the charge gain of the pre-amplifier. The voltage dependence of the gain, shown in Figure 5.2b, allows to determine the pixel capacitance and break-down voltage, according to Equation 4.9. The width of the peaks in the SPS is related to the gain fluctuations, according to Equation 4.10:

$$\sigma_G = \sqrt{\sigma_{1pe}^2 - \sigma_{en}^2}, \tag{5.5}$$

where σ_{1pe} is the width of the first photoelectron peak and σ_{en} is the width of the pedestal peak. The mean value of the spectrum Q is proportional to the average number avalanche breakdowns:

$$N_{av} = (Q - Q_{ped})/Q_{pix}, \tag{5.6}$$

where Q_{ped} is the pedestal value. The value N_{av} quantifies the total number of fired pixels, including signals from dark-rate, cross-talk and after-pulses. The number of detected photons,

[1] LeCroy Model 2249A, 12-Channel Charge Integrating ADC, 50 Ω input impedance
[2] Phillips Scientific Model 774, Voltage gain: 50, Bandwidth: (100-1500) kHz (3dB)

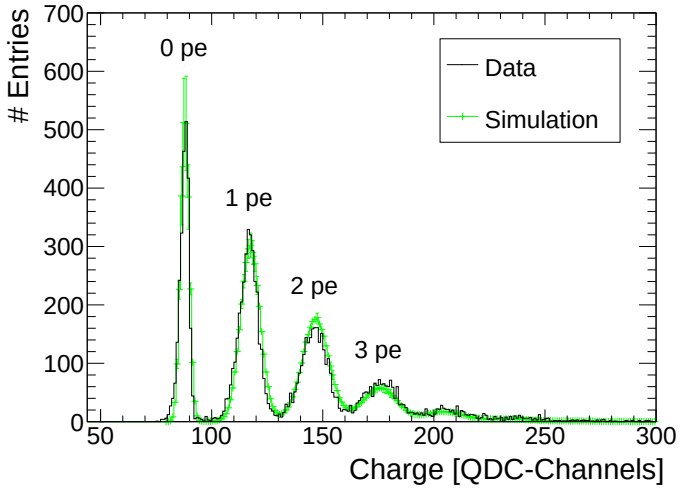

Figure 5.3.: Single photon spectrum for $V_{ov} = 0.5\,\mathrm{V}$ over-voltage. Each peak corresponds to a certain number of fired pixels (pe). The well separated peaks demonstrate the excellent single photon resolution of SiPMs. The spectrum holds information about a multitude of SiPM parameters, e.g. the gain, which is determined by the charge difference of neighbouring peaks. (Published in [93].)

without these noise contributions, can be determined exploiting the statistical nature of the photo-detection process. The number of detected photons n follows a Poisson distribution[1] $\mathcal{P}(n, N_{pe})$. The average number of detected photons N_{pe} can be inferred from the probability to detect no photons:

$$\begin{aligned} \mathcal{P}(0, N_{pe}) &= \mathrm{e}^{-N_{pe}} \\ \Rightarrow N_{pe} &= -ln(\mathcal{P}(0, N_{pe})) = -ln(\frac{c_{dr} \cdot N_{ped}}{N_{tot}}). \end{aligned} \tag{5.7}$$

The probability $\mathcal{P}(0, N_{pe})$ is given by the number of events in the pedestal peak N_{ped} over the total number of events N_{tot} in the charge spectrum. It should be noted, that $\mathcal{P}(0, N_{pe})$ is not sensitive to cross-talk and after-pulse effects. Therefore N_{pe} yields the number of detected photons without contamination from cross-talk and after-pulse signals. The correction factor c_{dr} accounts for dark-rate events, which result in a signal above the pedestal value, although no photon is detected. This correction factor can be determined from a dark-rate charge spectrum, where the sensor is not illuminated:

$$c_{dr} = N^{dr}_{tot}/N^{dr}_{ped}, \tag{5.8}$$

where N^{dr}_{tot} is the total number of events and N^{dr}_{ped} is the number of events in the pedestal peak of the dark-rate spectrum.
The PDE can be determined from a SPS measured with a referenced light intensity, i.e. the average number of incident photons N_{phot} is known. The statistical analysis of the spectrum described by Equation 5.7 allows to determine the PDE without contributions from cross-talk, after-pulse and dark-rate:

$$\mathcal{E}_{pde} = N_{pe}/N_{phot}. \tag{5.9}$$

A detailed description of the PDE measurement has been published in [58, 85, 97].

[1] Although the photon detection itself follows a Binomial distribution, its convolution with the Poisson distributed number of photons results again in a Poisson distribution.

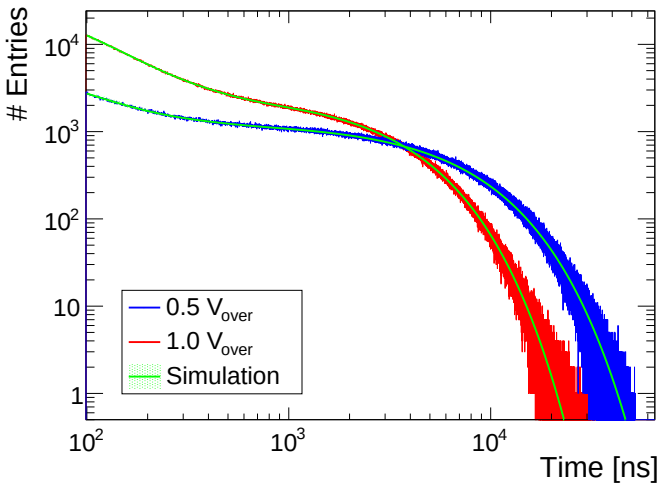

Figure 5.4.: Spectrum of the time intervals between two consecutive dark-rate pulses. The spectrum is used to extract the thermal pulse and after-pulse parameters. (Published in [93].)

Dark-rate and After-pulsing

The dark-rate and after-pulse parameters can be determined from a statistical analysis of the time interval t between consecutive dark-rate pulses. The spectrum of the time intervals measured for the two over-voltages under study is shown in Figure 5.4.
The spectrum is recorded using a discriminator[1] with a 0.5 pe threshold, and a Time-to-Digital Converter[2] (TDC), which measures the timestamps of the discriminator output signals. The minimum time interval which can be measured with this setup is limited to roughly $t = 100\,\text{ns}$. This limit is related to the time-over-threshold of the SiPM signal and the dead-time of the discriminator.
The time spectrum contains primary dark-rate events and a contribution from after-pulses. The shape of the spectrum is related to the probability density for a dark-rate pulse to occur at a time t with respect to the previous pulse. The probability density for thermal pulses is given by:

$$p_{tp}(t) = \frac{1}{\tau_{tp}} \cdot \mathrm{e}^{-\frac{t}{\tau_{tp}}}, \tag{5.10}$$

with the characteristic thermal pulse time constant τ_{tp}.
For the after-pulse component, this probability density is multiplied with the after-pulse probability P_{ap}:

$$p_{ap}(t) = \frac{P_{ap}}{\tau_{ap}} \cdot \mathrm{e}^{-\frac{t}{\tau_{ap}}}. \tag{5.11}$$

In general, there can be several after-pulse components with different time constants, as discussed in section 4.3.7. Assuming a slow and a fast after-pulse component, the dark-rate time spectrum

[1] LeCroy Model 4416
[2] CAEN C 1290A

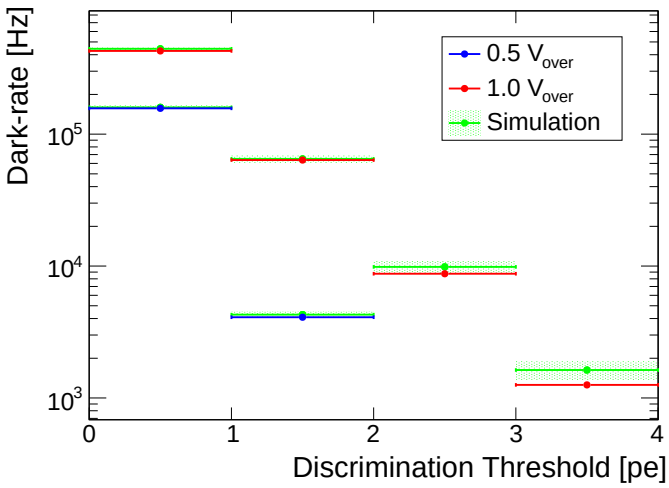

Figure 5.5.: Dark-rate measured at different discrimination thresholds. The rate for a threshold of larger than 1.5 pe is associated with optical cross-talk. (Published in [93].)

is approximated by the following equation:

$$
\begin{aligned}
N(t) = N \cdot \Bigg(& p_{tp}(t) \cdot \left[1 - \int_0^t p_{ap_s}(t')\,\mathrm{dt}'\right] \cdot \left[1 - \int_0^t p_{ap_f}(t')\,\mathrm{dt}'\right] \\
& + p_{ap_s}(t) \cdot \left[1 - \int_0^t p_{tp}(t')\,\mathrm{dt}'\right] \cdot \left[1 - \int_0^t p_{ap_f}(t')\,\mathrm{dt}'\right] \\
& + p_{ap_f}(t) \cdot \left[1 - \int_0^t p_{tp}(t')\,\mathrm{dt}'\right] \cdot \left[1 - \int_0^t p_{ap_s}(t')\,\mathrm{dt}'\right] \Bigg),
\end{aligned}
\tag{5.12}
$$

where $p_{ap_{s/f}}$ denotes the probability density of the slow and fast after-pulse component and N is the total number of entries in the spectrum. The simulation parameters τ_{tp}, $\tau_{ap_{s/f}}$ and $P_{ap_{s/f}}$ can be extracted from the time spectrum by fitting the data with Equation 5.12. However, this approach only yields approximate values of the input parameters, since Equation 5.12 does not take into account cross-talk and pixel recovery effects, which influence the number of after-pulse events. Furthermore, Equation 5.12 does not consider after-pulses which do not originate from the preceeding pulse, but come from avalanches prior to this. These effects result in a systematic error in the parameters obtained from the fit. In addition, the minimum time interval of $t = 100\,\mathrm{ns}$ which can be achieved with this setup reduces the sensitivity to fast after-pulses, which may also lead to a systematic error in the fit result. In order to improve the accuracy of the input parameter determination, the simulated time spectrum is fitted to the data. This is done by iterative variation of the simulation input parameters τ_{tp}, $\tau_{ap_{s/f}}$ and $P_{ap_{s/f}}$. The resulting values are listed in Table 5.1 and show a deviation of up to 20 % compared to the values obtained from the analytical fit.

Cross-talk

The cross-talk probability can be measured via the amplitude distribution of dark-rate pulses. Signals with an amplitude corresponding to two or more firing pixels can be attributed to cross-talk. The probability of two dark-rate pulses to occur simultaneously[1] is usually negligible.

[1] i.e. within a short time interval $\mathcal{O}(1\,\mathrm{ns})$, such that the total amplitude is equivalent to a 2 pe signal.

The dark-rate amplitude spectrum is measured using a discriminator[1] with a tunable discrimination threshold. The output signals of the discriminator are counted using a scaler module[2]. Figure 5.5 shows the measured dark-rate as a function of the discrimination threshold for $V_{ov} = 0.5\,\mathrm{V}$ and $V_{ov} = 1.0\,\mathrm{V}$. The probability for a dark-rate pulse to trigger at least one cross-talk signal is given by the ratio of the rate at 1.5 pe and 0.5 pe threshold:

$$P_{ct}^{n\geq 1} = \frac{DR_{1.5pe}}{DR_{0.5pe}}. \tag{5.13}$$

The optical cross-talk model in the simulation is parameterised by the cross-talk value P_{ct}, which describes the probability for an avalanche to trigger one specific neighbouring pixel via cross-talk. Since in the simulation only the four direct neighbours are considered, the measured cross-talk probability $P_{ct}^{n\geq 1}$ is related to the simulation parameter P_{ct} via the following approximation:

$$(1 - P_{ct})^4 \approx 1 - P_{ct}^{n\geq 1}. \tag{5.14}$$

Single Pixel Pulse Shape

The pulse shape of a single pixel signal is measured using an oscilloscope. Several waveforms are acquired and averaged, in order to eliminate the electronic noise on the signal. This averaged waveform is used as the simulation input for the single pixel pulse shape.

5.2.2. Validation of the Simulation for Low Light Levels

The characterisation measurements presented above have been reproduced with the simulation, in order to validate the physics models used to describe the different SiPM properties (i.e. the photon detection, excess noise, dark-rate, cross-talk and after-pulsing process). The simulated dark-rate time spectrum shown in Figure 5.4 is in good agreement with the data, which validates the implemented model for after-pulsing and thermal pulses. The total dark-rate at a threshold of 0.5 pe, shown in Figure 5.5, is also well described by the simulation. Since the total dark-rate is mainly determined by thermal pulses and after-pulses, this independently demonstrates the accuracy of the thermal pulse and after-pulse simulation model. The dark-rate for a threshold of 2.5 pe and 3.5 pe is slightly overestimated by the simulation. This can most likely be attributed to the simplified cross-talk model used in the simulation. The probability for an avalanche to trigger two ore more cross-talk signals, corresponding to a threshold of 2.5 pe and higher, is typically in the order of $\mathcal{O}(1\,\%)$. Therefore, this effect can safely be neglected for most practical purposes.
The single photon spectrum shown in Figure 5.3 is also well modelled by the simulations. Since the shape of the spectrum is sensitive to cross-talk, after-pulses and dark-rate, this reassures the validity of the simulation model of these noise sources.
The above results show, that the simulation accurately describes the SiPM dark-rate and response to low light levels. At higher light intensities, the pixel recovery effects and the increasing occupancy have a significant impact on the SiPM response. Therefore, the validation of the simulation has been extended by measuring the SiPM charge response as a function of the light intensity, covering the whole dynamic range of the sensor. This allows to study the accuracy and predictive power of the SiPM simulation. In the following, the measurement and simulation results are presented.

[1] LeCroy 4416
[2] LeCroy Model 2250B

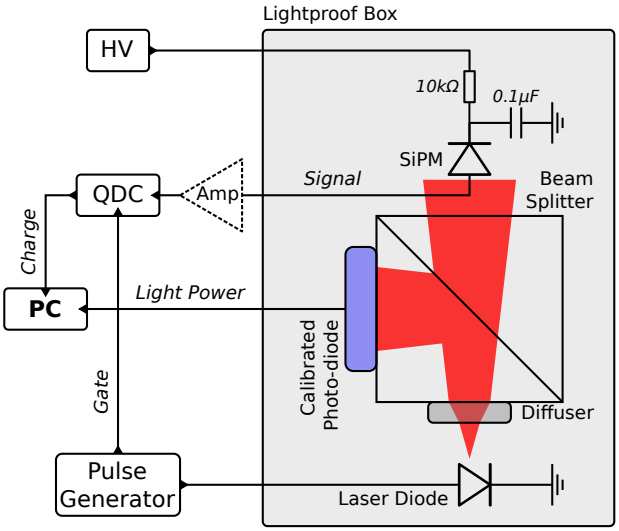

Figure 5.6.: Schematic view of the setup for the SiPM response curve measurement. (Published in [93].)

5.2.3. Measurement Setup

A schematic view of the setup for the SiPM charge response measurement is shown in Figure 5.6. The SiPM is illuminated using a laser diode emitting light with a wavelength of $\lambda \approx 658\,\text{nm}$. The laser diode is driven by a pulse generator, which generates voltage pulses with a width of 4 ns. A beam splitter in the optical path of the light pulse equally distributes the light to the SiPM and a calibrated PIN photo-diode, which is used as a reference sensor with nearly ideal linear response. The charge produced by the SiPM in response to the light pulse is measured with a QDC. Within the used integration time of 300 ns, practically 100 % of the SiPM signal charge is collected.
The SiPM response and saturation behaviour strongly depend on the time and spatial distribution of the light pulse. In order to uniformly illuminate the SiPM, a diffuser is installed in front of the beam splitter, which produces a well defined homogeneous light spot. The influence of the time structure of the light pulse is minimised by the long recovery time of the SiPM of $\tau_{rec} \approx 38\,\text{ns}$, which is much longer than the pulse duration set at the pulse generator. However, it has been observed that the SiPM response at high light levels still exhibits a small dependence on the duration of the voltage pulse driving the laser diode. Therefore, the actual time structure of the light pulse is estimated from the shape of the rising edge of the SiPM signal. Figure 5.7 shows the SiPM signal recorded with an oscilloscope for a light intensity corresponding to about 20 firing pixels. The rising edge of the measured signal is compared to simulated signal waveforms with different light pulse distributions. The best agreement between data and simulation is achieved for a flat time distribution of the photons with a pulse duration of about $(1.0 \pm 0.5)\,\text{ns}$. The discrepancy between this estimated light pulse duration and the 4 ns voltage pulse duration is assumed to originate from the time response characteristics of the laser diode.
The SiPM response, i.e. the number of fired pixels N_{av}, is measured as a function of the number of incident photons N_{phot}. The number of fired pixels is obtained from the average signal charge according to Equation 5.6. Due to the limited dynamic range of the QDC, the response curve is measured without a pre-amplifier. As a consequence, the value for the single pixel charge Q_{pix} required in Equation 5.6 cannot be measured directly, since the individual peaks in the charge spectrum cannot be resolved without amplification of the signal. Therefore, Q_{pix} is determined indirectly from charge spectra recorded with a pre-amplifier. The value Q^A_{pix} obtained with

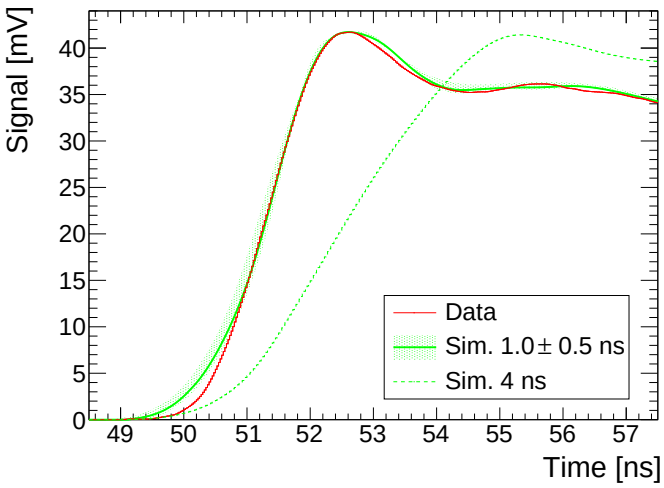

Figure 5.7.: Rising edge of the signal (about 20 firing pixels). The measured waveform is shown in red, the simulated waveform assuming a flat 1.0 ± 0.5 ns light pulse is shown in green. The simulated waveform assuming a flat 4.0 ns light pulse is shown by the dashed green line. (Published in [93].)

amplification is related to the non-amplified value Q_{pix} via the following equation:

$$Q_{pix} = \mathcal{A} \cdot Q^A_{pix} = \frac{Q - Q_{ped}}{Q^A - Q^A_{ped}} \cdot Q^A_{pix}, \tag{5.15}$$

where $\mathcal{A}$ is the charge amplification factor, which is determined by the ratio of the signal charge measured with and without the amplifier. The obtained value for the charge amplification factor is $\mathcal{A} = 48.0 \pm 1.5$. The deviation from the nominal voltage gain can be explained by a small undershoot in the tail of the amplified signals.
The number of photons N_{phot} hitting the active area of the SiPM is measured using the calibrated PIN diode. The ratio between N_{phot} and the light power measured at the PIN diode is calibrated at low light intensities, where the individual peaks in the SiPM charge spectrum are well separated. In order to be able to resolve the individual peaks in the spectrum, the pre-amplifier is used for this calibration measurement. For the obtained spectra, the number of detected photons N_{pe} can be derived from to the statistical analysis described in Equation 5.7, and therefore the number of incident photons can be directly determined by:

$$N_{phot} = N_{pe}/\mathcal{E}_{pde}. \tag{5.16}$$

This allows to relate the light power measured at the calibrated PIN diode to the number of photons hitting the active area of the sensor. The uncertainty in this calibration leads to a systematic error in N_{phot} of about 5 %.

5.2.4. Results

Figure 5.8 and Figure 5.9 show the measured and simulated number of fired pixels N_{av} as a function of the number of incident photons N_{phot} for $V_{ov} = 0.5$ V and $V_{ov} = 1.0$ V, respectively. For the lower over-voltage of $V_{ov} = 0.5$ V the noise contributions are rather small and the saturation behaviour is predominantly determined by the PDE. The response curve is fitted using a slight modification of Equation 4.8:

$$N_{av}(N_{phot}) = N_{max} \cdot (1 - \mathrm{e}^{-\frac{\mathcal{E} \cdot N_{phot}}{N_{max}}}) + N_{dr}, \tag{5.17}$$

where $\mathcal{E}$ denotes the effective efficiency, which is given by the mean number of avalanches triggered by an incoming photon, including the PDE, cross-talk and after-pulse probability, and N_{dr} is the mean number of dark-rate events occurring within the charge integration window. The maximum saturated signal N_{max} corresponds to approximately 104 pixel signals. This saturation level is given by the total number of pixels $N_{pix} = 100$ plus a contribution from after-pulses and cross-talk, which causes an excess of 4 % over the ideal limit.
For the measurement at $V_{ov} = 1.0\,\mathrm{V}$, the fit function has to be modified, in order to account for the large contribution from correlated noise. The measured response curve is well described by a phenomenological model, which is parameterised by [98]:

$$N_{av}(N_{phot}) = N_{max} \cdot (1 - \mathrm{e}^{-\frac{\mathcal{E} \cdot N_{phot}}{N_{max}}}) / (1 - \mathcal{E}_{cn} \cdot \mathrm{e}^{-\frac{\mathcal{E} \cdot N_{phot}}{N_{max}}}) + N_{dr}, \tag{5.18}$$

where $\mathcal{E}_{cn}$ describes the contribution from cross-talk and after-pulses. These noise contributions lead to an increase of the saturation signal of approximately 20 %, compared to the ideal value of 100 pe.
The response curve for both operation voltages is well described by the simulation, considering the uncertainties of a few percent. The error band of the simulated data is determined by the uncertainties in the input parameters. The simulation allows to directly extract the contribution from the different noise sources to the overall charge response. The dominant contributions are shown in the lower part of the figures; effects which contribute less than 1 % are not shown. The after-pulse contribution to the signal is practically constant over the hole dynamic range, since the time scale for the after-pulse is much longer than the pixel recovery time. The prompt contribution from cross-talk decreases with higher light intensities, due to the increasing occupancy. For large signal amplitudes close to the saturation level, the contribution from primary cross-talk events approaches zero. However, cross-talk originating from after-pulse events still significantly contributes to the SiPM response, even in the saturation region. As a consequence, the overall cross-talk contribution shown in Figure 5.8 and Figure 5.9 only slightly decreases for higher light intensities.
Figure 5.10 and Figure 5.11 show the signal resolution, which is defined by the RMS of the signal charge $\sigma_{N_{av}} = Q_{RMS}/Q_{pix}$. The measured resolution is also well described by the simulation in the whole measurement range. The different noise contributions, which are obtained from the simulation, strongly depend on the incident photon flux. For low light intensities, the noise contributions are rather small. Consequently, the PDE is the limiting factor for the resolution. For high light intensities, cross-talk and after-pulses significantly contribute to the signal resolution, in particular for an operation voltage of $V_{ov} = 1.0\,\mathrm{V}$.
Figure 5.12 and Figure 5.13 show the relative photon-counting resolution, which is derived from the inverted response curve $N_{phot}(N_{av})$ and the resolution $\sigma_{N_{av}}$:

$$\frac{\sigma_{N_{phot}}}{N_{phot}} = \frac{\frac{\partial N_{phot}}{\partial N_{av}} \cdot \sigma_{N_{av}}}{N_{phot}}. \tag{5.19}$$

In the linear response range where the signal saturation can be neglected, the photon-counting resolution can be parameterised by the following equation:

$$\frac{\sigma_{N_{phot}}}{N_{phot}} = \frac{\alpha}{N_{phot}} \oplus \frac{\beta}{\sqrt{N_{phot}}}. \tag{5.20}$$

The first term describes the contribution from the dark-rate and the second term (stochastic term) describes the fluctuations in the number of detected photons related to the PDE, as well

as contributions from cross-talk and after-pulses. This ideal behaviour is shown by the dashed line in Figure 5.12 and Figure 5.13, where Equation 5.19 is fitted to the data points at low intensity corresponding to a response below 20 pixels. For high light intensities, this assumption breaks down, as the signal saturation significantly contributes to the photon-counting resolution. The best resolution of roughly $\sigma_{N_{phot}}/N_{phot} = 20\,\%$ is achieved for about 70 to 80 fired pixels for both over-voltages, corresponding to about 2500 photon for $V_{ov} = 0.5\,\mathrm{V}$ and 1000 photons for $V_{ov} = 1.0\,\mathrm{V}$. The simulation shows, that in a for low light intensities, the noise contributions from dark-rate, cross-talk and after-pulses are rather small. Thus, the limiting factor is the PDE. However, for signals in the saturation region, cross-talk and after-pulses significantly contribute to the resolution.
The results presented in this section show that the simulation accurately models the SiPM charge response and saturation behaviour. The noise contributions from dark-rate, cross-talk, after-pulsing are relatively large for the studied MPPC, which is related to the large pixel size. It is thus expected, that the SiPM simulation also accurately describes the charge response and saturation behaviour for other sensors, which usually exhibit lower noise rates.

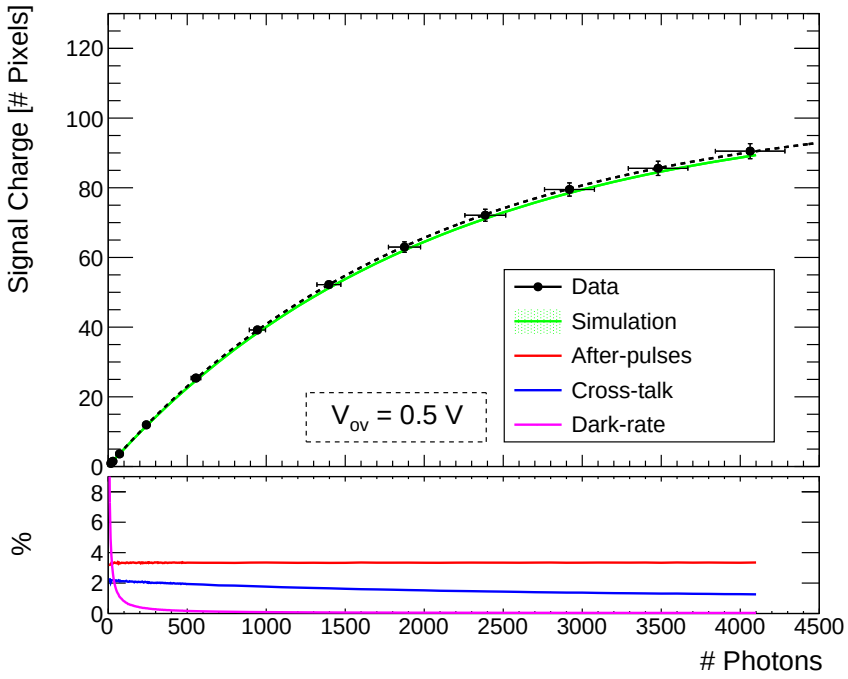

Figure 5.8.: *(Top)* SiPM response for low noise operation ($V_{ov} = 0.5\,\mathrm{V}$). *(Bottom)* Contribution from different noise sources. (Published in [93].)

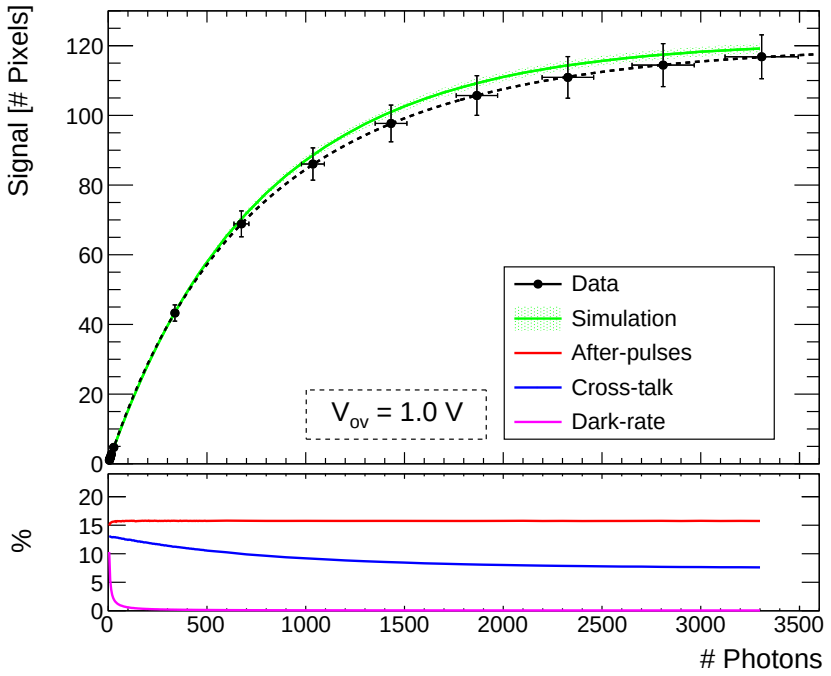

Figure 5.9.: *(Top)* SiPM response for high noise operation ($V_{ov} = 1.0\,\mathrm{V}$). *(Bottom)* Contribution from different noise sources. (Published in [93].)

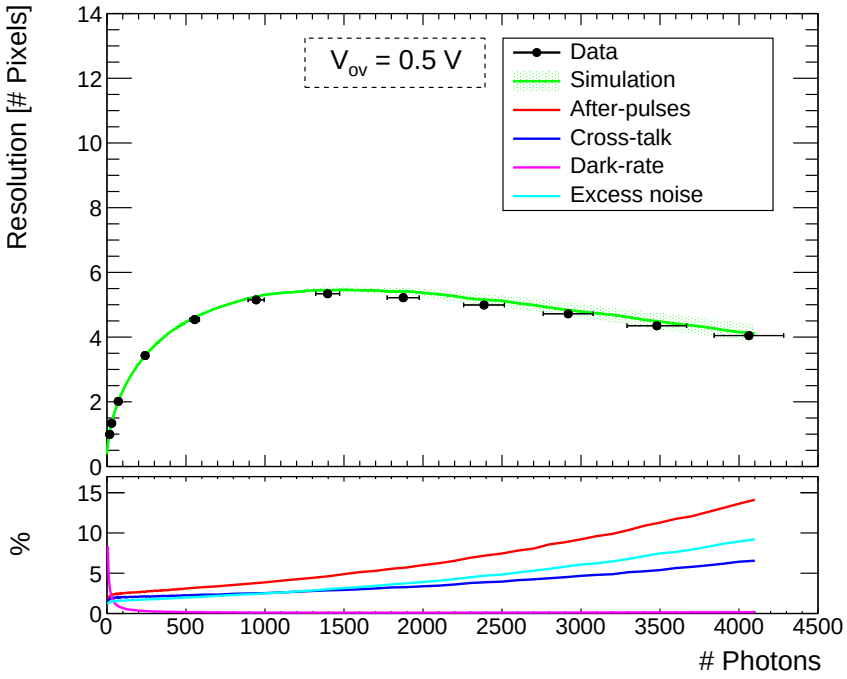

Figure 5.10.: *(Top)* Resolution of the signal for low noise operation ($V_{ov} = 0.5\,\mathrm{V}$). *(Bottom)* Contribution from different noise sources. (Published in [93].)

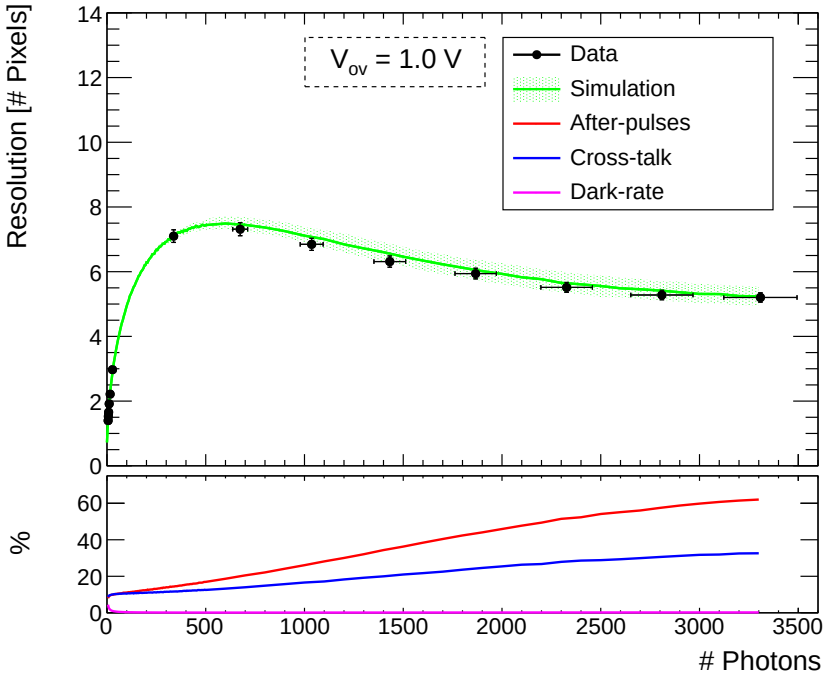

Figure 5.11.: *(Top)* Resolution of the signal for high noise operation ($V_{ov} = 1.0\,\mathrm{V}$). *(Bottom)* Contribution from different noise sources. (Published in [93].)

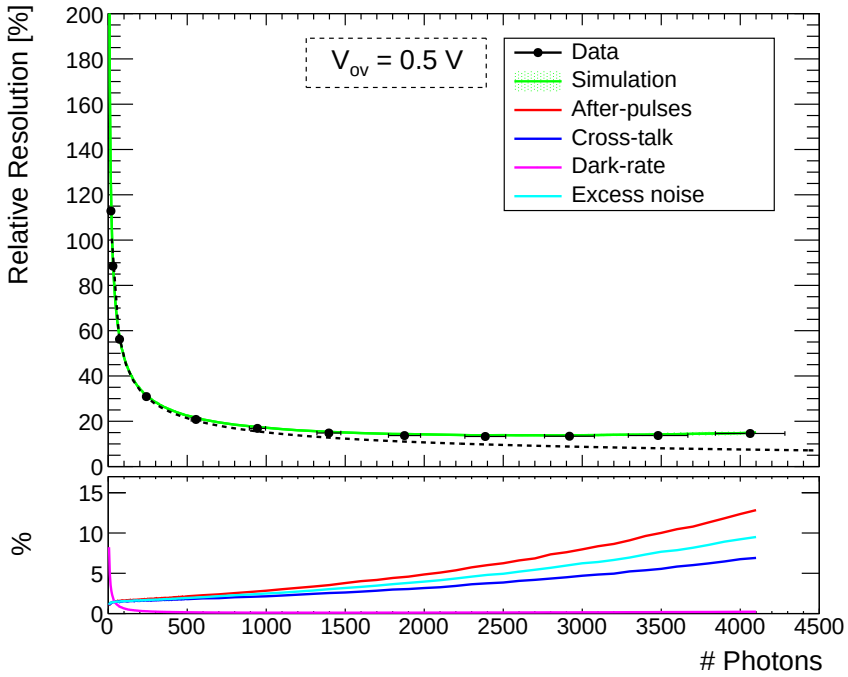

Figure 5.12.: *(Top)* Photon-counting resolution for low noise operation ($V_{ov} = 0.5\,\mathrm{V}$). The dotted line shows the resolution assuming no saturation effects. *(Bottom)* Contribution from different noise sources. (Published in [93].)

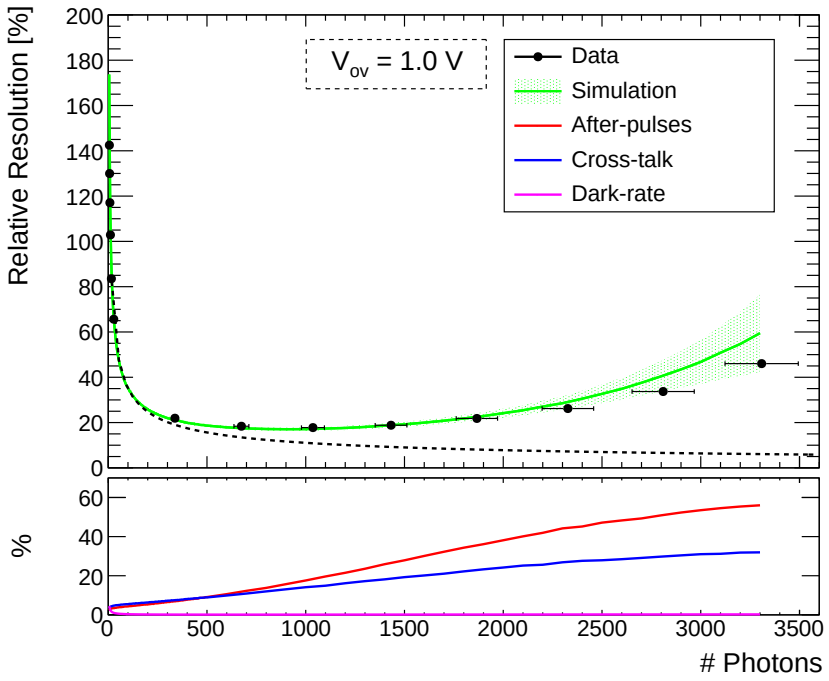

Figure 5.13.: *(Top)* Photon-counting resolution for high noise operation ($V_{ov} = 1.0\,\mathrm{V}$). The dotted line shows the resolution assuming no saturation effects. *(Bottom)* Contribution from different noise sources. (Published in [93].)

Table 5.2.: Simulation input parameters determined by the characterisation measurements. The PDE is measured at $\lambda \approx 408\,nm$. The single pixel pulse shape is given by a double exponential function with the parameters τ_r and τ_d. The gain parameter G is not required for this measurement. The excess noise parameter $\sigma_{A_{sp}}/A_{sp}$ is equivalent to σ_G/G.

Parameter	$V_{ov} = 1.0\,\mathrm{V}$	$V_{ov} = 1.5\,\mathrm{V}$	$V_{ov} = 2.0\,\mathrm{V}$
$\mathcal{E}_{pde}$ [%]	25.7 ± 2.6	34.6 ± 3.5	41.2 ± 4.1
A_{sp} [mV]	0.19 ± 0.03	0.29 ± 0.03	0.38 ± 0.03
$\sigma_{A_{sp}}/A_{sp}$ [%]	12.6 ± 0.4	8.5 ± 0.2	6.4 ± 0.1
σ_{en} [mV]	0.45 ± 0.1	0.45 ± 0.1	0.45 ± 0.1
τ_{tp} [ns]	1295 ± 65	511 ± 26	353 ± 18
τ_{ap} [ns]	41 ± 2	41 ± 2	41 ± 2
P_{ap} [%]	8 ± 2	18 ± 2	33 ± 2
$P_{ct}^{n\geq 1}$ [%]	10 ± 2	12 ± 2	16 ± 2
τ_{rec} [ns]	13.5 ± 1.0	13.5 ± 1.0	13.5 ± 1.0
τ_r [ps]	100 ± 20	100 ± 20	100 ± 20
τ_d [ns]	25 ± 1	25 ± 1	25 ± 1
σ_{av} [ps]	100 ± 50	100 ± 50	100 ± 50

5.3. Timing Response

In many application, like the Mu3e experiment, the timing response of SiPMs is a critical parameter. This section presents a measurement of the SiPM time resolution in response to a fast light pulse. The measurement is carried out with a $3 \times 3\,\mathrm{mm}^2$ MPPC[1] with a pixel size of 50 µm, operated at over-voltages of $V_{ov} = 1.0\,\mathrm{V}$, $V_{ov} = 1.5\,\mathrm{V}$ and $V_{ov} = 2.0\,\mathrm{V}$. This MPPC type is proposed for the Tile Detector and was used in a detector prototype, which is presented in chapter 7. The results of the time resolution measurement are compared to simulation, in order to validate the SiPM simulation model with respect to the timing behaviour. This lays the foundation for the simulation of the time resolution of a combined scintillator-SiPM system, presented in chapter 6. Furthermore, the simulation is used to determine the parameters which limit the SiPM time resolution.

5.3.1. Simulation Input

The SiPM input parameters for the simulation are determined in a similar way as described in section 5.2.1. The obtained parameter values which are relevant for this measurement are summarised in Table 5.2. The data acquisition used for the SiPM characterisation, as well as for time resolution measurement, is based on a digital storage oscilloscope[2] (DSO), which records the waveforms of the SiPM signals. The waveforms are analysed using a custom peak finding algorithm, which identifies individual signals and extracts their amplitude and timestamp. For pileup signals, like fast after-pulses, the amplitude relative to the local baseline is determined. An example of an analysed dark-rate waveform is shown in Figure 5.14a.
The waveform analysis generally allows for a more precise determination of the SiPM parameters, compared to the data acquisition used in section 5.2.1. This is essential for the used $3 \times 3\,\mathrm{mm}^2$ device, since the larger dark-rate of this sensor significantly degrades the precision of SiPM characterisation.

[1] S10362-33-050C
[2] LeCroy Waverunner 610Zi

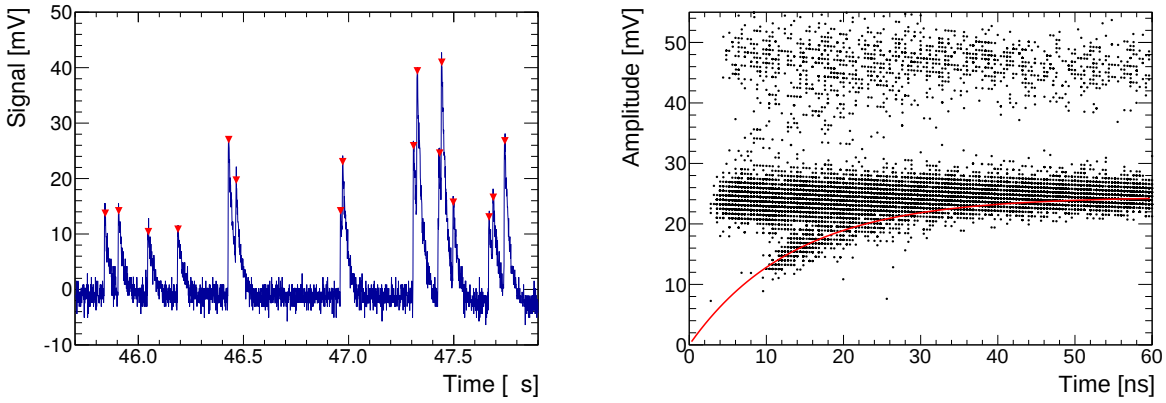

(a) **(b)**

Figure 5.14.: **(a)** Analysed waveform of dark-rate signals. The red triangles mark the time and amplitude of the signals identified by the peak finding algorithm. **(b)** Amplitude of dark-rate pulses as a function of the time interval to the previous pulse. The amplitude of fast after-pulses is reduced due to pixel recovery. The red curve shows a fit of Equation 5.21 to the data points associated with after-pulses.

Recovery Time

The waveform analysis of dark-rate pulses allows to directly measure the recovery time via the amplitude of fast after-pulses. The principle of this method is described in [99, 100]. Since after-pulse events occur in the same pixel as the primary signal, the amplitude of fast after-pulses is reduced due to the pixel recovery:

$$A_{ap}(t) = A_{ap} \cdot R(t), \tag{5.21}$$

where t is the time between the primary signal and the after-pulse. Figure 5.14b shows an exemplary measurement of the amplitude A of dark-rate pulses as a function of t. The data points in the band around $A = 24\,\mathrm{mV}$ correspond to dark-rate signals of fully recovered pixels. The signals with an amplitude of about $A = 48\,\mathrm{mV}$ originate from optical cross-talk. For small time intervals $t \lesssim 20\,\mathrm{ns}$, the after-pules can clearly be distinguished from thermal pulses by the reduced signal amplitude. The recovery time is determined by fitting these events with Equation 5.21, as indicated by the red curve, yielding a value of $\tau_{rec} = (13.5 \pm 1.0)\,\mathrm{ns}$. This is consistent with values obtained via the indirect measurement described in section 5.2.1 [101]. The algorithm used to identify after-pulses limits the minimum time interval to about $t = 10\,\mathrm{ns}$.

PDE and Single Pixel Amplitude

In contrast to the charge measurement presented in section 5.2, the SiPM timing resolution is directly sensitive to the pulse shape and amplitude of the single pixel signal. Therefore, in this simulation the single pixel amplitude A_{sp} is used rather than the gain parameter G, in order to quantify the signal size. It should be noted that A_{sp} and G are directly related and, for a given signal shape, hold the same information.
The amplitude of a single pixel signal A_{sp} is determined from the amplitude spectrum at low light levels, analogous to the determination of the single pixel charge Q_{pix} from the charge spectrum in section 5.2.1. An example of such a spectrum is shown in Figure 5.15a. In contrast to the charge spectrum in Figure 5.3, the pedestal peak is not shown, due to a detection threshold of $A = 0.25\,\mathrm{pe}$ used in the peak finding algorithm. The fluctuation in the single pixel amplitude

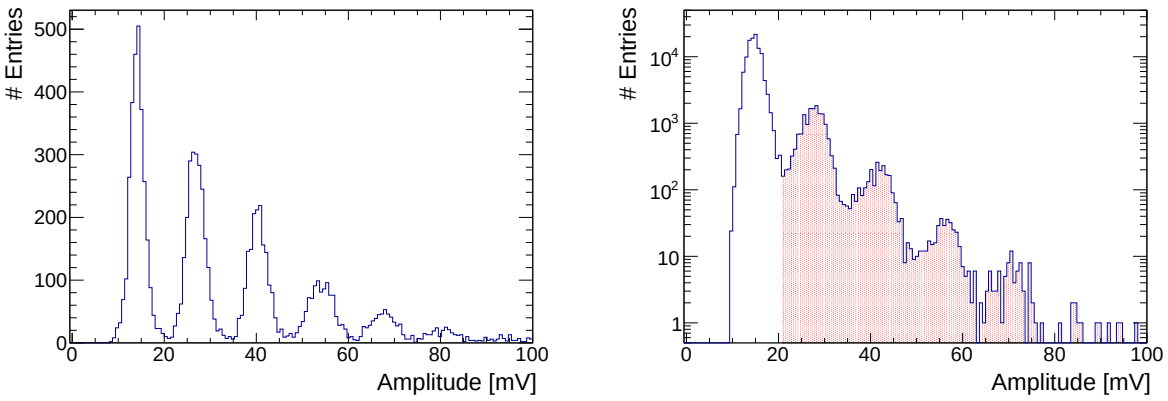

(a) **(b)**

Figure 5.15.: (a) Exemplary amplitude spectrum at low light intensities. The first peak corresponds to the single pixel signal amplitude. The pedestal peak is not shown, due to a detection threshold of $A = 0.25\,\mathrm{pe}$ used in the peak finding algorithm. **(b)** Exemplary dark-rate amplitude spectrum. The entries in the second and higher peaks (shaded red) correspond to cross-talk events.

$\sigma_{A_{sp}}$ is determined from the broadening of the width of the individual peaks, similar to the determination of the gain fluctuations σ_G in section 5.2.1:

$$\sigma_{A_{sp}} = \sqrt{\sigma_{2pe}^2 - \sigma_{1pe}^2}, \tag{5.22}$$

where σ_{1pe} and σ_{2pe} is the width of the first and second peak in the spectrum. The factor $\sigma_{A_{sp}}/A_{sp}$ is equivalent to the excess noise factor σ_G/G.
The PDE is determined from the single pixel charge spectrum in the same way as described in section 5.2.1.

Cross-talk

The cross-talk parameter is determined from the amplitude spectrum of dark-rate pulses. An example of such a spectrum is shown in Figure 5.15b. Pulses which occur within a time interval of $t < 50\,\mathrm{ns}$ after the preceding pulse are excluded from the spectrum. This selection rejects signals of not fully recovered pixels, which would smear out the peaks in the amplitude spectrum. As discussed in section 5.2.1, signals with an amplitude of two or more pixel signals correspond to cross-talk events. In Figure 5.15b, these events are indicated by the red shaded area. The probability for an avalanche to trigger least one cross-talk signal is therefore given by:

$$P_{ct}^{n\geq 1} = \frac{N_{tot} - N_{1pe}}{N_{tot}}, \tag{5.23}$$

where N_{1pe} is the number of events in the first peak and N_{tot} is the total number of events in the spectrum. The simulation parameter P_{ct} is obtained via Equation 5.14.

Dark-rate and After-pulsing

The input parameters for the dark-rate and after-pulses are obtained via the dark-rate time spectrum, similar to the method discussed in section 5.2.1. The waveform analysis allows for a more accurate determination of the time spectrum, compared to the measurement in section 5.2.1.

One of the main advantages is that the analysis algorithm allows to detect consecutive pulses occurring within a much shorter time interval of down to $t = 10\,\text{ns}$. Furthermore, the following selection criteria can be applied to improve the spectrum quality. Considering two consecutive dark-rate pulses with the amplitudes A_1, A_2 and timestamps t_1, t_2, the first pulse of the pair is required to have an amplitude of $A_1 = A_{sp} \pm \sigma_{A_{sp}}$, in order for the time interval $t = t_2 - t_1$ to be considered for the time spectrum. This selection criteria reject events where an after-pulse originates from an optical cross-talk event. In addition, only pulse pairs are selected which occur at least 200 ns after preceeding pulse. This suppresses events where the after-pulse is not generated by the first pulse of the pair, but a pulse prior to this. The resulting spectrum is well described by the analytical function in Equation 5.12. The dark-rate and after-pulse parameters thus can directly be extracted by fitting the spectrum with this function. In contrast to the measurement in section 5.2.1, the time spectrum is well described by a single after-pulse component, which presumably is related to the more recent MPPC product line, which features an overall improved noise behaviour.

Avalanche Jitter

The avalanche jitter σ_{av} is obtained from the measurement of the single pixel time resolution (SPTR). However, σ_{av} cannot be determined directly from this measurement, since the electronic noise and pileup from dark-rate pulses also contribute to the SPTR. Experimentally it is difficult to disentangle these contributions. Therefore, the simulation is used to extract the value for the avalanche jitter σ_{av} from the SPTR. Since the electronic noise and dark-rate parameters σ_{en} and τ_{tp} are determined in independent measurements, the avalanche jitter can be extracted by fitting the simulation to the measured SPTR. This is done by iterative variation of the input parameter σ_{av}, which yields a value of $\sigma_{av} = (100 \pm 50)\,\text{ps}$. This is consistent with the typical values measured for MPPC devices [73, 89, 90, 102].

Single Pixel Pulse Shape and Bandwidth

The single pixel pulse shape is approximated with a double exponential function. The decay constant of the signal tail of $\tau_d = (25 \pm 1)\,\text{ns}$ is extracted from the recorded signal waveforms. For the rise time constant a typical value of $\tau_r = 100\,\text{ps}$ is assumed. However, the signal rise time measured with the DSO is essentially determined by the bandwidth of the setup. Therefore, the bandwidth limitation has to be considered in the simulation, in order to accurately model the SiPM timing behaviour.
The bandwidth of the setup is modelled with a Butterworth filter [103], which is realised via digital signal processing using recursive filters (IIR filter). These filters are characterised by a flat frequency response up to a certain cutoff frequency ν_c, while frequencies above ν_c are suppressed. The sharpness of the cutoff is described by the filter order $n = 1, 2, 3...$, where for small values of n the cutoff is less sharp. It should be noted, that the Butterworth filter is expected to only provide a first order approximation of the real frequency response of the setup. The measured single pixel waveform is best described using a filter of second order and a cutoff frequency of $\nu = (250 \pm 30)\,\text{MHz}$. This bandwidth limitation arises from the cables and connectors used in the setup.

Electronic Noise

The electronic noise σ_{en} on the measured signal is dominated by the vertical resolution of the DSO. The noise generated by the SiPM itself due to leakage currents is negligible. In general,

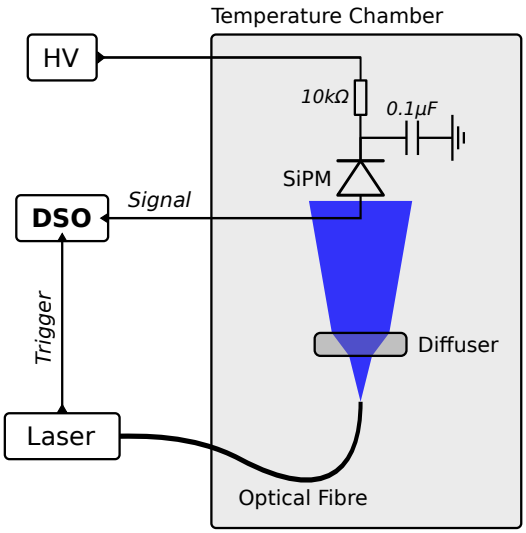

Figure 5.16.: Schematic view of the setup for the measurement of the response curve. The SiPM is uniformly illuminated by a fast laser pulse. The SiPM signal is read out with a digital storage oscilloscope (DSO). The time resolution is determined by the RMS of the time interval between the SiPM signal and the trigger signal generated by the laser controller.

the vertical resolution of a DSO is frequency dependent. For very low frequencies, the resolution is basically determined by the voltage quantisation associated with the number of bits of the Analogue-to-Digital Converter (ADC) of the DSO. For higher frequencies, the resolution usually is significantly degraded [104–106]. This effect is quantified by the *Effective Number of Bits* (ENOB), which characterises the vertical resolution for a certain frequency.
The resolution of the used DSO is estimated by measuring the RMS of the amplitude of a sinusoidal signal which is generated by an arbitrary waveform generator. In the frequency range of (100-500) MHz, the vertical noise is measured to be $\sigma_{en} = (0.4 \pm 0.1)\,\mathrm{mV}$. This corresponds to an ENOB of roughly 6.6 ± 0.4.

5.3.2. Measurement Setup

The setup for the measurement of the time resolution is sketched in Figure 5.16. The SiPM is illuminated by a short laser[1] pulse with a wavelength of $\lambda = 408\,\mathrm{nm}$ and a duration of about 25 ps. The light is guided to the SiPM via an optical single mode fibre. An engineered square pattern diffuser[2] is placed in the optical path in between the MPPC and the fibre end, in order to homogeneously distribute the light over the whole active area of the sensor. The SiPM signal is read out with the DSO, which digitises the signals with a sampling rate of 10 GSPS[3]. The timestamp of the signals are determined via a leading edge discrimination method, which uses linear interpolation between adjacent sampling points.
The time resolution of the SiPM signal is defined by the RMS of the time interval between the SiPM signal and the trigger signal generated by the laser controller. This value is corrected for the jitter of the trigger signal, which has been measured to be about $\sigma_{trig} = 4\,\mathrm{ps}$. The time resolution is measured for different signal amplitudes, which are associated to a certain laser intensity, and for different discrimination thresholds.

[1] A.L.S. PiLas PiL040 + EIG1000D Controller
[2] Thorlabs ED1-S20
[3] Giga-Samples Per Second

5.3.3. Results

Figure 5.17, Figure 5.19 and Figure 5.21 show the measured and simulated time resolution as a function of the signal amplitude for an over-voltage of $V_{ov} = 1.0\,\mathrm{V}$, $V_{ov} = 1.5\,\mathrm{V}$ and $V_{ov} = 2.0\,\mathrm{V}$. The discrimination threshold is set to 10 % of the average amplitude. The number of photons specified on the top axis is obtained using the simulation.
The simulation accurately models the measured time resolution for all three over-voltages. As in section 5.2.4, systematic uncertainty of the simulated resolution is associated with the uncertainties in the input parameters, primarily the cutoff frequency ν_c and the electronic noise σ_{en} of the DSO. The lower part of the figures shows the contributions of the SiPM parameters which dominate the time resolution. In contrast to the simulation of the charge response, the individual contributions cannot clearly be distinguished, since most parameters are not independent from each other. For example, a larger PDE not only improves the time resolution due to a better photon detection statistic, but the larger signal amplitude, and therefore steeper rising edge, reduces the jitter associated with the electronic noise. In order to obtain a qualitative measure of the different effects, the individual contributions are estimated by switching off the corresponding parameter in the simulation[1]. As an example, the contribution from electronic noise is determined via:

$$\frac{(\sigma_t^{en})^2}{(\sigma_t)^2} = \frac{(\sigma_t)^2 - (\sigma_t^{\not{en}})^2}{(\sigma_t)^2}, \tag{5.24}$$

where $\sigma_t^{\not{en}}$ is the simulated time resolution without electronic noise. It should be noted, that the individual contributions do not precisely add up to 100 %, due to the correlation between the different effects.
For this measurement, the three main limiting factors for the time resolution are the statistical fluctuations in the photon detection process related to the PDE, the electronic noise, which is essentially determined by the vertical resolution of the DSO, and the avalanche jitter. The overall resolution is well described by:

$$\sigma_t = \frac{\alpha}{N_{phot}} \oplus \frac{\beta}{\sqrt{N_{phot}}}. \tag{5.25}$$

The dashed line in Figure 5.17, Figure 5.19 and Figure 5.21 shows a fit of this function to the data. The first term is mainly determined by the electronic noise (see Equation 4.12), since the slope of the signal is in first approximation proportional to the signal amplitude, and therefore the number of photons N_{phot}. The second term predominantly describes the contribution from the PDE and the avalanche jitter (see Equation 4.13). The contributions from the PDE are mostly due to time-walk. Therefore, the time resolution indirectly probes the simulated amplitude distribution.
Figure 5.18, Figure 5.20 and Figure 5.22 show the time resolution as a function of the discrimination threshold. The laser intensity is adjusted to yield a signal amplitude of $A = 100\,\mathrm{mV}$, which approximately corresponds to the amplitude of the signals expected in the Tile Detector (see section 7.1). For high thresholds, the resolution is dominated by time-walk, which arises from the statistical fluctuation of the signal amplitude related to the PDE. The effect of optical cross-talk improves the time resolution for high thresholds. This can be explained by the steeper signal slope, which reduces the contribution from electronic noise and time-walk. For low thresholds, the resolution is dominated by the electronic noise. This can be explained by the reduced signal slope at the beginning of the waveform, which is caused by the limited bandwidth. The best

[1] In case of the PDE, the statistical fluctuations in the detection process were disabled.

resolution of about $\sigma_t = 18\,\text{ps}$ is achieved for a threshold of about 6 mV, which corresponds to about 30, 22 and 15 firing pixels for the respective over-voltages of $V_{ov} = 1.0\,\text{V}$, $V_{ov} = 1.5\,\text{V}$ and $V_{ov} = 2.0\,\text{V}$. It should be noted, that with readout electronics optimised for timing applications, a much higher bandwidth and a significantly lower electronic noise level can be achieved. In this case, a significantly better time resolution is obtained for lower thresholds.
The measurements presented in this section show, that intrinsic SiPM time resolution in response to a short 25 ps laser pulse is well below the targeted resolution for the Mu3e Tile Detector of $\sigma_t < 100\,\text{ps}$. This demonstrates, that SiPMs are in principle well suited for the Mu3e application. Furthermore, the measurement results verify, that the GosSiP simulation provides a good model of the SiPM time response. In the following chapters, the SiPM response in combination with a scintillator tile is discussed in the context of the Mu3e Tile Detector. In section 6.3, an extended simulation framework is presented, which includes the scintillator response. Measurements of time resolution of a combined scintillator-SiPM system are discussed in chapter 7.

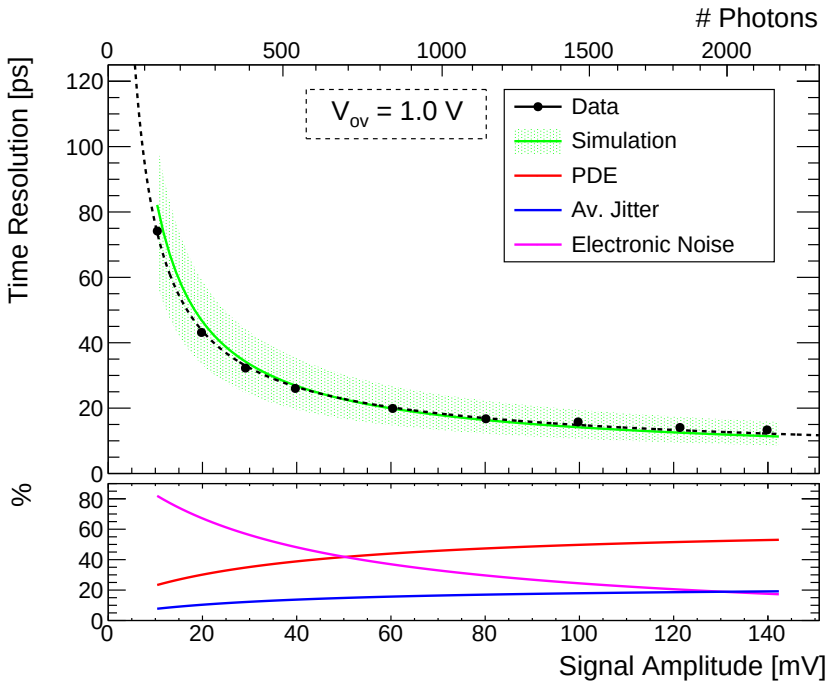

Figure 5.17.: *(Top)* Time resolution as a function of the signal amplitude for low operating voltage ($V_{ov} = 1.0\,\mathrm{V}$). *(Bottom)* Contribution from different parameters.

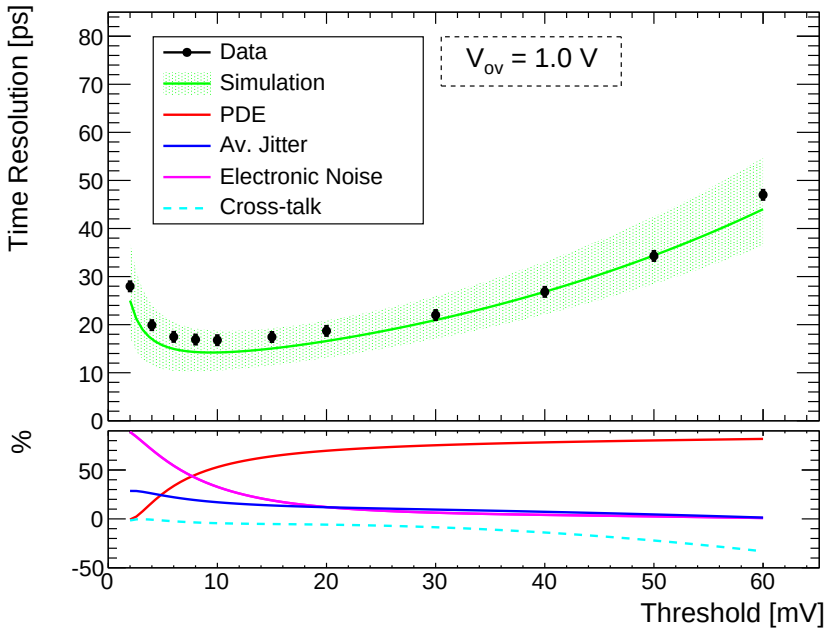

Figure 5.18.: *(Top)* Time resolution as a function of the discrimination threshold for low operating voltage ($V_{ov} = 1.0\,\mathrm{V}$). *(Bottom)* Contribution from different parameters.

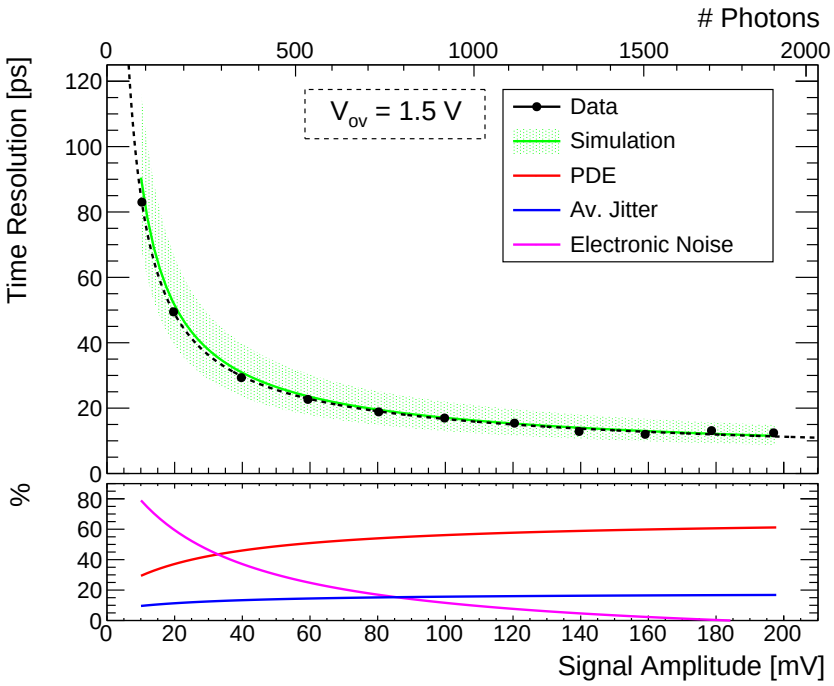

Figure 5.19.: *(Top)* Time resolution as a function of the signal amplitude for medium operating voltage ($V_{ov} = 1.5\,\mathrm{V}$). *(Bottom)* Contribution from different parameters.

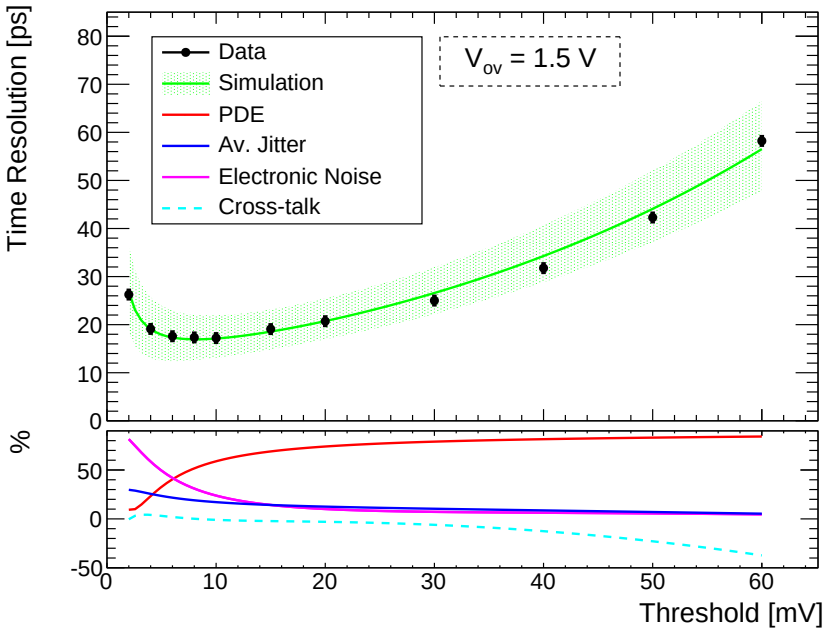

Figure 5.20.: *(Top)* Time resolution as a function of the discrimination threshold for medium operating voltage ($V_{ov} = 1.5\,\mathrm{V}$). *(Bottom)* Contribution from different parameters.

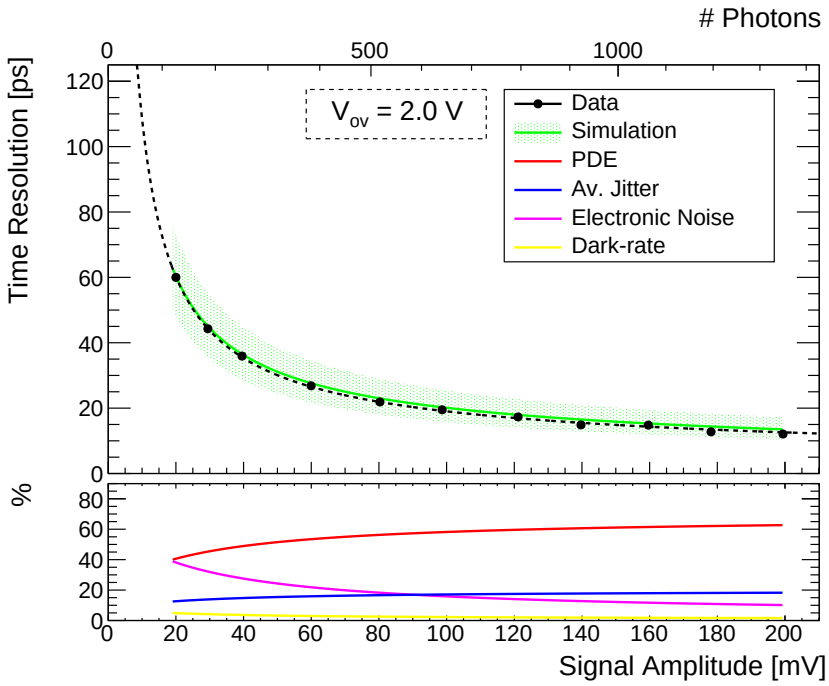

Figure 5.21.: *(Top)* Time resolution as a function of the signal amplitude for high operating voltage ($V_{ov} = 2.0\,\mathrm{V}$). *(Bottom)* Contribution from different parameters.

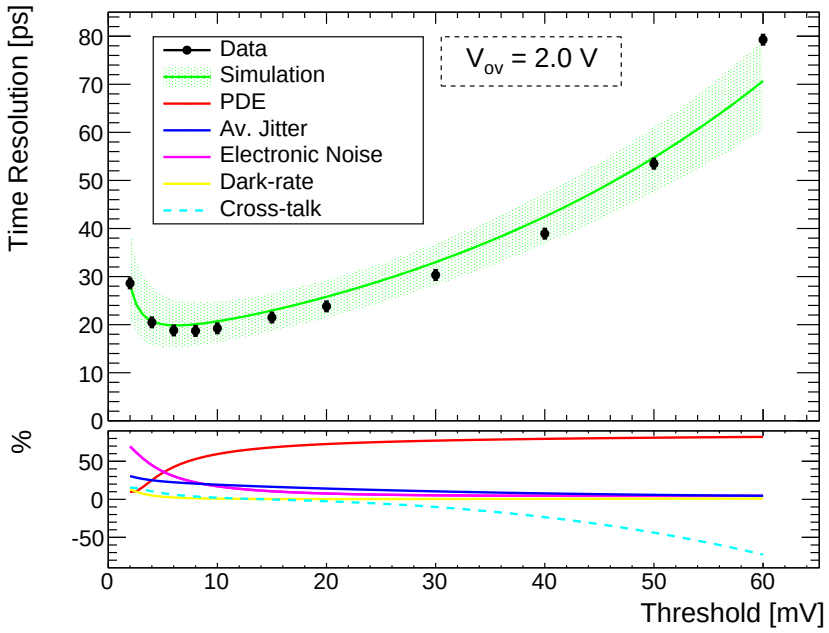

Figure 5.22.: *(Top)* Time resolution as a function of the discrimination threshold for high operating voltage ($V_{ov} = 2.0\,\mathrm{V}$). *(Bottom)* Contribution from different parameters.

6. Mu3e Tile Detector Simulation & Design

Within this thesis, the detector concept of the Mu3e Tile Detector has been developed and studied. This chapter presents a baseline technical design of the detector, as well as detector simulations, which are used to estimate and optimise the detector performance. Preliminary results of these studies have been published in the *Mu3e Research Proposal* [7]. The following studies primarily focus on the upcoming phase Ib of the experiment.

6.1. Detector Concept

One of the main characteristics of the $\mu \to eee$ decay is the coincidence of the three electron tracks. The purpose of the Tile Detector is to measure the timestamps of the electrons with high precision, in order to identify the prompt signal decays and reject the non-coincident accidental background. It should be noted, that variations in the time-of-flight associated with different particle trajectories can result in a significant spread $\mathcal{O}(1\,\text{ns})$ of the timestamps measured in the Tile Detector. However, the time-of-flight delay can be precisely determined from the particle trajectories measured with the pixel detector, with an expected resolution of below 10 ps. In the following, this time-of-flight correction is always implied.
The Tile Detector is planned to be installed in phase Ib of the experiment, where due to the increased muon rate of about 100 MHz, the precise timing information is needed to suppress accidental background. As shown in Figure 6.1, there are two identical Tile Detector segments, which are located in the two re-curl stations inside of the pixel layers. The detector consists out of plastic scintillator, which is segmented into small tiles. Each tile is read out with a Silicon Photomultiplier, which is directly attached to the scintillator.

Performance Requirements

The key parameter for the Tile Detector is the time resolution, which is required in order to suppress the accidental background to a level of below 10^{-16} per muon decay. The suppression factor associated with the time resolution is determined by the probability for three random tracks to occur within a certain coincidence window Δt_{cw}. In the following, this is referred to as

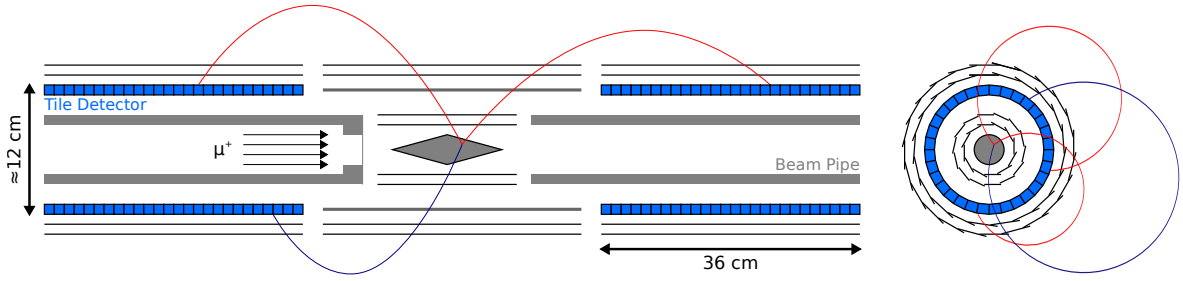

Figure 6.1.: Schematic view of the Mu3e experiment in phase Ib in z *(left)* and ϕ *(right)* direction. The Tile Detector is located in the re-curl stations and is enclosed by the pixel layers. The detector is segmented into small scintillator tiles, which are coupled to SiPMs.

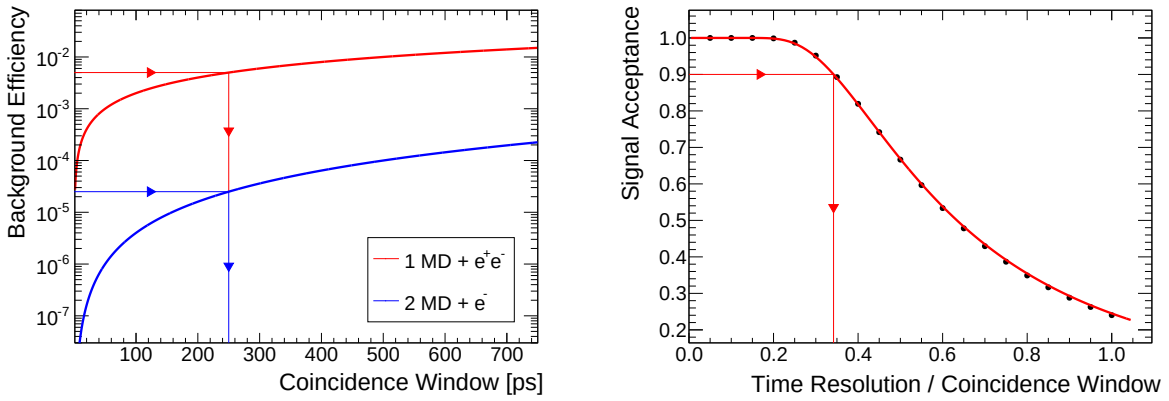

(a) **(b)**

Figure 6.2.: (a) Accidental background efficiency for one Michel decay (MD) plus an e^+e^- pair (red) and two Michel decays plus one e^-. The aimed background suppression is achieved for a coincidence window of $\Delta t_{cw} = 250\,\text{ps}$. **(b)** Signal acceptance ε_{cw} as a function of the time resolution σ_t relative to the coincidence window Δt_{cw}. An acceptance of 90 % is reached for a time resolution of about $0.34 \cdot \Delta t_{cw}$.

the *background efficiency* η_t. As discussed in section 2.4.2, the accidental background can be grouped into processes with one Michel decay overlaying with a prompt e^+e^- pair (1 MD + e^+e^-) and processes with two Michel decays overlaying with an electron (2 MD + e^-). The background efficiency for these processes is determined by the coincidence window and the time interval of the readout frame Δt_{rf} considered for the event reconstruction (see section 2.4.2):

$$\eta_t' = \Delta t_{cw}/\Delta t_{rf} \qquad \text{for 1 MD + } e^+e^- \text{ , and} \tag{6.1}$$

$$\eta_t'' = (\Delta t_{cw}/\Delta t_{rf})^2 \qquad \text{for 2 MD + } e^- \text{ .} \tag{6.2}$$

The background efficiency for a readout frame of $\Delta t_{rf} = 50\,\text{ns}$ is displayed in Figure 6.2a as a function of the coincidence window. The most critical background is the overlay of a Michel decay together with an e^+e^- pair from a Bhabha scattering event in the target (see Table 2.2). In order to suppress this process to a level of 10^{-16} per muon decay, a background efficiency of about $\eta_t' < 5 \cdot 10^{-3}$ is required, in addition to the background suppression associated with the vertex and kinematic constraints (see section 2.5.1). This corresponds to a coincidence window of $\Delta t_{cw} = 250\,\text{ps}$. For 2 MD + e^- processes, this yields a background efficiency of $\eta_t'' < 2.5 \cdot 10^{-5}$, which sufficiently suppresses all associated backgrounds.
Besides the low background efficiency, the Tile Detector has to provide a high signal efficiency[1]. The signal efficiency ε is defined here as the probability to detect the three electrons from a signal decay within a certain coincidence window, given that all tracks lie within the acceptance of the tracking detector. This probability depends on several factors: the efficiency of the scintillation detection process ε_d, the efficiency for separating consecutive signals (pileup) ε_{pu}, the acceptance of the coincidence window ε_{cw} and the geometrical acceptance of the Tile Detector ε_{geo}:

$$\varepsilon = \varepsilon_d^3 \cdot \varepsilon_{pu}^3 \cdot \varepsilon_{geo}^3 \cdot \varepsilon_{cw}. \tag{6.3}$$

The efficiency of the scintillation detection process is essentially 100 %, due to the high light yield of the tiles. As discussed in the next sections, the signal produced by an electron in a scintillator tile corresponds to several hundred photons. Therefore, the probability for the

[1]The term 'signal efficiency' here refers to both efficiency and acceptance effects.

number of detected photons to fluctuate below a typical detection threshold of a few photons is negligible.
The geometrical acceptance ε_{geo} of the Tile Detector relative to the acceptance of the tracker is also essentially 100 %, since the Tile Detector covers the same region as the re-curl pixel layers. The influence of the non-sensitive areas in between neighbouring tiles, which are needed to isolate the individual cells, is negligible, since the electrons hit the detector at a certain angle (see Figure 6.14).
The acceptance ε_{cw} is defined as the probability to detect all three electrons of a signal decay within a certain coincidence window. Figure 6.2b shows the time resolution dependence of this parameter, which has been calculated using Monte Carlo methods. The relation is well described by the following parameterisation:

$$\varepsilon_{cw}(\sigma_t, \Delta t_{cw}) = \mathrm{Erf}(\frac{\Delta t_{cw}}{\sqrt{2} \cdot 1.5\sigma_t})^2, \tag{6.4}$$

where σ_t is the single hit time resolution. For a coincidence window of $\Delta t_{cw} = 250\,\mathrm{ps}$, a signal acceptance of 90 % is achieved for a time resolution of $\sigma_t = 0.34 \cdot 250\,\mathrm{ps} = 85\,\mathrm{ps}$. This defines the design goal for the time resolution of the Tile Detector.
The efficiency for separating consecutive signals ε_{pu} is related to the signal pileup P_{pu}, which is defined by the probability for a subsequent signal to occur within the dead-time of the channel. This is determined by the channel hit rate R and the dead-time Δt_{dt}:

$$P_{pu}(\Delta t_{dt}, R) = \int_0^{\Delta t_{dt}} R \cdot \mathrm{e}^{-t \cdot R}\,\mathrm{d}t = 1 - \mathrm{e}^{-\Delta t_{dt} \cdot R}. \tag{6.5}$$

In first approximation, the efficiency for separating consecutive signals is given by $\varepsilon_{pu} = 1 - P_{pu}$. Consequently, a low occupancy and a short channel dead-time are required, in order to achieve a high signal efficiency. The targeted pileup probability for phase Ib is $P_{pu} \approx 3\,\%$, which corresponds to a pileup separation efficiency of $\varepsilon_{pu}^3 \approx 90\,\%$.

6.2. Detector Design

This section presents the baseline concept of the technical design[1] of the Tile Detector, which has been developed within this thesis. The design is based upon the results of the optimisation studies presented in the next section. Moreover, the design has to respect the physical space requirements in the experiment, as well as the requirements of the readout electronics.
As described in section 2.5, the Tile Detector in phase Ib is subdivided into two identical segments - one in each re-curl station. In phase II, two additional segments will be added. Each Tile Detector segment has the shape of a hollow cylinder, which encloses the beam-pipe. The length of a segment is 36 cm in beam direction (z direction), thus covering the same length as the pixel layers. The outer radius is 6.3 cm, which is limited by the surrounding pixel sensor layers. The detector in each re-curl station is segmented into 60 tiles in z direction and 56 tiles along the azimuthal angle (ϕ direction). This is the highest channel density which seems feasible, considering the space requirements for the readout electronics (see below). The high granularity is essential, in order to achieve a low occupancy, as well as a high time resolution. This aspect is discussed more in detail in section 6.3.
The technical design of the Tile Detector is based on a modular concept, i.e. the detector is

[1] It should be noted that the experiment is still in the development phase, therefore minor adjustments to the detector design might still be necessary.

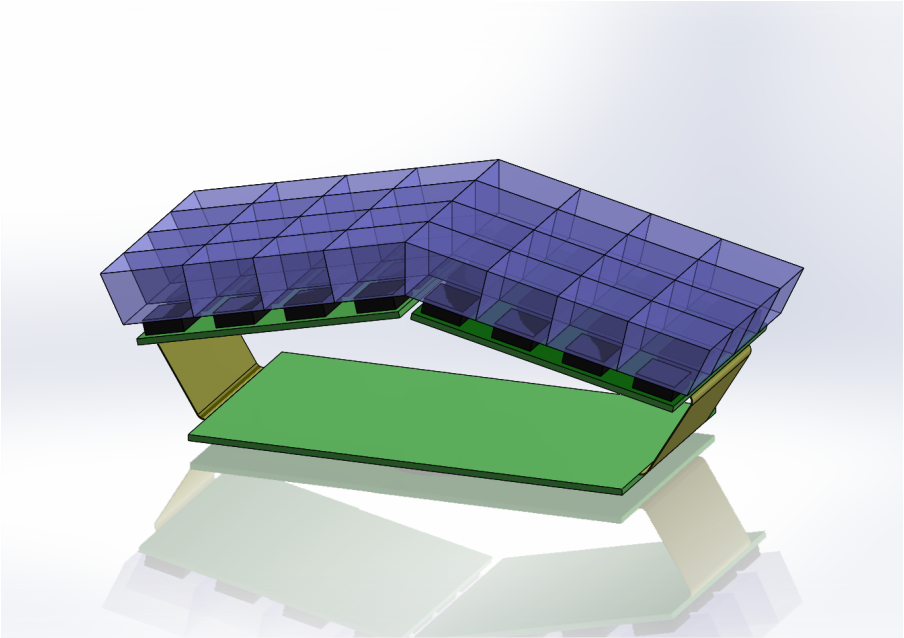

Figure 6.3.: Tile Detector submodule with 32 channels.

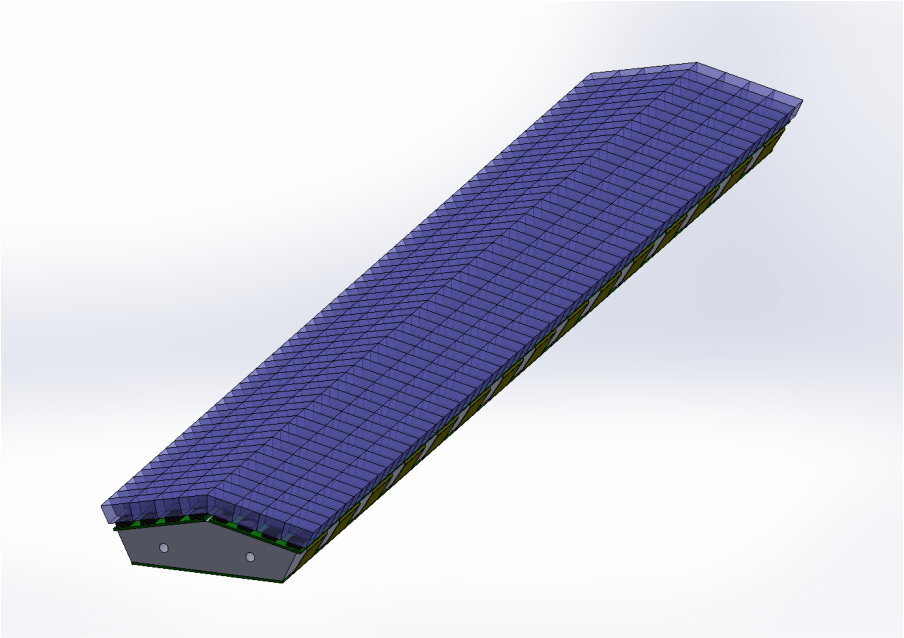

Figure 6.4.: Module consisting out of 15 submodules.

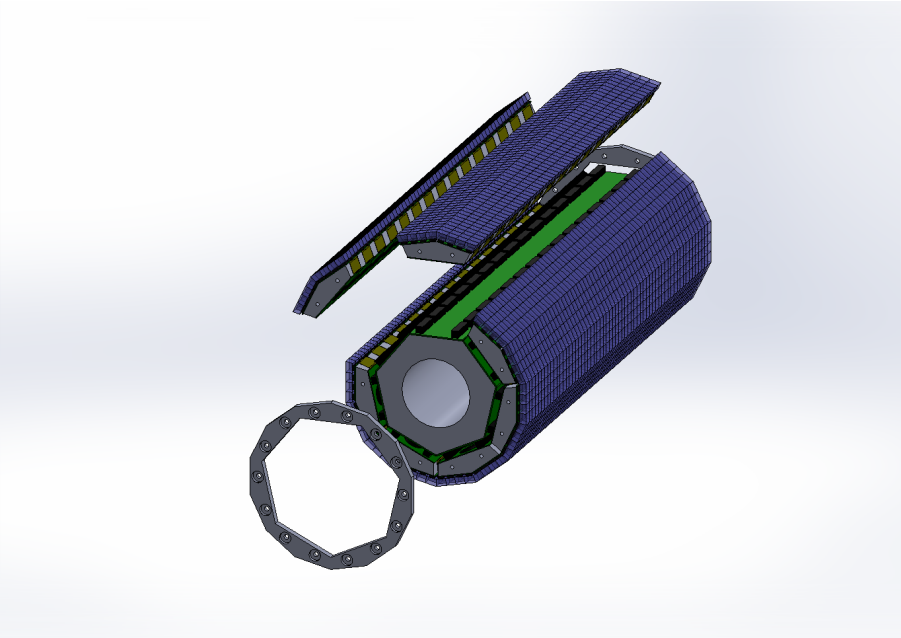

Figure 6.5.: Explode view of a full detector segment consisting out of seven modules.

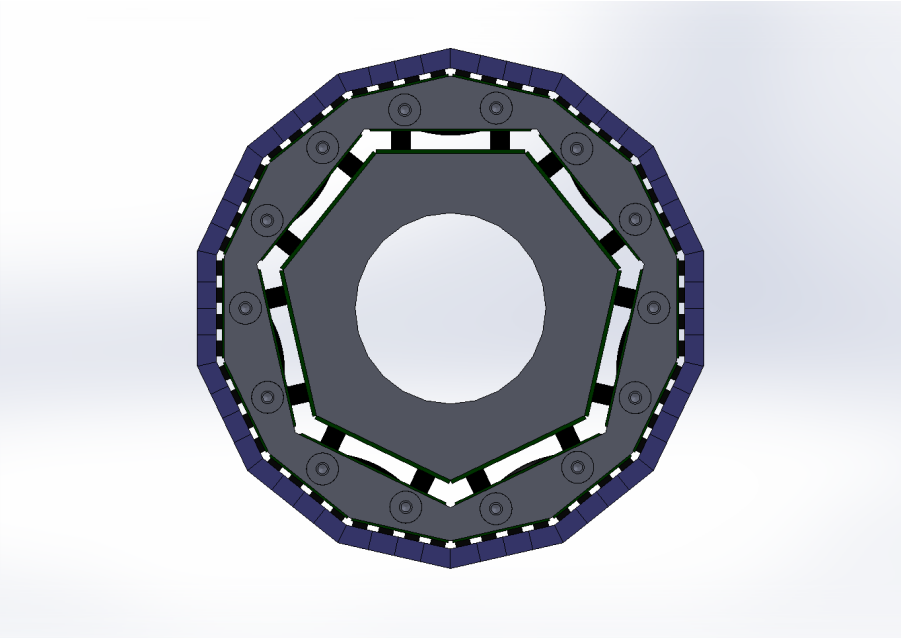

Figure 6.6.: Front view of a full detector segment.

build up out of small independent detector units. The base unit of the Tile Detector, referred to as *Submodule*, is shown in Figure 6.3. It consists out of 32 channels arranged in two 4×4 arrays. The tiles are made out of BC418 plastic scintillator and have a size of $6.5 \times 6.0 \times 5.0\,\mathrm{mm}^3$. The choice of the scintillator material and tile geometry are the result of the simulation studies presented below. The edges of the two outer rows of an array are bevelled by 25.7°, which allows for seven base units to be arranged in a circle. This seven-fold symmetry matches the heptagonal structure of the beam-pipe (see Figure 6.6).
The individual tiles are coated with reflective TiO_2 paint[1], in order to increase the light yield and optically isolate the channels. Every tile is read out by a $3 \times 3\,\mathrm{mm}^2$ MPPC (S12572-050P) with 3600 pixels[2], which is glued to the bottom $6.5 \times 6.0\,\mathrm{mm}^2$ side of the tile. At this interface, the scintillator is not painted. The SiPMs are soldered to a printed circuit board (PCB), which is connected via a flexible PCB (flex print) to a readout chip.
A stack of 15 Submodules constitute a *Module*, which comprises 480 channels. The drawing of such a Module is shown in Figure 6.4. The Submodules are mounted on a metal support structure, which is also used for the heat dissipation for the readout chips.
Figure 6.5 and Figure 6.6 show a drawing of a full Tile Detector segment, which consists out of seven Modules. The individual Modules are connected to a PCB mounted on the beam-pipe. This PCB hosts several FPGAs, which collect the data from the readout chips. The subsequent data transmission and processing is discussed in section 2.6.3.

6.2.1. Readout Electronics

STiC Chip

The baseline solution for the readout of the SiPM signals is the STiC[3] chip, which is a mixed-signal[4] ASIC[5] developed for the readout of SiPMs with the focus on Time-of-Flight applications [107]. A detailed description of the chip can be found in [108–110].
The core piece of the analog input stage is a fast discrimination unit with two tunable thresholds. The lower threshold, referred to as *timing threshold*, is used to determine the timestamp of the input signal via leading edge discrimination. The higher threshold, referred to as *energy threshold*, is used to determine the signal charge via the Time-over-Threshold (ToT) of the signal. The chip is designed in such a way that the ToT is directly proportional to the charge in a large range. The time and energy information is digitised via an integrated TDC with a bin size of 50 ps. The intrinsic time resolution of the chip has been measured to be $\sigma_{stic} \lessapprox 30\,\mathrm{ps}$ [109]. In section 7.2, the functionality of the chip is discussed in more detail.
An important feature of STiC is the capability to tune the voltage at each input terminals within a range of about 0.7 V. This allows to adjust the SiPM bias voltage and thereby compensate fluctuations in the detector response, which for example can arise due to temperature changes and channel-to-channel variations.
The chip version STiC2 has successfully been tested in a 16 channel prototype of a Submodule, which is discussed in section 7.2. The latest version of the chip (STiC3) features an additional zero pole cancellation circuit, which is designed to reduce the signal tail a factor of three. This results in a significantly reduced channel dead-time. In addition, this is expected to reduce

[1] EJ-510
[2] A promising alternative is a 14 400 pixel sensor (MPPC S12572-025) from the most recent MPPC series. This device has a similar PDE and features shorter pulses, which reduces signal pileup.
[3] **S**iPM **Ti**ming **C**hip
[4] Containing both analog and digital circuits
[5] Application Specific Integrated Circuit

the baseline fluctuations related to the SiPM dark-rate and thus slightly improve the time resolution. Further development of the chip is planned, in order to optimise the performance for the application in the Tile Detector; including for example an increased data rate of about 1 MHz per channel, which is required for phase II.

DRS Sampling Chip

An alternative readout solution considered for phase II is the DRS chip [111], which digitises the waveform of the SiPM signals. An advantage of the DRS readout is the flexible analysis of the signals, which for example allows for a better pileup detection, compared to the STiC chip. However, the realisation of this readout scheme is quite challenging, in particular due to the high data rate which has to be processed.
The chip version DRS4, which features a sampling rate of up to 5 GSPS, has been successfully tested with single detector tiles. The results of these tests are presented in section 7.1.1. However, the event rate for this chip is limited to roughly 100 kHz. Therefore, the successor chip DRS5 is currently being developed, and is designed to match the rate requirements of the Mu3e experiment. The new version is supposed to provide a dead-time less readout with an enhanced sampling rate of 10 GSPS.
In contrast to the STiC readout, the DRS chips would be located outside the detector in special crates, due to the significantly higher space requirements. The SiPM signal would have to be amplified and send to the readout chips via a few meters of cable. The signal waveforms would then be analysed on FPGAs, in order to extract the timing and energy information.

6.2.2. Detector Calibration & Monitoring Scheme

The calibration and monitoring of the detector response is crucial for achieving a high time resolution. A detailed study of the calibration and monitoring scheme is discussed in [112]. The main task of the calibration is to synchronise all channels. In particular, the delay arising from the length of the signal lines has to be corrected for. Furthermore, the energy dependence of the timestamps has to be characterised, in order to correct for time-walk effects. Besides the detector calibration, the monitoring of the detector response is required to assure a stable operation. This is necessary since the response is expected to vary over time, due to fluctuations in the ambient temperature and degradation of the SiPM response caused by radiation damage. For the calibration and monitoring, coincident signals are required. There are three processes which can be used for calibration and monitoring: internal conversion decays, e^+e^- pairs from Bhabha scattering and hit clusters from a single track. Coincident signals from internal conversion decays and e^+e^- pairs offer the most precise and direct way to calibrate the detector. However, since the event rate is relatively low, this method is not suitable for monitoring purposes and a fast detector calibration.
As discussed in section 6.3.2, a single electron track produces a small cluster of hits in the tiles with an average cluster size of about two. This can be exploited to inter-calibrate the tiles in a cluster since the signals are basically coincident, up to the time of flight between the individual tiles of a cluster of about 10 ps. Since all particle tracks can be used, this provides a fast way to calibrate and monitor the response. As this method is limited to the inter-calibration within one re-curl station, it is complementary to the global calibration with internal conversion decays.

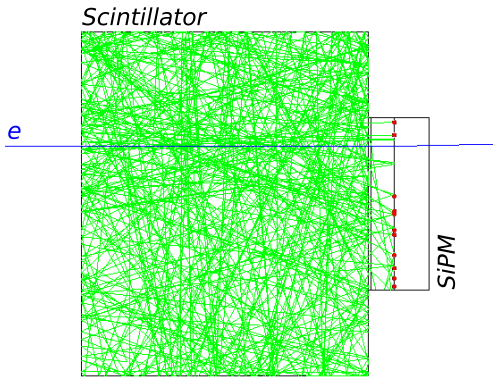

Figure 6.7.: Scintillator and SiPM simulation in Geant4. The electron trajectory is shown in blue; the trajectories of the scintillation photons are shown in green. Detected photons on the SiPM surface are indicated by the red points. The scintillation yield is significantly reduced for the sake of clarity.

6.3. Simulation Studies

Extensive simulation studies have been performed in order to optimise the detector design and demonstrate that the required performance in terms of time resolution and signal efficiency can be achieved. In the first subsection, the simulation of a single tile is discussed, which is used to optimise the time resolution. The second subsection describes the simulation of the full Mu3e experiment, which is used to determine the occupancy and pileup for the Tile Detector.

6.3.1. Scintillator-SiPM Simulation

A simulation of a single scintillator tile has been developed, which includes the modelling of the scintillation process, the optical properties of the tile, as well as the SiPM response. The simulation is used to study the time resolution for different tile geometries, scintillator materials, and SiPM types.

Simulation Setup

The scintillator tile, including the scintillation process and optical properties, is simulated using Geant4. For illustration, an example of a simulated event is depicted in Figure 6.7.
The surface of the scintillator tile is modelled as a diffuse Lambertian reflector with a reflectivity of 95 %. This emulates a coating with titanium dioxide paint. The surface properties are described using the data set of measured optical reflectance[1] which is provided in the Geant4 framework. The material parameters[2] and scintillation properties[3] of the tile are taken from the data sheet of the scintillator [63, 64]. A 100 µm thin layer of optical cement is placed in between the tile and the SiPM. The SiPM is described by a 500 µm thick protective layer of silicon dioxide and the silicon bulk. The complex index of refraction and the absorption length of the silicon and SiO_2 is taken from [113, 114]. The information about the wavelength, impact position and time of the photons which are absorpt in the silicon bulk are passed to the GosSiP simulation.

[1] PolishedTiOAir
[2] Density, chemical composition, optical absorption length and refractive index.
[3] Scintillation yield, rise and decay time.

Unless otherwise noted, the results presented in this chapter are obtained using the following default simulation configuration:

- **Particle Beam:** Single electrons with an energy of 30 MeV are simulated with a momentum direction perpendicular to the tile surface opposite to the SiPM. The impact position is distributed uniformly on the surface.
- **Tile:** The dimensions of the simulated tile are $6.5 \times 6.0 \times 5.0\,\mathrm{mm}^3$. The scintillator material is BC418.
- **SiPM:** A $3 \times 3\,\mathrm{mm}^2$ SiPM with a pixel size of 50 µm is simulated. The SiPM input parameters for an over-voltage of 1.5 V are taken from Table 5.2. The PDE value which enters the GosSiP simulation is corrected for photon reflection on the SiPM surface, since this process is already included in the Geant4 simulation of the tile. The input parameter $\mathcal{E}^{in}_{pde}$ is thus given by $\mathcal{E}^{in}_{pde} = \mathcal{E}_{pde}/(1 - R(\lambda))$, for which the wavelength dependent reflection probability $R(\lambda)$ is obtained from the simulation.
- **Readout Electronics:** A bandwidth of $\nu_c = 500\,\mathrm{MHz}$ and an electronic noise of $\sigma_{en} = 0.5\,\mathrm{pe}$ are assumed, which correspond to the values estimated for the STiC readout. The bandwidth filter is implemented as described in section 5.3.1. The timestamps are obtained via leading edge discrimination with a threshold of 3 pe. The intrinsic jitter of the STiC chip of $\sigma_{stic} \lessapprox 30\,\mathrm{ps}$ is not considered for this simulation.

Energy Deposition

Figure 6.8a shows the energy deposition of an electron in a PVT based plastic scintillator, relative to the covered distance. For particle energies above 10 MeV the energy deposition is essentially constant. This includes the energy range in the Mu3e experiment of (10-50) MeV. In this range, the electron behaves like a minimum ionising particle and is not stopped in the scintillator. It should be noted, that the total energy loss of the electron increases for high energies due to the radiation of high energetic photons. However, these gamma rays rarely interact with the scintillator, due to the low density of the plastic material and thus do not deposited energy in the tile.

SiPM Comparison

Different SiPM types have been compared in order to find the best suited device for the Tile Detector. One of the main distinguishing parameters is the size of the sensor. Commonly available sizes are $1 \times 1\,\mathrm{mm}^2$, $3 \times 3\,\mathrm{mm}^2$ and $6 \times 6\,\mathrm{mm}^2$. Figure 6.8b shows the number of photons hitting the sensor, as well as the estimated time resolution. The simulation of the time resolution is simplified by assuming identical SiPM properties for the different sensor sizes. An exception is the dark-rate parameter, which is scaled proportional to the sensor area.
The simulated time resolution improves with the SiPM size, due to the increasing number of detected photon. However, it should be noted, that the rise time of the SiPM signal is expected to decrease for larger sensors, due to the increasing detector capacity. This effect is not taken into account in this simplified study and is expected to slightly degrade the time resolution for larger sensor sizes. The increasing detector capacitance also results in a significantly longer decay time of the SiPM signal. Consequently, there is a tradeoff between a large photon signal and a short dead-time connected with the sensor size.
For the Tile Detector, a $3 \times 3\,\mathrm{mm}^2$ SiPM is chosen. This sensor size yields a sufficient photon

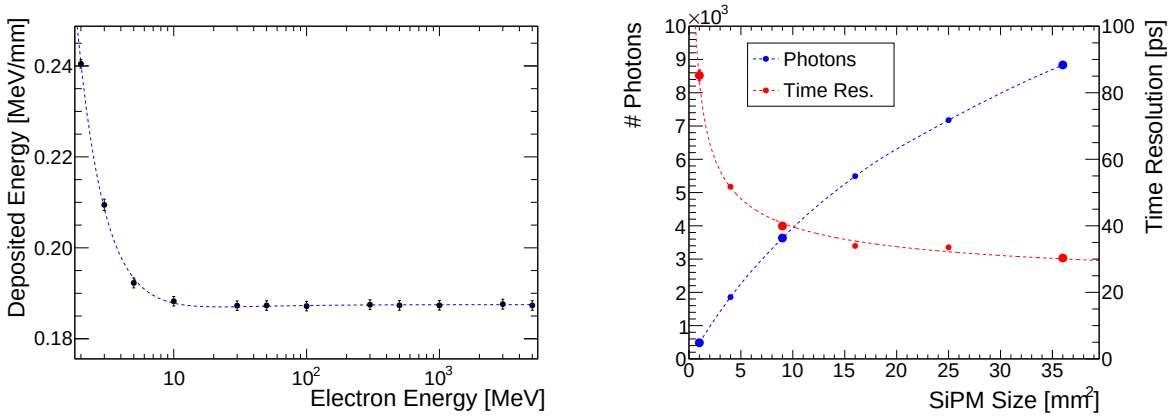

Figure 6.8.: (a) Simulated energy deposition in the scintillator tile as a function of electron energy. The deposited energy for the test-beam energies (1-5) GeV is identical (within <1 %) to the deposited energy for the energy range in the Mu3e experiment ((≈10-50) MeV). **(b)** Time resolution and number of photons hitting the SiPM as a function of the SiPM area. Commonly available SiPM sizes ($1 \times 1\,\mathrm{mm}^2$, $3 \times 3\,\mathrm{mm}^2$, $6 \times 6\,\mathrm{mm}^2$) are marked with larger data points.

signal and time resolution, while exhibiting a moderate signal decay time.
Another main SiPM characteristic is the number of pixels of the device. Typical pixel sizes are 100 µm, 50 µm and 25 µm[1]. For a device with a size of $3 \times 3\,\mathrm{mm}^2$, this corresponds to 900, 3600 and 14 400 pixels, respectively. Assuming a typical PDE of 35 %, the number of detected photons is expected to be about $N_{pe} = 3800 \cdot 0.35 \approx 1300$ (see Figure 6.8b). A 900 pixel device is hence not suited for this application, since the signal would strongly saturate at this light intensity. Smaller pixel sizes usually come along with a lower PDE, due to the reduced geometrical fill factor, which results in a degradation of the time resolution. Therefore, a SiPM with 50 µm pixel size is preferred over a device with 25 µm. A drawback of the larger pixel size is the larger pixel capacitance, which results in a longer signal decay time.
In the most recent SiPM series from Hamamatsu (MPPC S12572), a 25 µm pixel sensor is available which features a similar PDE as the 50 µm pixel device. This is a promising alternative to the baseline proposal of a MPPC with 50 µm pixel size. The performance of this device has to be verified in future detector prototypes.

Scintillator Comparison

Figure 6.9 shows the simulated signal waveforms and time resolution of the scintillator-SiPM system for different scintillator materials. Five different commercially available plastic scintillator materials[2], as well as an anorganic scintillator (LYSO) and a Cherenkov detector material (Sapphire) are compared. The Cherenkov detector inherently has the fastest response. However, the light yield of about 20 detected photons is relatively low, which results in a poor time resolution. In contrast, the anorganic scintillator provides a high light yield, corresponding to a signal amplitude of $A \approx 1500\,\mathrm{pe}$. However, the relatively slow response time of several tens of nanoseconds significantly limits the time resolution. Furthermore, the slow response leads to a higher pileup rate, which reduces the signal efficiency. Plastic scintillators offer both, a

[1] Recently, devices with even smaller pixels size down to 10 µm have become available.
[2] Most manufacturers offer akin scintillator materials.

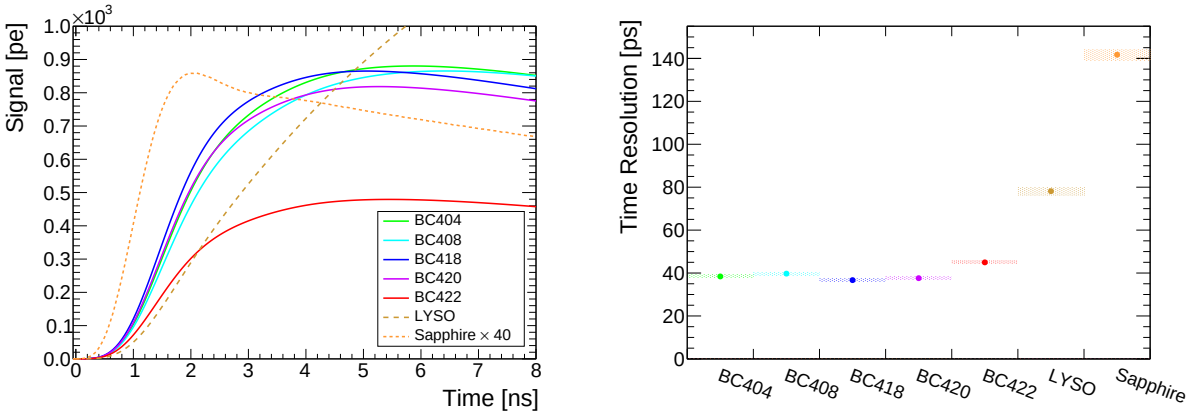

(a) **(b)**

Figure 6.9.: (a) Simulated SiPM signal for different scintillators and Sapphire for a $6.5 \times 6.0 \times 5.0\,\mathrm{mm}^3$ scintillator tile. The signal for Sapphire is scaled by a factor 40. **(b)** Simulated time resolution obtained for the different scintillators. The best resolution is achieved with the plastic scintillator BC418.

relatively high light yield, corresponding to $A \approx 900\,\mathrm{pe}$, and a fast response. This results in an excellent time resolution for the given application. The differences between the studied plastic scintillators is rather small. The best resolution is achieved with BC418, which has both a high light yield and fast response time (see Table 3.1), and therefore is chosen as the baseline material for the Tile Detector.

Tile Dimensions

Figure 6.10a shows the time resolution as a function of the Tile Detector granularity, i.e. the number of tiles in z and ϕ direction, N_z and N_ϕ. The associated tile dimensions (length and width) are listed in Table A.2. Three different configurations are shown: one where the number of tiles N_z equals N_ϕ (blue curve) and two where the number of tiles in φ and z direction is fixed to 56, respectively (green & red curve). The time resolution improves for a smaller tile dimensions, since the relative surface covered by the SiPM increases, which results in an enhanced light collection efficiency. The time resolution is approximately proportional to the tile dimensions:

$$\sigma_t(N_{\phi,z}) = \frac{\alpha}{N_{\phi,z}} \oplus C, \tag{6.6}$$

where $1/N_{\phi,z}$ is proportional to the length and width of the tile. Consequently, the highest possible granularity is desired for the Tile Detector. However, the granularity is limited by the maximum channel density which can be realised, particularly considering the physical space constraints in the experiment. The maximum granularity which seems feasible is $N_\phi = 56$ and $N_z = 60$, which results in 3360 channels per re-curl station, and a tile size[1] of $6.5 \times 6.0\,\mathrm{mm}^2$. Figure 6.10b shows the time resolution as a function of the tile height. The tile height essentially determines the path length of the electron in the scintillator tiles. Consequently, the time resolution improves with the tile height, due to the increasing number of scintillation photons (see Equation 5.25). However, for tile heights larger than about 5 mm the resolution is approximately constant. This effect is attributed to the increasing fluctuations in the light collection process, which is related the larger tile dimensions, as well as the saturation of the SiPM signal.

[1] Considering the heptagonal arrangement depicted in Figure 6.6.

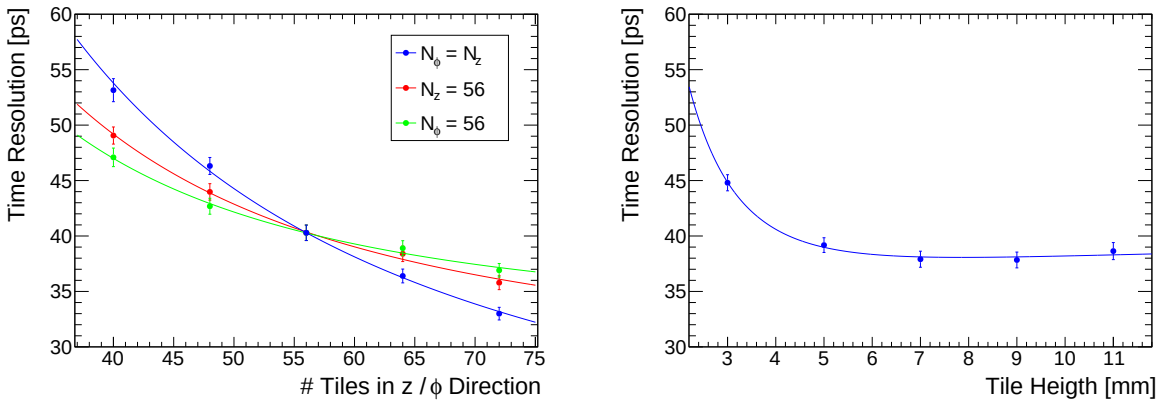

(a) **(b)**

Figure 6.10.: (a) Tile time resolution as a function of the number of tiles in ϕ and z direction. The resolution is approximately proportional to the tile length $l \propto 1/N_\phi$ and width $w \propto 1/N_z$. **(b)** Tile time resolution as a function of the tile height. For large tile heights, the resolution is limited by fluctuations in the light collection process related to the larger tile dimensions, as well as the saturation of the SiPM signal.

Time Resolution Energy Dependence

Figure 6.11 shows the relation between the time resolution and the energy deposited in the scintillator. The different energy bins are obtained by randomising the impact angles of the electrons according to the angular distribution in the Mu3e experiment shown in Figure 6.14. This angular distribution is obtained using the Tile Detector simulation described in the next section. The resulting energy distribution is equivalent to the one shown in see Figure 6.15a. Energy depositions above $E \approx 1\,\text{MeV}$ belong to electrons which traverse the full height of the tile. Smaller energy deposition are associated to edge effects, where the electron enters or leaves the tile at the side. The time resolution can be approximated by:

$$\sigma_t(E) = \varsigma/\sqrt{E}, \tag{6.7}$$

with $\varsigma \approx 30\,\text{ps}\,\text{MeV}^{-\frac{1}{2}}$. In contrast to the measurements in section 5.3, the term proportional to $1/E$ is negligible. This can be explained by the significantly lower electronic noise and the larger bandwidth assumed in this simulation.
For an average energy deposition of $E = 1\,\text{MeV}$, the time resolution obtained in the simulation is about $\sigma_t = 30\,\text{ps}$. Taking into account the intrinsic jitter of the STiC chip of $\sigma_{stic} \approx 30\,\text{ps}$, a resolution of about $\sigma_t \approx 42\,\text{ps}$ is achieved, which is well below the design goal of $\sigma_t = 85\,\text{ps}$. Assuming a coincidence window of $\Delta t_{cw} = 250\,\text{ps}$, this yields an signal acceptance of $\varepsilon_{cw} \approx 100\,\%$.

6.3.2. Full Detector Simulation

A detailed simulation of the Mu3e experiment is essential for multiple aspects of the project, like the optimisation of the detector, development and optimisation of the event reconstruction, background simulation and sensitivity studies, as well as the final data analysis. Within this thesis, the Tile Detector has been implemented in the Geant4 simulation of the Mu3e experiment, which is discussed in the following section. In the subsequent sections, the simulation is used to study the hit topology and channel occupancy, which determines the pileup probability and the associated signal efficiency.

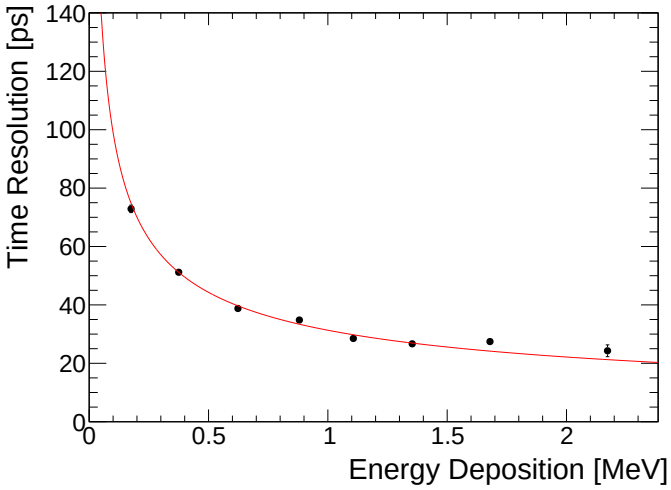

Figure 6.11.: Simulated time resolution as a function of the energy deposited in the tile. The time resolution is in good approximation proportional to $1/\sqrt{E}$.

Simulation Setup

The Tile Detector design described in section 6.2 has been implemented in Geant4 simulation of the Mu3e experiment. The geometry and response parameters of the detector can be varied in order to study different detector configurations. Figure 6.12 show an example of a simulated event in the detector.

Response Parameterisation

In the full detector simulation, the simulation of individual scintillation photons is not feasible, since this would significantly increase the computing time. Therefore, the scintillator response of the tile has to be parameterised. In principle, the GosSiP framework can be used to simulate the SiPM signal for every individual channel (see Figure A.4 for an example). However, this also requires a rather long computation time. Therefore, a parameterised model is used to describe the response of the tile, including the scintillation process, SiPM response, as well as the functional behaviour of the STiC readout chip. The parameterised response characteristics

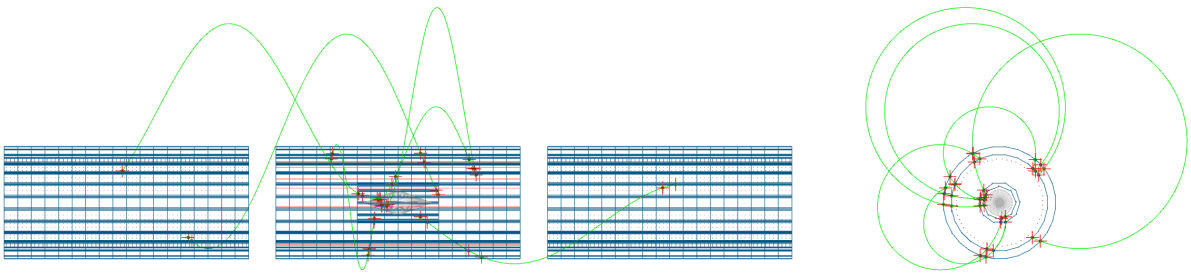

(a) **(b)**

Figure 6.12.: Geant4 simulation of the phase Ib Mu3e experiment, including the Tile Detector as described in section 6.2. The sketch shows simulated events in a 50 ns time frame with a viewpoint in z **(a)** and ϕ **(b)** direction. The hits in the fibres and pixel layers are indicated in red.

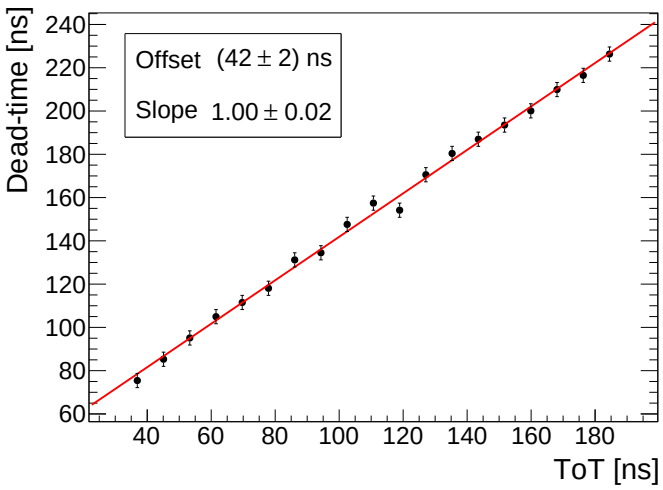

Figure 6.13.: Measurement of the channel dead-time using STiC2 [112]. The dead-time is directly related to the ToT of the signal.

are the time and energy resolution, the channel dead-time and the detection threshold. The parameters are obtained with the help of the scintillator-SiPM simulation discussed in the last section, as well as the test-beam data presented in chapter 7.
In order for a signal to be detected by the readout electronics, a minimum energy deposition is required. This corresponds to the energy threshold of the STiC chip, which is assumed to be roughly $E = 0.1\,\text{MeV}$. The energy resolution of the detected signals is described by:

$$\sigma_E(E) = 12\,\% \cdot E, \tag{6.8}$$

where E is the energy deposition in the tile. The value for the energy resolution is essentially given by the resolution of the STiC chip [109]. The contribution from fluctuations in the number of detected photons is given by $\sigma_E/E \propto 1/\sqrt{N_{pe}}$. This is below 4 % for the expected light yield and is therefore neglected.
Figure 6.13 shows the dead-time of a single channel measured with STiC2. The details of the measurement setup are discussed in [112]. The time-over-threshold (ToT) value[1] is approximately proportional to the energy deposited in the tile. The measured dead-time is equivalent to the ToT value, with an additional offset of 42 ns. It can thus be concluded, that the dead-time is essentially determined by the time interval in which the SiPM signal is above the discrimination threshold. The additional 42 ns offset can be explained by the dead-time of the TDC. In the measurements with a detector prototype presented in section 7.2, a mean ToT value of about 220 ns is obtained. The energy deposition in these measurements is approximately $E = 1.4\,\text{MeV}$ (see section 7.1). Assuming a perfectly linear relation[2] between the deposited energy and the ToT value, the dead-time is parameterised by the following equation:

$$\Delta t_{dt}(E) = 220\,\text{ns} \cdot \frac{E}{1.4\,\text{MeV}} + 42\,\text{ns}. \tag{6.9}$$

It should be noted, that the dead-time is expected to improve significantly with STiC3, due to the zero pole cancellation circuit.

[1] ToT of the energy threshold.
[2] The ToT pedestal value is not precisely know, but is expected to be smaller than $|ToT| < 20\,\text{ns}$.

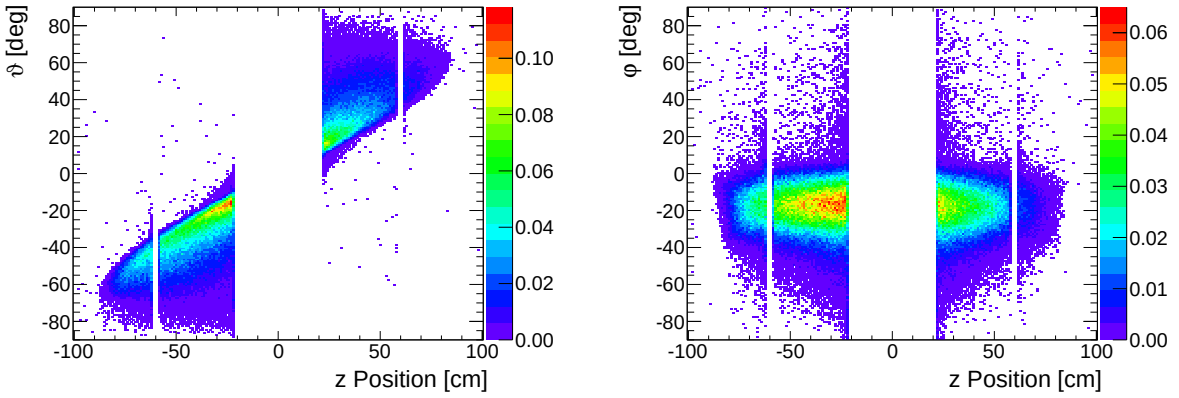

(a) **(b)**

Figure 6.14.: Distribution of the electron impact angles ϑ **(a)** and φ **(b)** as a function of the z position of the impact point.

The energy dependence of the time resolution is parameterised using the simulation data shown in Figure 6.11. In addition, the intrinsic resolution of the STiC chip is considered. This jitter is estimated to be $\sigma_{stic} \lessapprox 30\,\text{ps}$ [109] and does not depend on the energy. The total resolution therefore is parameterised by the following equation:

$$\sigma_t(E) = \frac{\varsigma}{\sqrt{E}} \oplus \sigma_{stic}. \tag{6.10}$$

The parameter ς is determined from the time resolution measured with the detector prototype described in section 7.2. For the estimated energy deposition of $E = 1.4\,\text{MeV}$ and the best achieved time resolution of $\bar{\sigma}_t = 56\,\text{ps}$, ς is given by:

$$\varsigma = (56\,\text{ps} \ominus \sigma_{stic}) \cdot \sqrt{1.4\,\text{MeV}} \approx 56\,\text{ps}\,\text{MeV}^{-\frac{1}{2}}. \tag{6.11}$$

It should be noted, that the time resolution achieved in the measurement is degraded with respect to the simulation results shown in Figure 6.11. This is explained by several reasons, for example a larger tile dimension and inferior scintillator material used in the measurement (this is discussed in detail in chapter 7). The above parameterisation of the time resolution hence is an conservative estimate.

Hit Topology

Figure 6.14 shows the distribution of the impact angles φ and ϑ of the electron tracks, obtained from the Tile Detector simulation. The angle ϑ is defined by the z component of the momentum vector $\vec{p}$ at the impact point:

$$\vartheta = \arcsin\left(\frac{p_z}{|\vec{p}|}\right). \tag{6.12}$$

The absolute value of this angle increases with the distance from the target (at $z = 0$), since the impact position in z direction is strongly correlated with the momentum fraction p_z. The average angle is approximately $|\bar{\vartheta}| = 38°$.
The angle φ is defined by the x and y component of the momentum vector relative to the tile surface normal $\vec{r}$:

$$\varphi = \text{atan2}\,(-r_y, -r_x) - \text{atan2}\,(p_y, p_x)\,. \tag{6.13}$$

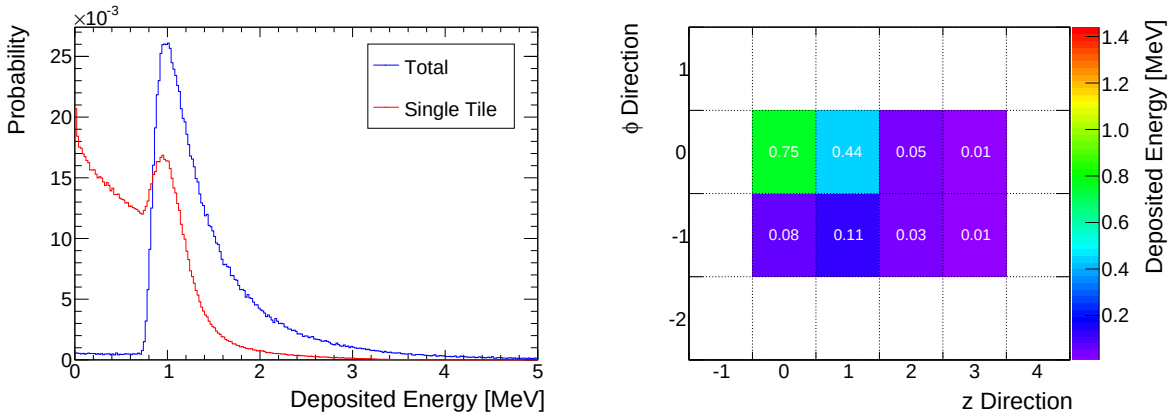

(a) **(b)**

Figure 6.15.: (a) Energy deposition of a positron. *Blue:* total energy in the detector. *Red:* energy in a single channel. **(b)** Distribution of the energy in a hit cluster for a positron. The particle impinges at $\phi = 0, z = 0$ with a momentum in z direction. For an electron, the distribution is mirrored along $\phi = 0$, due to the reverse rotational direction.

This angle does not depend on the impact position. The average value is about $\bar{\varphi} = -19°$.
Figure 6.15a shows the distribution of the energy deposition in the Tile Detector. The total deposited energy in the detector (blue curve) follows a Landau distribution with a mean value of $E = 1.4\,\text{MeV}$. Due to the non-zero impact angle of the electrons, the total energy deposition is usually distributed over several neighbouring cells. The energy deposition in a single tile of such a hit cluster is shown by the red curve in Figure 6.15a.
The distribution of the energy in a hit cluster for a positron track is shown in Figure 6.15b. For an electron, the distribution is mirrored along $\phi = 0$, due to the reverse rotational direction in the magnetic field. The average energy deposition in the first tile ($z = 0, \phi = 0$) is about $E = 0.75\,\text{MeV}$, which is roughly 54 % of the mean total energy deposition. About 31 % of the energy is deposited in the neighbouring tile in z direction, where here the z direction is defined to always point away from the target. The average energy deposition in the neighbouring tiles in $-\phi$ direction is relatively small, due to the smaller impact angle $\bar{\varphi}$, compared to $\bar{\vartheta}$.
The average size of a hit cluster n_c comprises approximately two tiles (see also Figure A.5 and Figure A.6). Since the average scattering angle of the electrons in the scintillator is small, the cluster size is essentially determined by the electron impact angle ϑ, φ and dimensions of the tiles:

$$n_c \approx 1 + \left[\frac{\tan(\vartheta)}{w} + \frac{\tan(\varphi)}{l}\right] \cdot h, \tag{6.14}$$

where l, w, h are the length, width and height of the tiles. The time information of the individual hits in a cluster can be combined, in order to retain the best possible time resolution:

$$\begin{aligned} \bar{t} &= \frac{\sum_i (E_i \cdot t_i)}{E_{tot}} \\ \Rightarrow \sigma_{\bar{t}} &= \frac{\varsigma}{\sqrt{E_{tot}}} \oplus \sigma_{stic} \cdot \frac{(\sum_i E_i^2)^{\frac{1}{2}}}{E_{tot}}, \end{aligned} \tag{6.15}$$

with $E_{tot} = \sum_i E_i$.

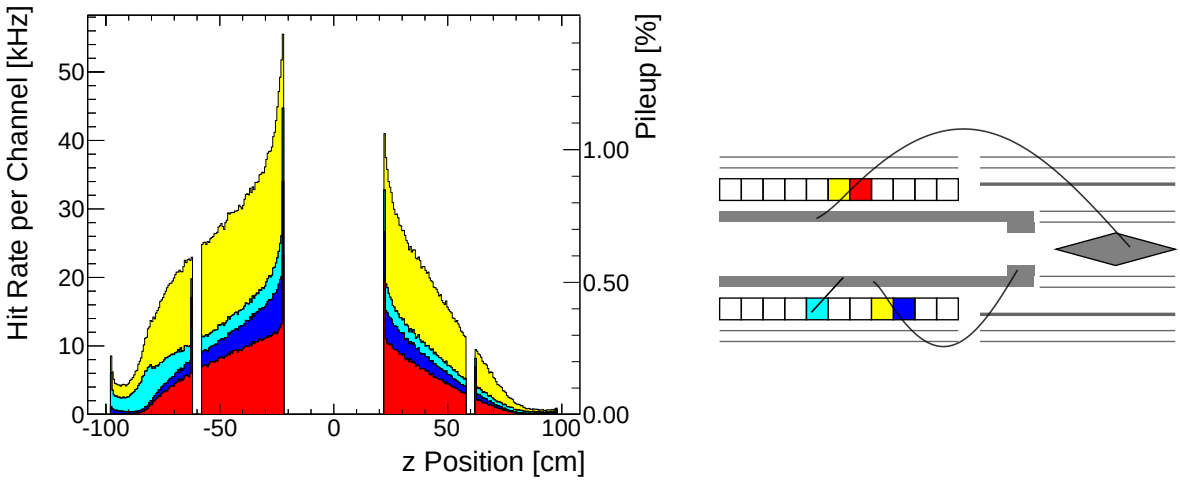

(a) **(b)**

Figure 6.16.: **(a)** Hit rate per channel as a function of the z position of the tile. **(b)** Sketch of the different processes which contribute to the total rate, indicated by different colours. *Red:* particles coming from the target. *Blue / cyan:* particles not originating from the target and impinging the detector from the outside / inside. *Yellow:* hits due to tracks, which traverse multiple tiles.

Hit Rate

Figure 6.16a shows the electron hit rate per channel as a function of the z position for a muon decay rate of 100 MHz. The associated pileup probability P_{pu} is shown on the right axis, assuming an average dead-time of $\Delta t_{dt} = 260\,\text{ns}$. For the planned beam intensity in phase II of 2 GHz, the hit rate is enhanced by a factor of 20. This also increases the pileup probability by roughly a factor 20.
The hit rate distribution is slightly asymmetric. The higher rate in the two upstream detector stations with $-98\,\text{cm} < z < -22\,\text{cm}$ can be explained by the polarisation of the muon beam. In the μ^+ Michel decay, the positron is preferably emitted in direction of the muon spin, which is aligned anti-parallel to its momentum direction. The slight excess in the first re-curl station at $z \approx -98\,\text{cm}$ originates from in-flight decays of muons in front of the detector.
The different colours in Figure 6.16a indicate different processes which contribute to the total rate. These processes are sketched in Figure 6.16b. The rate of electrons which come from muon decays in the target (marked in red) constitutes about 25 % of the total rate. Practically all associated tracks are within the acceptance of the tracking detector and can be fully reconstructed. After passing the scintillator layer, the electrons are stopped in the material on the inside of the scintillator tiles; mainly in the stainless steel beam-pipe. The fraction of electrons which are not stopped and re-enter the Tile Detector is negligible.
Particle tracks which do not originate from the target (marked in blue and cyan) contribute about 10 % to the total rate. This contribution can be split into tracks which hit the Tile Detector from the outside (marked in blue) and tracks which impinge from the inside (marked in cyan). The former are mainly coming from electrons and positrons produced in the detector material and beam collimators via Bhabha scattering or photon conversion. The latter background predominantly comes from photons produced via Bremsstrahlung, which can easily pass through the relatively large material budget inside of the Tile Detector. In the first re-curl station at $-98\,\text{cm} < z < -62\,\text{cm}$, this background is slightly enhanced due to secondary particles produced

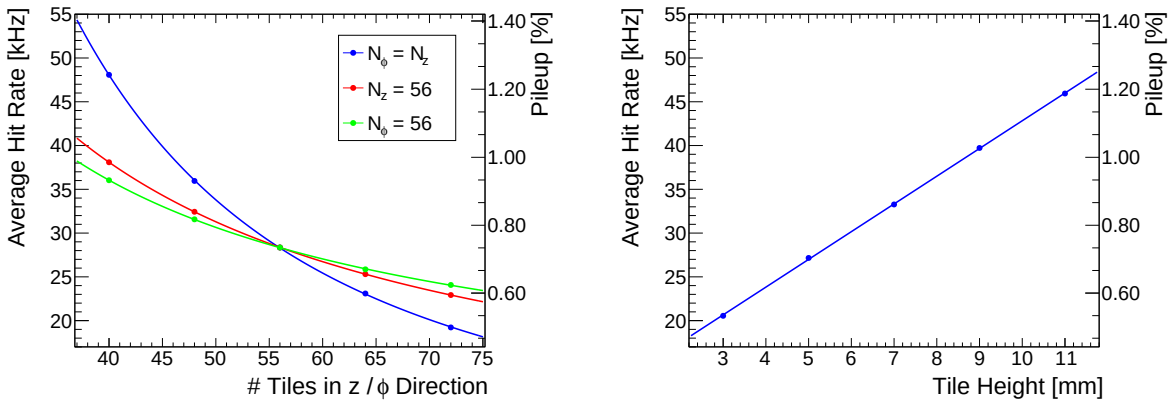

(a) **(b)**

Figure 6.17.: (b) Average channel hit rate in the inner re-curl stations as a function of the number of tiles in ϕ and z direction. **(b)** Mean hit rate as a function of the tile height for $N_z = 60$ and $N_\phi = 56$.

in a beam collimator located at $z = -80\,\text{cm}$.
As discussed above, an electron usually generates a signal in several tiles. This effect (marked in yellow) increases the hit rate by a factor of two, which corresponds to the average size of a hit cluster. In principle it is possible to reduce the cluster size by tilting the tiles according to the average impact angle of the incoming electrons. In this way the occupancy can be reduced by about 15 %. However, this approach is discarded, since the production process for such a tile geometry is significantly more complex.
The maximum hit rate of about $R = 50\,\text{kHz}$ for phase Ib is relatively moderate and can be processed by the current version of the STiC chip. The average pileup probability is below one percent, which is well below the targeted value. The associated signal efficiency is about $\varepsilon \approx \varepsilon_{pu}^3 > 97\,\%$, assuming other contributions to be negligible. For phase II, the hit rate increases by a factor of 20, due to the increased beam intensity. Therefore, the data transmission rate of the chip has to be increased by one order of magnitude, in order to process hit rates of up to $R = 1\,\text{MHz}$. Due to the increased hit rate, the pileup probability in phase II is significantly enhanced. Assuming a channel dead-time of $\Delta t_{dt} = 260\,\text{ns}$, the pileup probability ranges up to 20 % for the innermost tiles. In order to keep the pileup probability in the order of a few percent, the dead-time consequently has to be decreased. This can be achieved with the zero pole cancellation circuit, which is currently being tested in the latest STiC version, or by using the DRS5 waveform digitiser.
Figure 6.17a shows the average channel hit rate and associated pileup probability for the inner re-curl stations as a function of the detector granularity. In first approximation, the hit rate and pileup probability is inversely proportional to the number of tiles: $1/R \propto N_z \cdot N_\phi$. However, also the size of the hit clusters increases with the number of tiles, which determines the lower limit of the hit rate for a high granularity. Since the impact angle $\bar{\vartheta}$ is larger than $\bar{\varphi}$, the effect is more pronounced for N_z compared to N_ϕ. The average cluster size n_c is approximately proportional to the height of the tiles (see Equation 6.14). This relation is reflected in Figure 6.17a, which shows the hit rate dependence on the tile height for $N_z = 60$ and $N_\phi = 56$. The lowest hit rate is thus achieved for thin tiles. Consequently, there is a trade-off between a low hit rate and a high time resolution (compare Figure 6.10b). In the final detector design, a tile height of 5 mm is chosen, which is a reasonable compromise between a high time resolution and low pileup.

7. Mu3e Tile Detector Prototype Measurements

The Tile Detector concept presented in the last section, has been validated in several test-beam measurement campaigns, which are discussed in this chapter. The first section presents two time resolution measurements performed with single tiles, including a measurement with the DRS4 chip and a setup specific to the validation of the tile simulation used in section 6.3.1. In the second section, the measurement of the time resolution and detection efficiency of a 16-channel prototype of a Tile Detector Submodule is presented.

7.1. Single Tile Measurements

The response of a single scintillator-SiPM system has been studied extensively in several measurement campaigns at the DESY[1] test-beam facility. The two main goals were to measure the time resolution of the tile and the validation of the scintillator-SiPM simulation discussed in section 6.3.1. The experimental setup used for these measurements is shown in Figure 7.1.
Two identical BC408 scintillator tiles are placed consecutively in a pulsed 3 GeV electron beam, which is produced by the synchrotron DESY II. As shown in Figure 6.8a, the scintillator response to 3 GeV electrons is expected to be similar to the response to electrons in the energy range of the Mu3e experiment. The beam impacts the tile perpendicular to the tile surface, which corresponds to an angle $\vartheta = \varphi = 0°$, according to the definition in Equation 6.12 and Equation 6.13. The scintillator tiles have a geometry of $7.5 \times 8.5 \times 5.0\,\mathrm{mm}^3$. These tile dimensions correspond to an earlier version of the detector design with $N_z = N_\phi = 48$ tiles arranged in a dodecagon[2] structure, instead of the current tetradecagon[3] geometry with $N_z = 60$ and $N_\phi = 56$. A diamond milling cutter has been used for the machining of the tiles, yielding a high surface quality. The tiles are coated on five sides with reflective TiO_2 paint[4]. The scintillation light is read out with a $3 \times 3\,\mathrm{mm}^2$ MPPC (S10362-33-050C) with a pixel size of 50 µm, which is coupled to the uncoated $7.5 \times 8.5\,\mathrm{mm}^2$ side via optical grease.

7.1.1. Time Resolution Measurement with the DRS4 Chip

As discussed in section 6.2.1, the DRS chip is considered as an alternative to the STiC chip, in particular for phase II. Therefore, the time resolution of the scintillator-SiPM system has been measured using a DRS4 evaluation board[5] for the readout of the SiPM signals. The data has been taken during a measurement campaign in June 2013. The SiPM signals are digitised by the DRS chip with a sampling rate of 5 GSPS, and the recorded waveforms are stored on a hard disk. The timestamp and amplitude of the signals is extracted via an offline analysis of the signal waveforms. The SiPMs have been operated at several bias voltages. The best results,

[1] Deutsches Elektronen-Synchrotron
[2] 12-fold symmetry
[3] 14-fold symmetry
[4] EJ-510
[5] Version 4

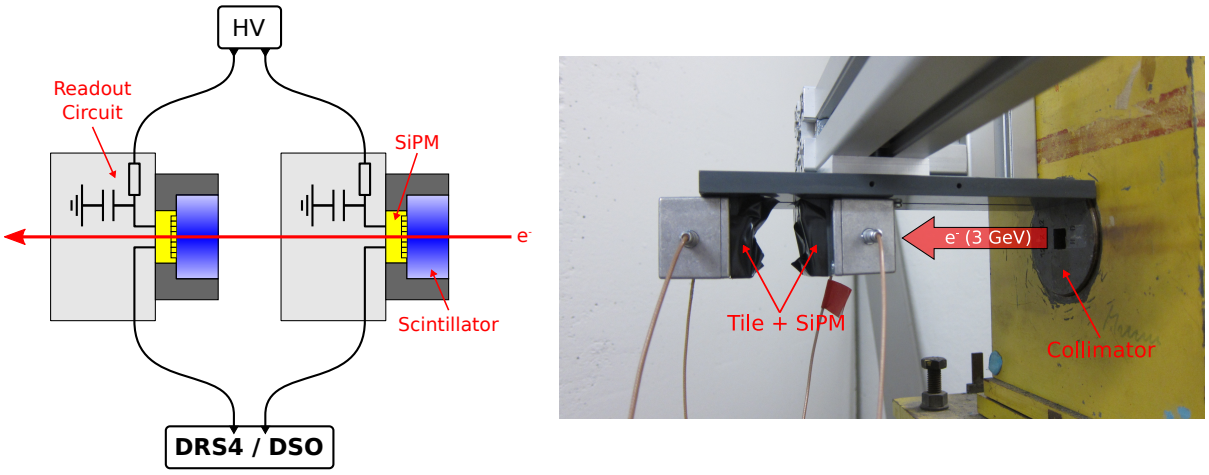

(a) (b)

Figure 7.1.: (a) Schematic sketch and **(b)** picture (October 2013) of the measurement setup at DESY test-beam facility. Two identical tiles are placed consecutively in a 3 GeV electron beam. The SiPMs are read out with a DRS4 chip and a DSO, respectively.

which are presented in the following, have been achieved for an over-voltage of $V_{ov} \approx 2.2\,\mathrm{V}$. The average signal amplitude measured for the two tiles is about $A = 150\,\mathrm{mV}$, corresponding to roughly 500 detected photons. The amplitude spectra for the two tiles can be found in Figure A.9. For the extraction of the signal timestamps, two different methods are compared: the leading edge (LE) discrimination method described in section 4.4 and a constant fraction (CF) discrimination method. In the CF method, the discrimination threshold is set at a certain fraction of the signal amplitude. In first approximation, this eliminates the time-walk effect. In order to increase the precision of the timestamps, both methods use a linear interpolation between adjacent sample points.

The *coincidence time resolution* (CTR) σ_{ctr} of the system is determined via the difference of the timestamps of the two tiles $\delta t = t_1 - t_2$. Figure 7.2a shows the measured distribution of the time differences for LE and CF discrimination. Assuming the response of both scintillator-SiPM systems to be identical, the time resolution of a single tile is given by $\sigma_t = \sigma_{ctr}/\sqrt{2}$.

Figure 7.2b shows the measured time resolution as a function of the discrimination threshold. The best resolution of $\sigma_t = 91\,\mathrm{ps}$ is achieved with constant fraction discrimination and a threshold of 10 %. For higher thresholds, the time resolution slightly degrades, due to a residual time-walk effect. For the LE discrimination, the time-walk effect is not corrected for, which results in a significantly degraded time resolution[1].

For an ideal system, one would theoretically expect to achieve the best resolution for the minimum discrimination threshold, where the sinal has the largest slope and the time-walk effect is negligible. However, the measured resolution significantly degrades for thresholds below 4 mV and 4 %, respectively. Similar to the measurements presented in section 5.3, this is explained by the bandwidth of the system, which reduces the initial slope of the signal.

The average energy deposition in the tile is about $E = 0.95\,\mathrm{MeV}$, which is determined from simulation (see next section). In the Mu3e experiment, the average energy deposition in the Tile Detector is about 50 % larger (see Figure 6.15a), due to the non-zero impact angle of the electrons, which results in a longer path length in the scintillator. This effect yields an improvement in the

[1] Applying a time-walk correction, the LE method yields a similar time resolution as the CF discrimination.

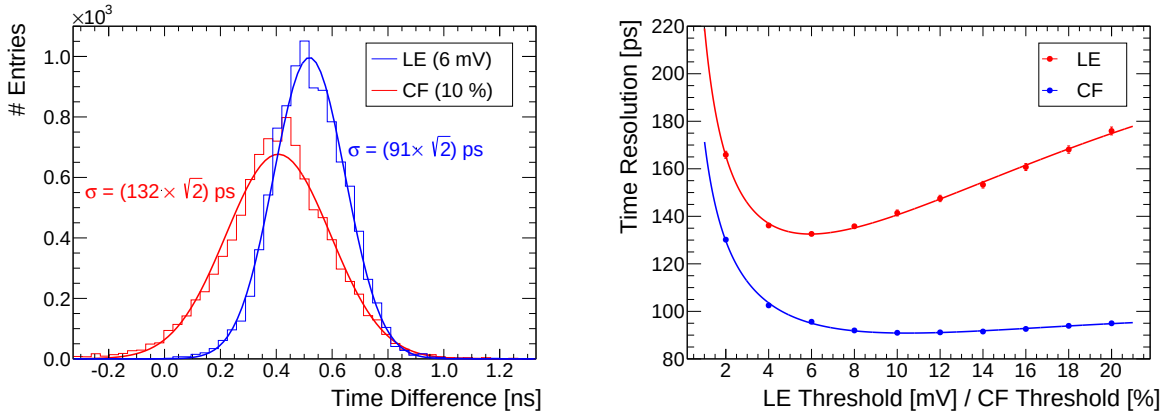

(a) **(b)**

Figure 7.2.: Coincidence time resolution measured with the DRS4 chip for leading edge (LE) and constant fraction (CF) discrimination. The LE data is not corrected for time-walk. **(a)** Distribution of timestamp difference $\delta t = t_1 - t_2$ measured with the two tiles. **(b)** Time resolution $\sigma_t = \sigma_{ctr}/\sqrt{2}$ as a function of the discrimination threshold.

time resolution of about 22 %, assuming the ideal energy dependence described by Equation 6.7. The resulting resolution expected for the conditions in the Mu3e experiment thus is about $\sigma_t = 73\,\text{ps}$. This result shows, that the targeted time resolution can be achieved using the DRS chip. The discrepancy between the achieved time resolution and the simulation results presented in section 6.3.1 are to a large extend explained by the lower bandwidth and a larger vertical noise, compared to the assumptions made in section 6.3.1. In the next section, simulation and measurement results are compared in detail.
In addition to the results discussed above, several other tile geometries and SiPM types have been tested in the particle beam. A detailed discussion of these measurements can be found in [115]. The response dependence on the tile dimensions and SiPM type discussed in section 6.3.1 could thereby be confirmed qualitatively. However, a quantitative interpretation of the results is not possible, due to large systematic uncertainties related to the positioning of the tile in the beam and the coupling procedure of the SiPM to the tile.

7.1.2. Simulation Validation

A main objective of the test-beam measurements was to validate the detector simulation presented in section 6.3.1. In the measurements with the DRS chip discussed above, the used MPPCs exhibit a rather large dark-rate of several MHz. This prohibits a precise determination of the SiPM parameters required for the simulation. Therefore, the validation measurement has been performed in a subsequent measurement campaign in October 2013, using novel MPPC sensors, which show a significantly lower dark-rate.
The measurement setup is similar to the one discussed above, with the exception, that the SiPM signals are recorded using the DSO which is also used in the measurements presented in section 5.3. The signal waveforms are digitised with a sampling rate of 5 GSPS and analysed in the same way as described above. For the measurement of the time resolution, a small full scale range (FSR) of $\Delta V_{FSR} = 40\,\text{mV}$ is used, in order to minimise the influence of the ENOB of the DSO.
The experimental setup is simulated using the framework described in section 6.3.1. The SiPM parameters are determined using the characterisation procedure described in section 5.3.1. The

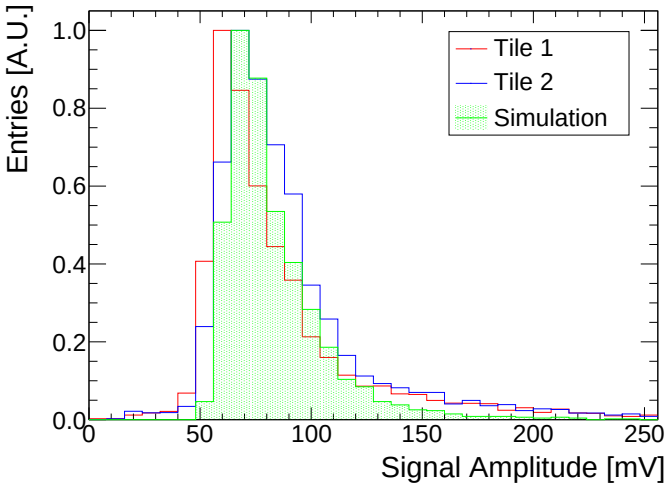

Figure 7.3.: Amplitude spectrum for the test-beam measurement and simulation. The light yield in the simulation is scaled by a factor of 0.7. The difference between Tile 1 and Tile 2 originates from a slightly different SiPM gain. The width of the distribution is underestimated by the simulation, which can possibly be explained by a different incident angle of the electrons or secondary particles in the experimental hall.

obtained parameter values for the simulation input are listed in Table A.3. The bandwidth of the system and the vertical noise of the DSO are modelled in the same way as discussed in section 5.3.

The tile response is studied for two different over-voltages of $V_{ov} = 1.4\,\mathrm{V}$ and $V_{ov} = 1.9\,\mathrm{V}$. Figure 7.3 shows the obtained amplitude spectrum, exemplary for $V_{ov} = 1.4\,\mathrm{V}$. The measured signal amplitude for both over-voltages is about 30 % smaller then the simulated amplitude, assuming a scintillation yield as specified by the manufacturer. A possible explanation for this is the natural aging [116,117] of the utilised scintillator, which is several years old. In addition, the light collection efficiency in the tile might potentially be overestimated in the simulation. This can arise from overestimating the reflectivity of the coating, the surface quality of the scintillator or the quality of the optical coupling to the SiPM. For example, a coating reflectivity of 90 % instead of the nominal value of 95 % would reduce the light yield by about 25 %. In order to obtain comparable simulation results for the time resolution, the scintillator light yield in the simulation is scaled by a factor of $S = 0.7$, in order to match the measured amplitude. Using this adjustment, the simulation reasonably describes the observed amplitude spectrum. However, the measured distribution is slightly wider than expected from simulation. This can possibly be explained by a different distribution of the impact angle of the electrons. Furthermore, the measured amplitude spectrum might be disturbed by secondary particles produced in the beam collimator. The observed difference in the amplitude spectra is taken into account by a 10 % uncertainty in the scaling factor of the scintillation yield: $S = 0.70 \pm 0.07$.

Figure 7.4 shows the time resolution $\sigma_t = \sigma_{ctr}/\sqrt{2}$ obtained with the LE discrimination method for $V_{ov} = 1.4\,\mathrm{V}$ and $V_{ov} = 1.9\,\mathrm{V}$. It can be seen, that the simulation accurately described the measured scintillator-SiPM response for both data sets, which demonstrates the validity of the simulation model. The systematic simulation uncertainty of about $\pm 10\,\%$ is primarily associated with the uncertainty in the cutoff frequency ν_c, vertical noise σ_{en} of the DSO and the scaling factor for the scintillation yield S.

The achieved time resolution is significantly better compared to the LE discrimination measure-

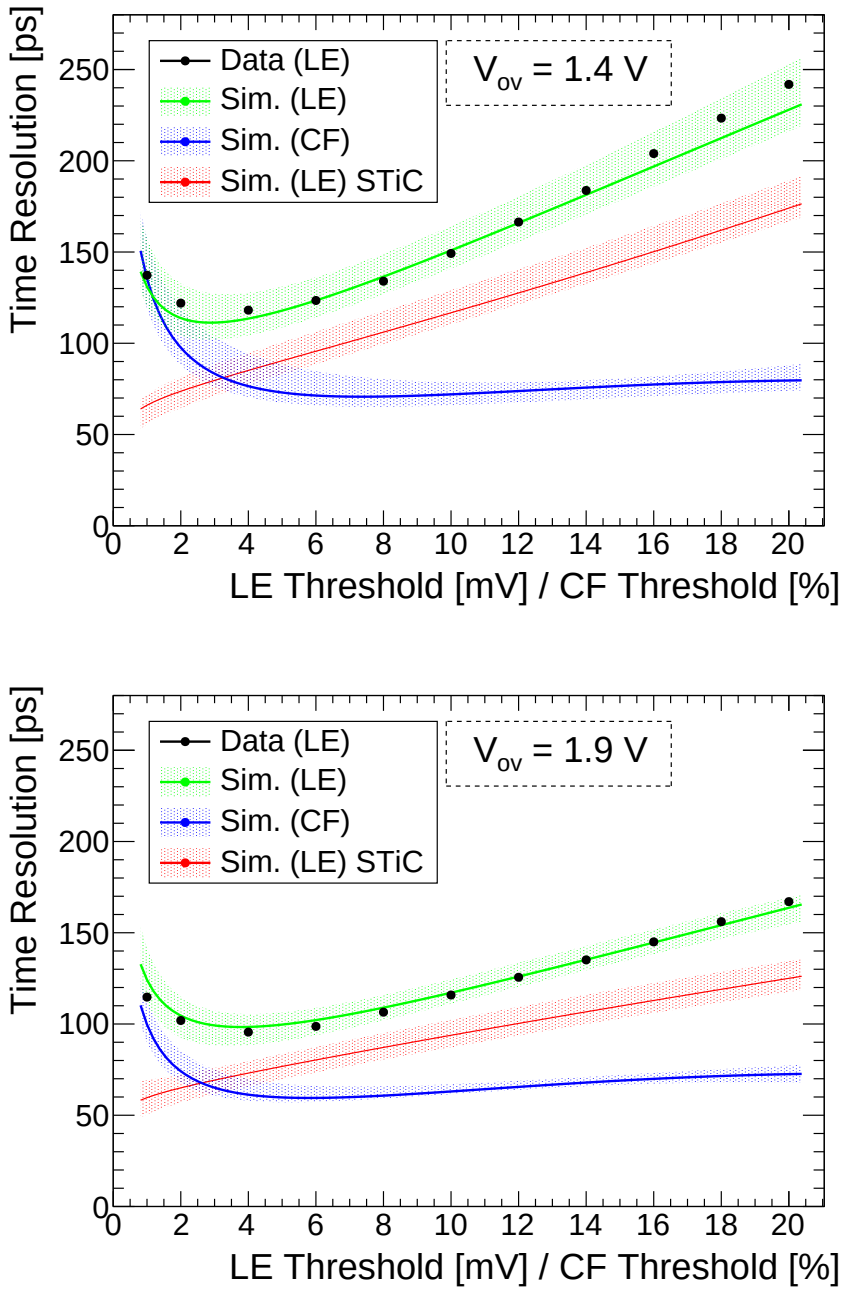

Figure 7.4.: Simulated and measured time resolution of tile for $V_{ov} = 1.4\,\mathrm{V}$ and $V_{ov} = 1.9\,\mathrm{V}$. In the measurement, the time resolution is determined using leading edge (LE) discrimination, without time-walk correction. In addition, the simulated resolution using a constant fraction (CF) method is shown by the blue curve, which, in first approximation, in not effected by time-walk. The simulation data marked in red show the resolution using the parameter values for the electronic noise and bandwidth which are estimated for the STiC readout.

ment with the DRS4 chip. This is primarily explained by the larger vertical noise of the DRS chip. Although the DRS has a much larger number of bits available for the voltage quantisation, the overall vertical resolution is limited by the larger fixed FSR of $\Delta V_{FSR} = 1\,\mathrm{V}$. In addition, the MPPCs used in the measurement with the DRS chip feature a significantly higher dark-rate. This effect is expected to degrade the time resolution by a few percent.
The blue simulation curve in Figure 7.4 shows the time resolution obtained with CF discrimination. Here, a comparison to data is not possible, since the signal amplitudes, which are required to determine the threshold, exceed the measurement range of $\Delta V_{FSR} = 40\,\mathrm{mV}$. The simulated resolution can therefore only be qualitatively compared to the data presented in Figure 7.2b, obtained with the DRS chip. Both, the measured threshold dependence of the resolution and the improvement with respect to the LE timing is consistent with the simulation results.
The time resolution of about $\sigma_t \approx 100\,\mathrm{ps}$ obtained in the test-beam measurement significantly differs from the simulation results presented in section 6.3.1. This is explained by the differences in the two setups. One of the major parameters influencing the resolution in the test-beam setup is the limited bandwidth ($\nu_c = 250\,\mathrm{MHz}$) and large vertical noise ($\sigma_{en} = 0.45\,\mathrm{mV} \approx 1.5\,\mathrm{pe}$) related to the ENOB of the DSO. In contrast, the simulation in section 6.3.1 assumes the bandwidth and electronic noise estimated for the STiC readout. The simulation result for the corresponding values of $\nu_c = (500 \pm 100)\,\mathrm{MHz}$ and $\sigma_{en} = (0.50 \pm 0.25)\,\mathrm{pe}$ is shown by the red curve in Figure 7.4. Especially for low thresholds, the higher bandwidth and lower noise significantly improve the time resolution. Assuming a threshold of 3 pe, which corresponds to about 1 mV, the simulation yields a resolution of about $\sigma_t \approx 60\,\mathrm{ps}$. Another important factor is the reduced light yield which has been observed in the test-beam measurement. Following Equation 6.7, this effect is expected to degrade the resolution by about 20 %. Furthermore, in the simulation in section 6.3.1, the tile surface which faces the SiPM is coated, except for a $3.5 \times 3.5\,\mathrm{mm}^2$ window at the SiPM interface. In the test-beam measurement, this surface is completely uncoated. The simulation shows, that this significantly reduces the light yield by a factor of roughly 0.6, strongly depending on the assumed reflectivity of the coating. Another factor degrading the time resolution is the larger tile dimensions of $7.5 \times 8.5 \times 5.0\,\mathrm{mm}^3$, compared to the $6.0 \times 6.5 \times 5.0\,\mathrm{mm}^3$ in the final designed of the Tile Detector. As shown in Figure 6.10a, this degrades the resolution by about 15 %. In addition, the scintillator material (BC418) studied in the simulation is expected to yield a slightly better time resolution compared to the scintillator material (BC408) used in the test-beam measurement (see Figure 6.9b).

7.2. 16-Channel Prototype

This section presents a 16-channel prototype of a Tile Detector Submodule utilising the STiC2 readout chip. The time resolution and detection efficiency ε_d of this prototype has been measured in the electron beam at the DESY test-beam facility. A picture of the setup is shown in Figure 7.5c.
The prototype consists out of an array of 4×4 scintillator tiles (BC408), which is shown in Figure 7.5a. Similar to the single tile measurements described above, each tile has a size of $7.5 \times 8.5 \times 5.0\,\mathrm{mm}^3$, corresponding to the earlier design of the detector with a dodecagon structure. The production and coating of the tiles is done in the same way as described in section 7.1. The tiles in the first and last row are bevelled by 15°, which would allow to arrange twelve modules in a circle. The tile array is orientated parallel to the beam, such that the incident particles traverse four tiles in a row. According to the definition in Equation 6.12, this corresponds to an incident angle of $\varphi = 0°$ and $\vartheta = 90°$.
Similar to the measurements in section 7.1, the scintillation light is read out by $3 \times 3\,\mathrm{mm}^2$ MPPCs[1] with a pixel size of 50 µm, which are coupled to the scintillator via optical grease. Figure 7.5b shows the MPPCs attached to the tiles. The MPPCs are connected to a STiC2 readout chip via a flex-rigid circuit board (see Figure 7.5c), similar to the final connection scheme described in section 6.2.
The electronic noise at the analogue input of the chip is estimated to be roughly at the 0.5 pe level, which is significantly lower than the vertical noise of the DRS chip for high frequencies. Furthermore, the bandwidth of the STiC chip setup is estimated to be significantly higher than in the setup used in section 7.1, which is achieved by the short signal lines and high speed connectors between the SiPMs and the STiC chip.
The functionality of the STiC2 chip is sketched in Figure 7.6. The analogue input signal is duplicated and each copy is processed by a fast discriminator with a tunable threshold. The lower threshold (timing threshold) is used to determine the timestamp of the input signal via leading edge discrimination. This threshold can be varied in a range equivalent to roughly 1 pe to 10 pe. The higher threshold (energy threshold) is used to measure the signal charge, which is proportional to the deposited energy, via the Time-over-Threshold (ToT) of the signal. The chip is designed in such a way that the ToT is in first approximation proportional to the signal charge. A hysteresis in the thresholds suppresses subsequent noise triggering.
The output signals of the two discriminators are combined via a XOR logic. The first rising edge of the resulting XOR signal contains the timing information, and the time interval between the first and the second rising edge contains the energy information. The time of the two rising edges are digitised via an integrated TDC, which is based on a coarse counter (CC) with a 622 MHz reference clock. In the following, the coarse counter values for the time and energy timestamp are referred to as T_{CC} and E_{CC}.
The energy value of an event is given by $E[\mathrm{CC\,Bins}] = E_{CC} - T_{CC}$. For the time information, an additional fine counter (FC) is used, which subdivides the coarse counter period in 32 bins with an average width of 50 ps. The timestamp of an event is thus given by $t[\mathrm{ps}] = (32 \cdot T_{CC} + T_{FC}) \cdot 50\,\mathrm{ps}$, where T_{FC} denotes the fine counter value.
The STiC chip setting, e.g. the individual thresholds, hysteresis and TDC parameters, have been tuned manually. The complete chip configuration is listed in Table A.4. Due to the large amount of parameters, a systematic optimisation of the chip settings could no be carried out. It is expected, that with fully optimised chip settings, the performance can be further enhanced.

[1] S10362-33-050C

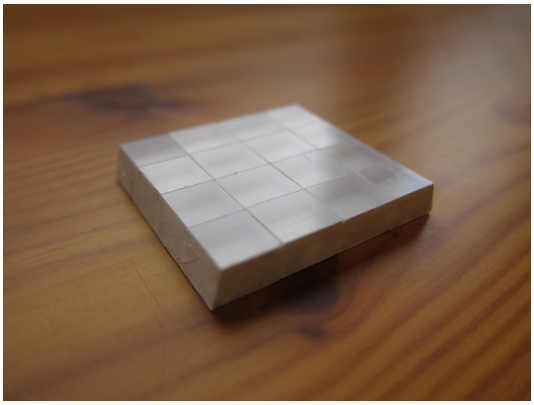

(a)

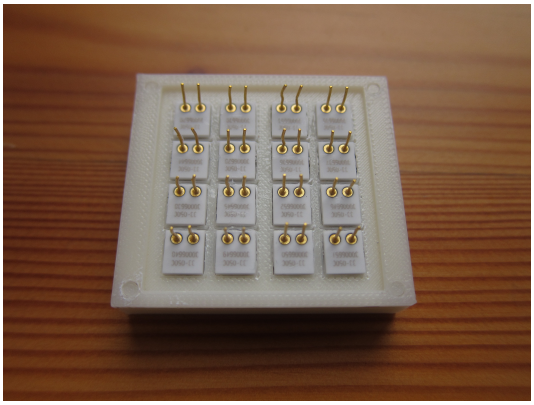

(b)

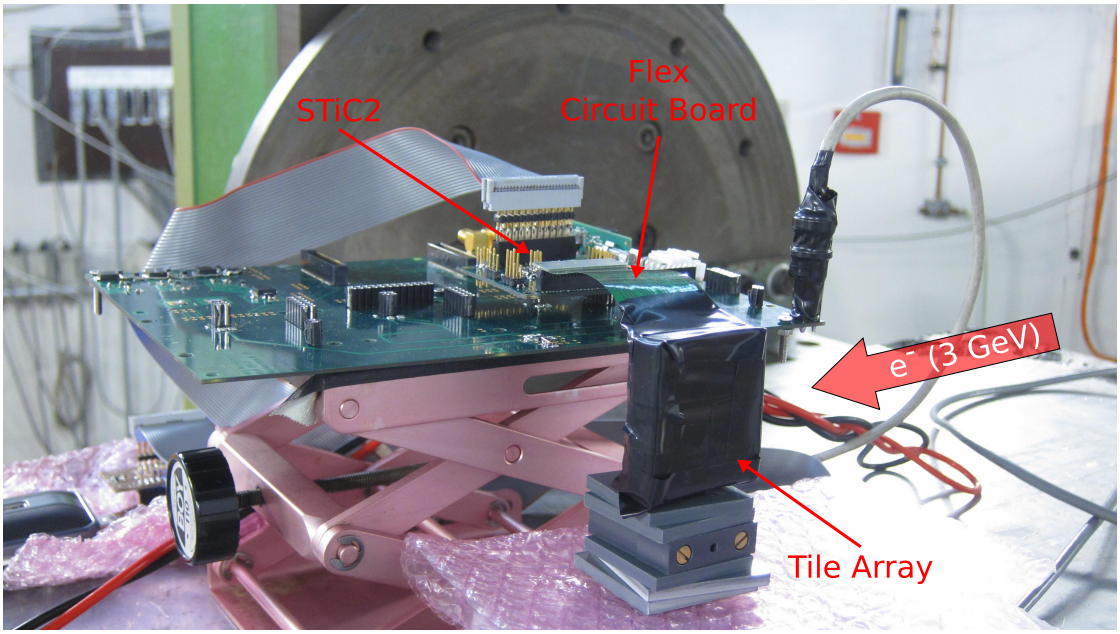

(c)

Figure 7.5.: Prototype of a 16 channel tile detector module. **(a)** 4×4 scintillator tile array. **(b)** MPPCs attached to the tiles via optical grease. **(c)** Test-beam setup of the prototype. The sensor array is connected to a STiC readout chip via a flex circuit board. The tile array is orientated parallel to the beam, such that the electron beam traverses four tiles in a row.

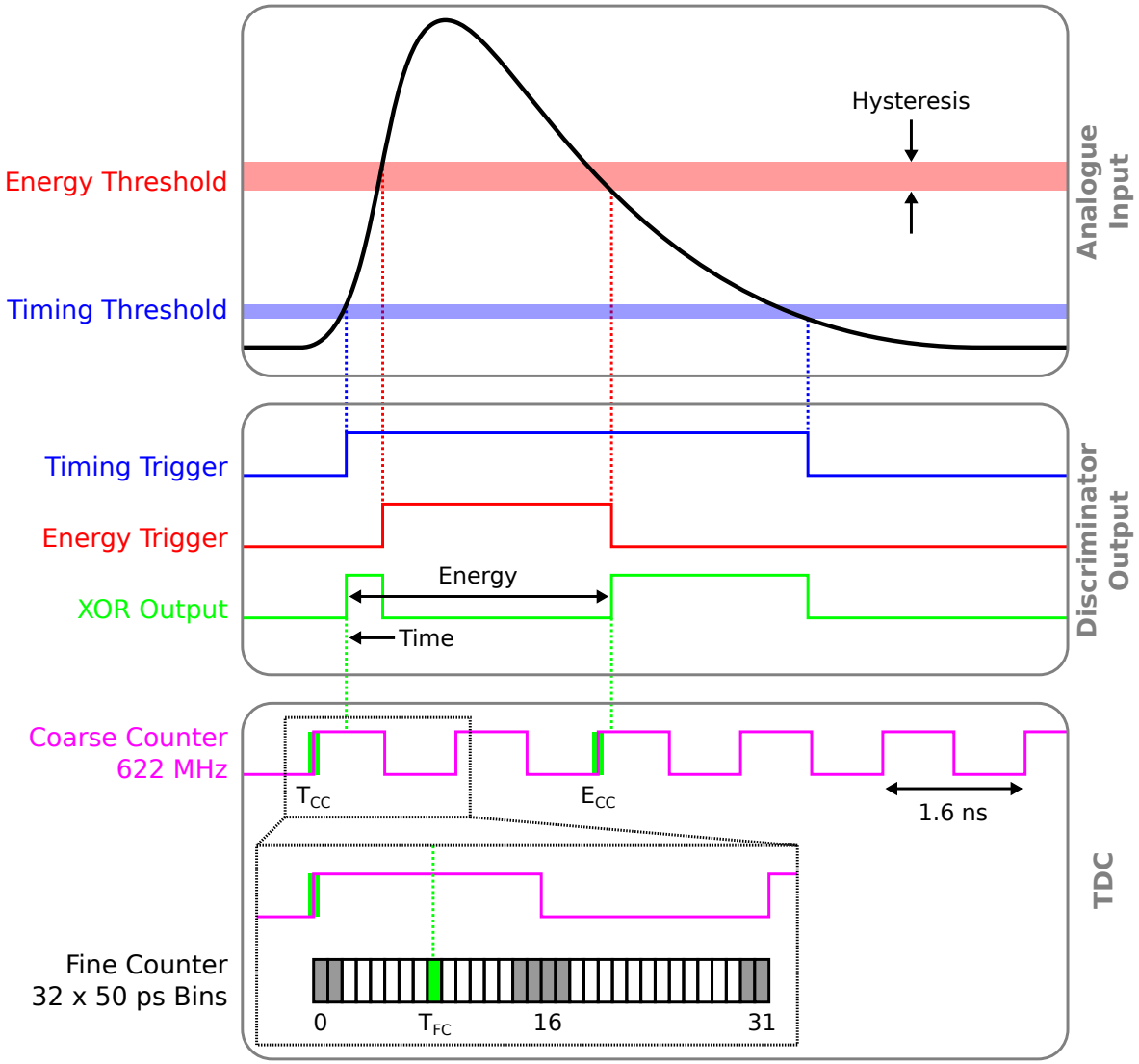

Figure 7.6.: Sketch of the functionality of the STiC2 chip. The time and energy information of the analogue input signal is obtained via two discriminator units. The discriminator output is processed by a TDC with a 622 MHz coarse counter and a fine counter with a bin size of $\Delta T_{FC} = 50$ ps. An accidental feature of STiC2 is that the fine counter information cannot be retrieved for certain FC bins (marked in grey); this deficiency is remedied in the new version of the chip STiC3.

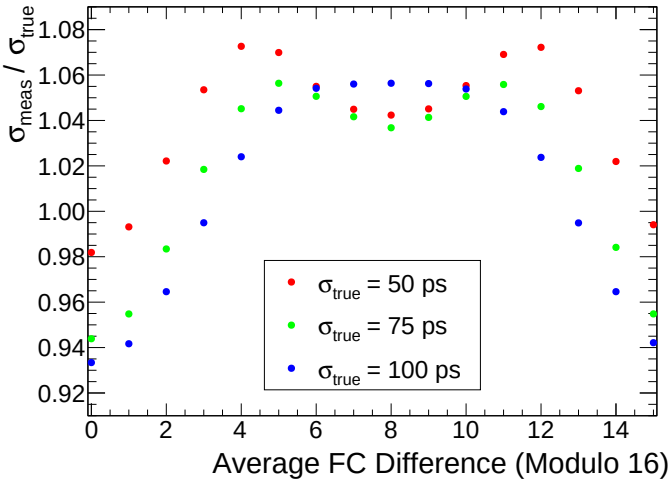

Figure 7.7.: Impact of the faulty fine counter reconstruction on the measured time resolution, assuming all FC bins to have the same size. Depending on the average fine counter difference and true time resolution, this effect can influence the measured resolution by up to ±7 %.

7.2.1. Data Quality

Fine Counter Reconstruction

An unexpected feature of the STiC2 chip is that the fine counter information cannot be properly retrieved. More precisely, it is ambiguous if the timestamp lies within the first 16 FC bins (bin n) or within the second 16 bins (bin $n+16$). This information can in principle be recovered from the state of the coarse counter: if the CC state is '1', the timestamp lies within the first 16 bins and if the CC state is '0', the timestamp lies within the second 16 bins[1] (compare Figure 7.6). However, this method is not reliable for the FC bins close to the transition edges of the coarse counter. Therefore, events in the lower bins 0, 1, 14, 15 and the corresponding higher bins 16, 17, 30, 31 cannot be reconstructed. This is indicated by the grey shading in Figure 7.6. The FC value hence can only be retrieved for about 75 % of the events. In the new chip version STiC3, this inefficiency is remedied.
A consequence of the defective FC reconstruction is that the probability to measure certain time differences is reduced. For example, two hits with a FC difference of $\Delta T_{FC} = 0$ can be reconstructed with a probability of 75 %, whereas a FC difference of $\Delta T_{FC} = 4$ can only be reconstructed in 50 % of the cases. This effect can disturb the measured distribution of time differences δt. Figure 7.7 shows the impact on the time resolution as a function of the average fine counter difference, assuming all FC bins to have the same size of 50 ps[2]. It can be seen, that, depending on the true time resolution, this effect can bias the measured resolution by about ±7 %. In the time resolution measurement presented in section 7.2.3, this effect is corrected for.
Another consequence of the faulty FC reconstruction in STiC2 is that the differential nonlinearity (DNL) of the TDC cannot be determined. The DNL describes the variation in the width of the different FC bins, which can be in the order of several picoseconds. Measurements performed with STiC3 show, that the DNL correction can improve the time resolution by 10 % to 30 %, depending on the average FC difference [118].

[1] It should be noted, that this is a very simplified and abstract description of the actual working principle.
[2] The exact size of the individual bins cannot be measured, due to the faulty fine counter reconstruction.

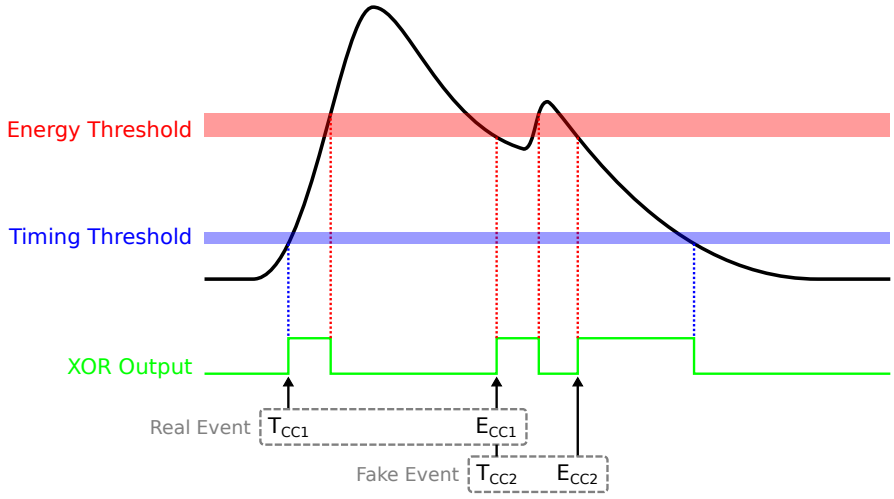

Figure 7.8.: Fake events generated by a second crossing of the energy threshold. This can either be triggered by a secondary scintillation signal or noise. A fake event is identified by the T_{CC} value being identical to the E_{CC} value of the preceding event. The contamination by fake events is about 1.0 %.

Fake Events

The recorded data set comprises a small fraction of fake events, which are generated by a second crossing of the energy threshold, either due to a secondary scintillation signal or due to noise. This effect is sketched in Figure 7.8. The fake events are characterised by the T_{CC} value being identical to the E_{CC} value of the preceeding event. These events are excluded from the data analysis. The contamination by fake events is about 1.0 %.

Hit Distribution

Figure 7.9a shows the number of recorded hits for the 16 tiles, as well as the numbering scheme which is used for the different channels. Only hits with an energy larger than $ToT > 50$ CC Bins are shown, in order to reject cross-talk events, which are discussed in the next paragraph. The beam is centered around the second row of tiles, which shows the highest hit rate, and traverses from the left to the right. The channels 4,11 and 12 are not working due to faulty electrical connections. This problem can easily be solved in future prototypes by a more carefull assembly of the circuit board.

Energy Spectrum

Figure 7.9b shows a typical ToT spectrum, exemplary for channel 2. The ToT spectra of all channels can be found in Figure A.10. The spectrum shows several distinct features. The most prominent feature is the peak at around $ToT = 130$ CC Bins, in the following referred to as *Landau peak*. This peak originates from electrons which fully traverse the tile. Such events can be selected by requiring the neighbouring tiles in the row (channel 1&3) to also have a signal in the Landau peak. The energy spectrum with this selection is shown by the blue curve in Figure 7.9b. The shape of the peak is given by a convolution of a Landau distribution, describing the energy deposition in the tile, and a Gaussian distribution, describing the energy resolution of the detector.
The second peak at $ToT \approx 30$ CC Bins originates from cross-talk between neighbouring scintillator tiles. This can be shown by selecting hits where at least one direct neighbour in the

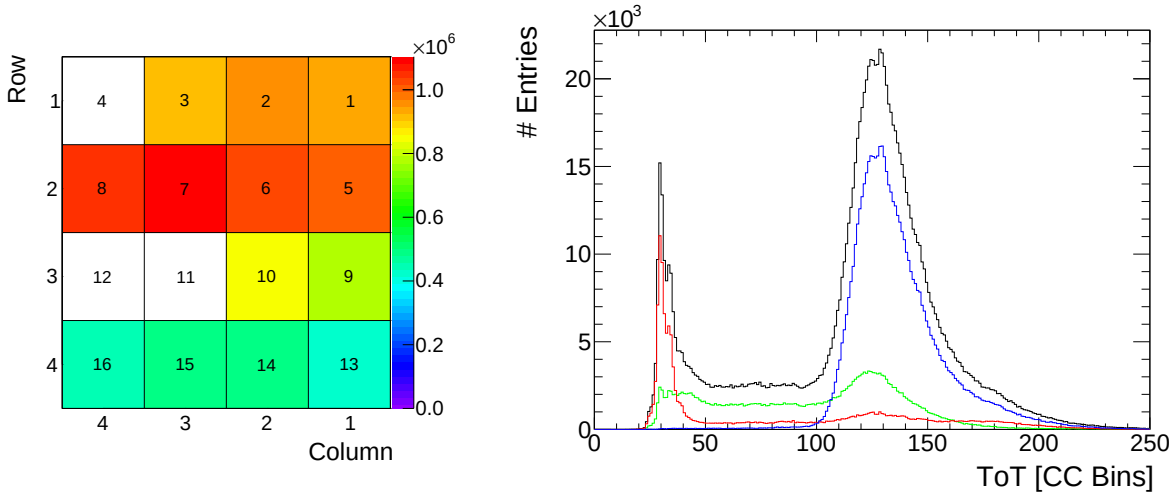

(a) **(b)**

Figure 7.9.: (a) Number of hits in the tiles. The beam traverses the tile array from the right to the left and is centered around the second tile row. The channels 4,11 and 12 are not working due to bad electrical connections. **(b)** Energy deposition in a scintillator tile. The spectrum is composed of the Landau peak (blue), a plateau arising from edge effects (green) and a peak from optical cross-talk (red).

rows above or below the tile (channel 5,6,7) has a large signal with an energy deposition in the Landau peak. The corresponding events are shown by the red curve in Figure 7.9b. There is no correlation between these signals and the positioning of the corresponding signal lines, which excludes electrical cross-talk via capacitive coupling as a possible origin. Therefore, this effect is attributed to optical cross-talk, which can be explained by the fact that the tile surface facing the SiPM is not painted, allowing the scintillation light to diffuse to the neighbouring tile. This can easily be prevented in future prototypes by coating the tile surface around the SiPM.
The plateau region to the left of Landau peak is attributed to edge effects, where the electron enters or exits the tile at the side, indicating that the detector array is not perfectly aligned with the beam. These events can be roughly selected by requiring at least one of the neighbouring tiles in the row to have no signal. In addition, it is required, that no tiles in the neighbouring rows are active, in order to suppress optical cross-talk events. The corresponding energy spectrum of these events is shown by the green curve in Figure 7.9b.

7.2.2. Detection Efficiency

The detection efficiency is determined using particles which traverse all four tiles of a certain row. Such events are selected by requiring at least three hits in the row, with one hit in the first and last tile. The energy deposition of all three hits has to be in the Landau peak. The time difference between the hits is required to be within $\delta t = \pm 200\,\text{ps}$, in order to suppress random coincidences. This implies, that the fine counter value of all three hits can be recovered. In addition, all events are excluded, where one or more additional channels outside of the row are active. These selection criteria assure, that the three hits originate from a single particle straightly traversing all four tiles in the row. The detection efficiency ε_d is then given by the probability to detect a hit in the remaining channel of the row with an energy deposition above the cross-talk level[1]. Furthermore, the T_{CC} value of this hit is required to be within ± 1 of the

[1] $ToT > 50\,\text{CC Bins}$

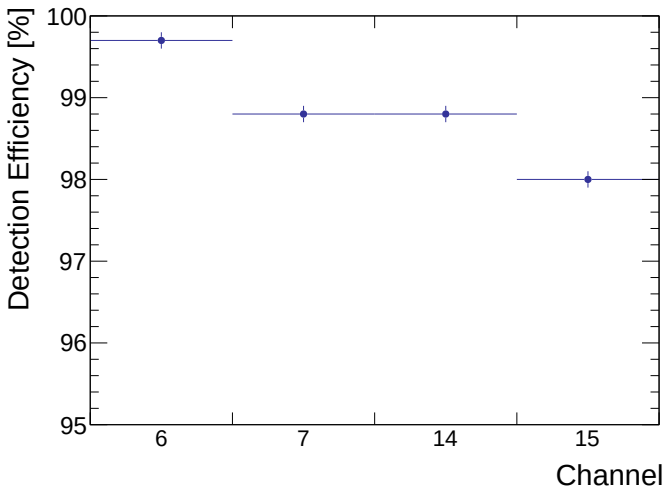

Figure 7.10.: Efficiency measured for channel 6, 7, 14 and 15. The efficiencies for the channels 2, 3 and 10 cannot be determined due to the defective channels 4, 11 and 12. The inefficiencies of up to 2 % can presumably be attributed to the STiC2 chip.

value for the other hits. The fine counter information is not used, since this would reduce the efficiency by roughly 75 %, due to the defective retrieval of the FC value.
Due to the large light yield, which guarantees the signal to be well above the detection threshold, the efficiency is expected to be $\varepsilon_d \approx 100\,\%$. In the measurement, an efficiency of up to $\varepsilon_d = 99.7\,\%$ is achieved for channel 6, which is shown in Figure 7.10. The inefficiencies of up to 2 % observed for channel 7, 14 and 15 can presumably be attributed to the STiC2 chip and might originate from non-optimal chip settings or inefficiencies related to the faulty FC reconstruction. For the chip version STiC3 it has been shown, that in principle an efficiency of $\varepsilon_d = 100\,\%$ can be achieved [118].

7.2.3. Time Resolution

The coincidence time resolution is measured for different pairs of tiles within one row. The signal in both channels is required to be in the Landau peak, in order to assure that the particle fully traverses both tiles. Only events are selected where the fine counter information can be recovered for both hits.
Figure 7.11a shows a measured distribution of the timestamp difference δt, exemplary for channel 5 and 8. The width of the distribution is $\sigma_{\delta t} = 96\,\text{ps}$. Taking into account the correction factor related to the FC reconstruction inefficiency (see Figure 7.7), the obtained coincidence time resolution is $\sigma_{ctr} = 100\,\text{ps}$. Assuming the response of both channels is identical, the time resolution of a single tile is given by: $\sigma_t = 100\,\text{ps}/\sqrt{2} \approx 70\,\text{ps}$. The time resolution is improved by a applying a two dimensional time-walk correction. The correction factor is determined from the energy dependence of the measured time difference $\delta t(E_1, E_2) = t_1(E_1) - t_2(E_2)$, exemplary shown in Figure 7.11b. This distribution is fitted with a two dimensional linear function:

$$F_{tw}(E_1, E_2) = a \cdot E_1 + b \cdot E_2 + c, \tag{7.1}$$

with the free parameters a, b, c. This most basic function yields a good approximation for the measured distribution. The corrected value for a certain time difference δt is given by:

$$\delta t_c = \delta t - F_{tw}(E_1, E_2). \tag{7.2}$$

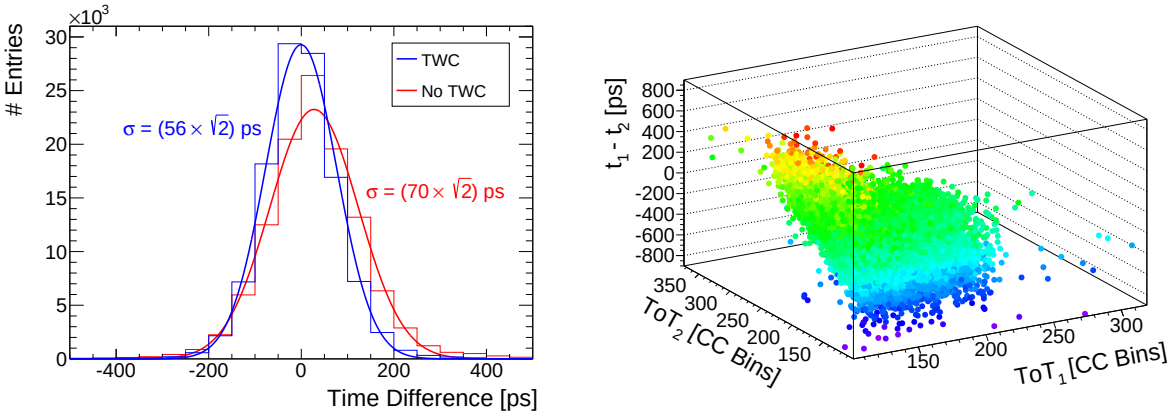

(a) **(b)**

Figure 7.11.: a) Time distribution with and without time-walk correction (TWC). Taking into account the correction factor for the faulty FC reconstruction, the obtained time resolution is $\sigma_t = 70\,\text{ps}$. After applying a time-walk correction, an improved resolution of $\sigma_t = 56\,\text{ps}$ is achieved. **b)** Measured time difference for a channel pair as a function of the deposited energy. A fit to this distribution is used for the time-walk correction.

For the time-walk correction, the data set is divided into two independent subsets. One subset is used to obtain the correction function F_{tw} and the other subset is used to determine the time resolution applying the correction in Equation 7.2. The distributions of the corrected time difference is shown by the blue curve in Figure 7.11a. Depending on the channel combination, the time-walk correction yields an improvement between 13 % and 23 %, which is consistent with simulation results.
Figure 7.12 shows the time resolution with time-walk correction measured for various combinations of channel pairs, including directly neighbouring tiles (bin 1 to 9) and pairs with one (bin 10 to 14) and two (bin 15 & 16) tiles in between. The average time resolution over all combinations is $\bar{\sigma}_t = 66\,\text{ps}$; the best achieved resolution is $\sigma_t = 56\,\text{ps}$. The channel-to-channel variations can be explained by different chip settings and variations in the SiPM over voltage. In addition, the quality of the optical coupling between the scintillator and the SiPM is expected to vary for the different channels, due to a non-optimal assembly procedure. For future prototypes, the stability of the coupling between the scintillator and the SiPM can be improved by using optical cement instead of silicon grease.

Simulation Results

The measurement of the time resolution has been simulated with the framework described in section 7.1.2. The simulation results should be interpreted as a rough estimate, since the response characteristics of the used setup (including the STiC2 chip and connection boards) in terms of noise and frequency response are not precisely known. Furthermore, the over-voltage of the individual SiPMs, which is influenced by the STiC settings, could not be determined during the measurement. Therefore, the SiPM parameters are approximated using the values obtained for the measurement in section 5.3 (see Table 5.2). For the modelling of the bandwidth, a cutoff frequency of $\nu = (500 \pm 100)\,\text{MHz}$ is assumed, which is the design value for the STiC chip. The bandwidth limitation arising from the connectors and traces on the circuit boards is assumed to be negligible. The electronic noise at the analogue input of the STiC chip is assumed to be $\sigma_{en} = (0.5 \pm 2.5)\,\text{pe}$, and the timing threshold is estimated to be roughly $(3 \pm 2)\,\text{pe}$.

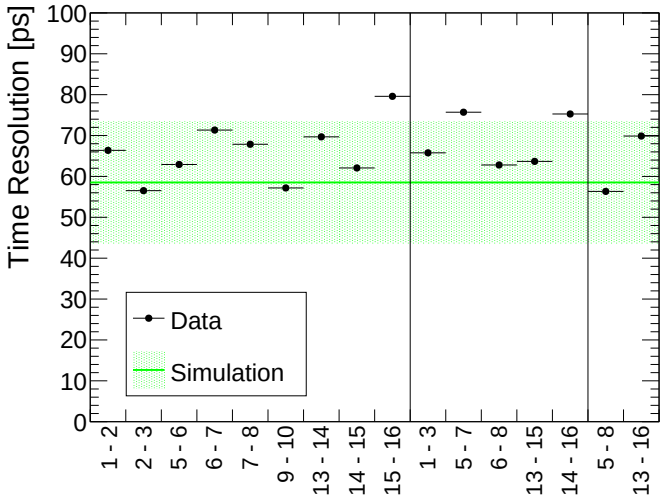

Figure 7.12.: Time resolution including time-walk correction, measured for directly neighbouring channel pairs (bin 1 to 9) and pairs with one (bin 10 to 14) and two (bin 15 & 16) tiles in between. The measurement results are in good agreement with simulation.

The simulated timestamps are randomised according to a Gaussian distribution, in order to take into account the intrinsic jitter of the STiC chip, which is assumed to be $\sigma_{stic} = 30\,\text{ps}$. A time-walk correction is applied to the simulated data in exactly the same way as for the measured data. The time resolution obtained with this simulation setup is $\sigma_t^{sim} = (58 \pm 15)\,\text{ps}$, which is shown by the green curve in Figure 7.12. Within the uncertainties, which arise from the imprecise input parameter, the simulated resolution is consistent with the measurement. This reassure the validity of the simulation results discussed in section 6.3.1.
The average energy deposition in the simulation is about $E = 1.4\,\text{MeV}$, which is similar to the average energy deposition in the Tile Detector (see Figure 6.15a). Therefore, the measured time resolution yields a good approximation for the achievable performance in the Mu3e experiment. The time resolution achieved with the detector prototype is well below the targeted value of $\sigma_t = 85\,\text{ps}$, which demonstrates the feasibility of the detector concept. According to the simulation results, the performance in the final detector is expected to further improve due to a newer and faster scintillator (BC418), better optical coupling, a smaller tile geometry of $6.5 \times 6.0 \times 5.0\,\text{mm}^3$, as well as the improvements in the new STiC3 chip.

8. Summary

The Mu3e experiment is proposed to search for the lepton flavour violating decay $\mu^+ \to e^+e^+e^-$. In the Standard Model of particle physics, this decay is extremely suppressed with a branching ratio of $BR \approx 10^{-54}$. However, many theories beyond the Standard Model predict a significantly enhanced decay rate within an experimentally accessible range. The goal of the Mu3e experiment is to reach a sensitivity to the $\mu^+ \to e^+e^+e^-$ branching ratio of $BR = 10^{-16}$, which exceeds the current exclusion limit for this process by four orders of magnitude. An observation of this decay would be a clear sign for New Physics; a non-observation on the other hand would strongly restrict the parameter space of many theories beyond the Standard Model.
Achieving the targeted sensitivity requires a high precision detector with an excellent momentum, vertex and time resolution, in order to suppress background processes to a level of below 10^{-16} per muon decay. The precise timing information of the muon decay products will be provided by the *Tile Detector*, which is a highly granular sub-detector system based on scintillator tiles and Silicon Photomultipliers (SiPMs) for the readout of the scintillation light. The design goal for this detector system is to achieve a single hit time resolution better than $\sigma_t = 85\,\text{ps}$ and a signal efficiency of $\varepsilon > 80\,\%$.
This thesis describes the development of the Tile Detector concept and demonstrates the feasibility of the elaborated design. In this context, a comprehensive simulation framework has been developed, in order to optimise the detector design and estimate the performance in terms of time resolution and signal efficiency. The central component of this framework is a detailed simulation of the SiPM response, which has been validated in several measurements using fast laser pulses. The measured charge and timing response of the SiPM is accurately modelled by the simulation within an uncertainty of a few percent. The SiPM simulation was combined with a simulation of a scintillator tile implemented in Geant4, which was used to optimise the detector in terms of scintillator material, tile dimensions and SiPM type. This scintillator-SiPM simulation model was verified in a measurement of the tile response to 3 GeV electrons. The measured timing behaviour of the tile is well described by the simulation with an accuracy of at least 10 %.
Based on the optimisations studies, the technical design of the Tile Detector has been devised. The final detector will be subdivided into four identical segments, each consisting out of 3360 scintillator tiles with a size of $6.5 \times 6.0 \times 5.0\,\text{mm}^3$. The high granularity results in a low occupancy and a high time resolution. The individual tiles are made out of BC418 scintillator, which features the best time resolution amongst the studied tile materials. The scintillation light is detected by $3 \times 3\,\text{mm}^2$ SiPMs with a pixel size of 50 µm (MPPC S12572-050P). This sensor type provides a high time resolution and features a reasonably fast signal shape, which results in a moderate channel dead-time. The SiPMs are read out by a custom ASIC chip (STiC), which is designed for fast timing applications. The time resolution obtained in the simulation of this detector setup is about $\sigma_t = 42\,\text{ps}$, which surpasses the design goal for the Tile Detector.
A 16-channel prototype of a detector module was constructed, which utilises a prototype version of the STiC readout chip (STiC2). The detector prototype was successfully operated in a 3 GeV electron beam at the DESY test-beam facility. In the test-beam measurements, a time resolution of up to $\sigma_t = 56\,\text{ps}$ was achieved, which by far exceeds the requirements of the Mu3e experiment.

The discrepancy between the measured resolution and the simulation results is explained by the larger tile geometry, inferior scintillator material and sub-optimal coating of the tile. Taking these effects into account, the simulation is consistent with the measured resolution.
The developed Tile Detector design has been implemented in a Geant4 simulation of the Mu3e experiment, which was used to study the response characteristics of the detector for the running conditions in the final experiment. For a muon decay rate of 100 MHz, corresponding to the first phase of the experiment, a maximum hit rate per tile of about 50 kHz and a pileup probability below 1 % is obtained, which is well within the design specifications. The overall signal efficiency obtained in the simulation studies is $\varepsilon \approx 97\,\%$.
The simulation studies, as well as the measurements with the detector prototype demonstrate the feasibility of the developed detector concept and show that the required performance can be achieved. This concludes an essential part of the research and development activities for the Tile Detector.

A. Supplementary Material

Table A.1.: Properties of commonly used anorganic scintillator materials.

Scintillator	ρ [g/cm^2]	X_0 [cm]	τ_d [ns]	LightYield [phot./MeV]	λ_{peak} [nm]
NaI:Ti	3.67	2.59	230	38000	415
CsI	4.51	1.85	30	2000	315
CsI:Ti	4.51	1.85	1000	55000	550
BaF_2[1]	4.88	2.10	0.7/630	2500/6500	220/310
BGO[2]	7.13	1.12	300	8000	480
PWO[3]	8.28	0.85	10-30	70-200	430
LSO[4]	7.41	1.20	12-40	26000	420
$LaBr_3$:Ce	5.29	-	18	70000	356
LuAG:Ce	6.73	-	60	25000	535
LFS	7.35	1.15	35	32000	425

[1] Values for fast and slow signal component.
[2] $Bi_4Ge_3O_12$
[3] $PbWO_4$
[4] Lu_2SiO_5 : Ce

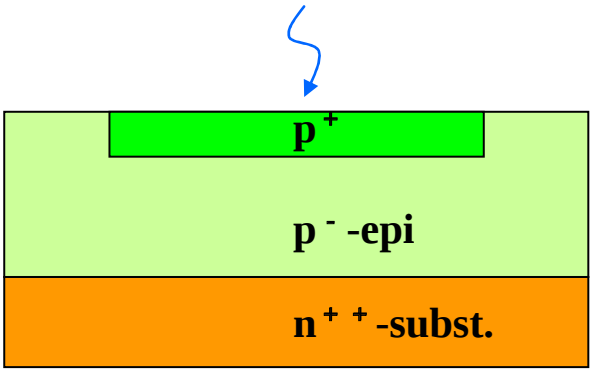

Figure A.1.: HPK reverse structure of a MPPC [119].

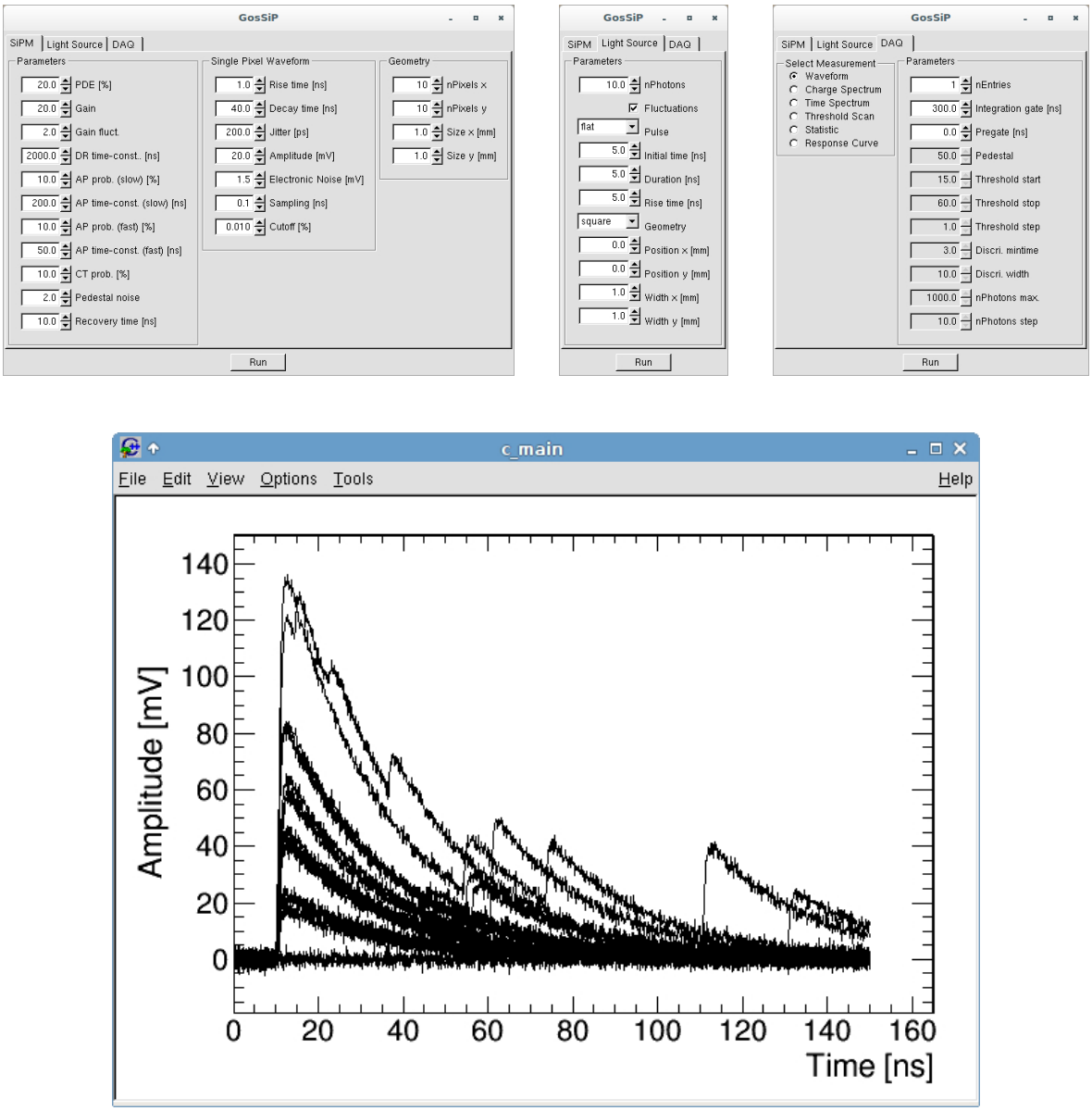

Figure A.2.: GosSiP graphical user interface and example of 20 simulated waveforms.

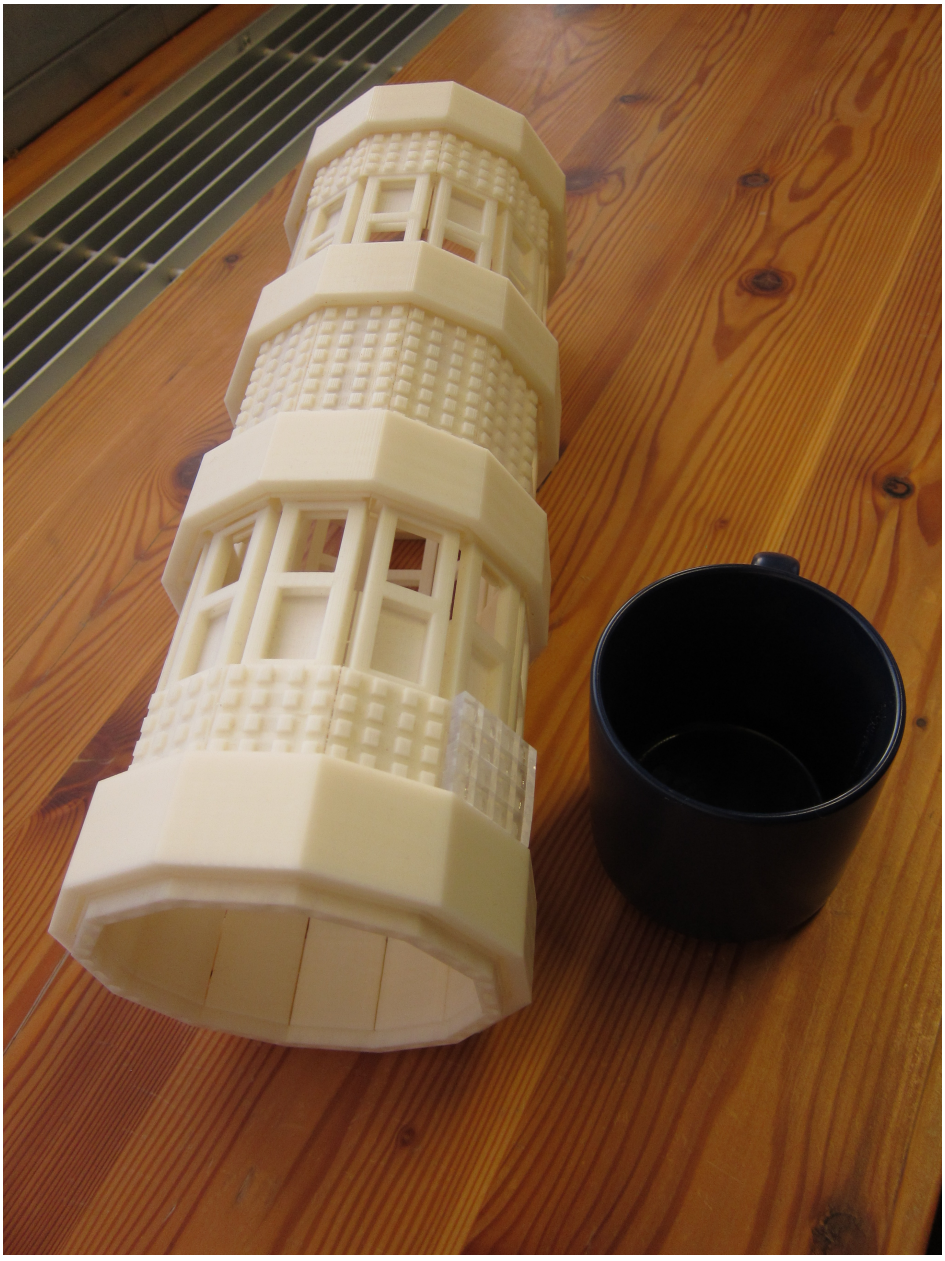

Figure A.3.: Tile Detector mockup based on an early 12-sided design. The tiles, SiPMs and readout boards are only partially shown.

Table A.2.: Tile dimensions for a certain number of tiles in ϕ and z direction.

# Tiles in ϕ Direction (N_ϕ)	40	48	56	64	72
Tile Length [mm]	9.9	8.3	7.1	6.2	5.5
# Tiles in z Direction (N_z)	40	48	56	64	72
Tile Width [mm]	9.0	7.5	6.4	5.6	5.0

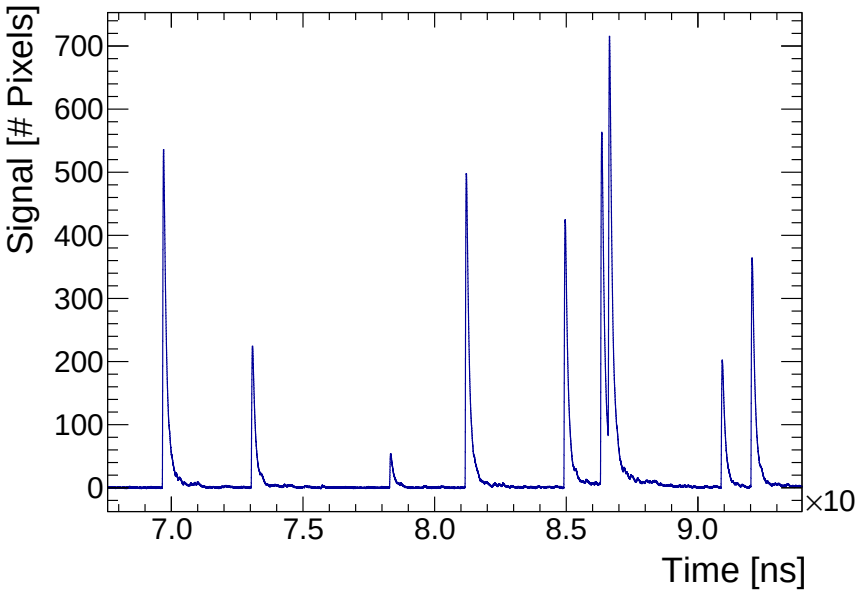

Figure A.4.: Example of a simulated signal of a single channel of the Mu3e Tile Detector.

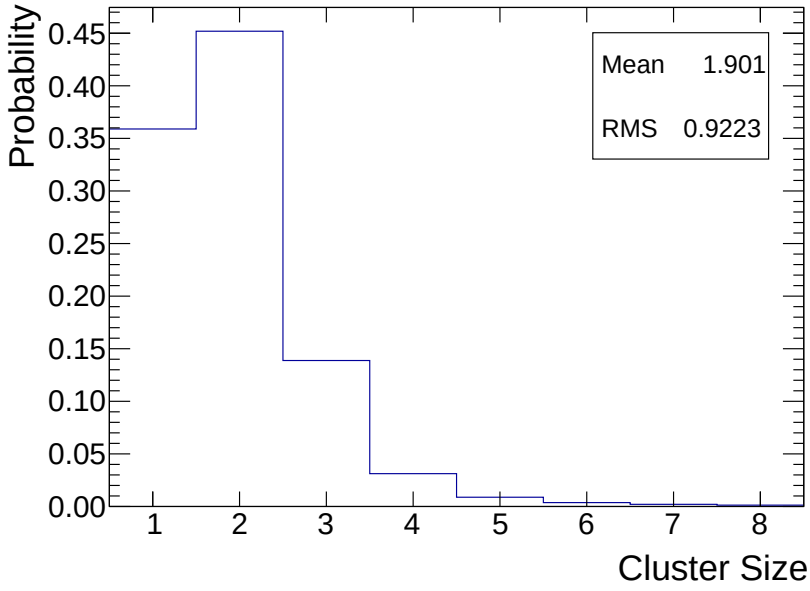

Figure A.5.: Number of tiles in a hit cluser. The average cluster size is about 2.

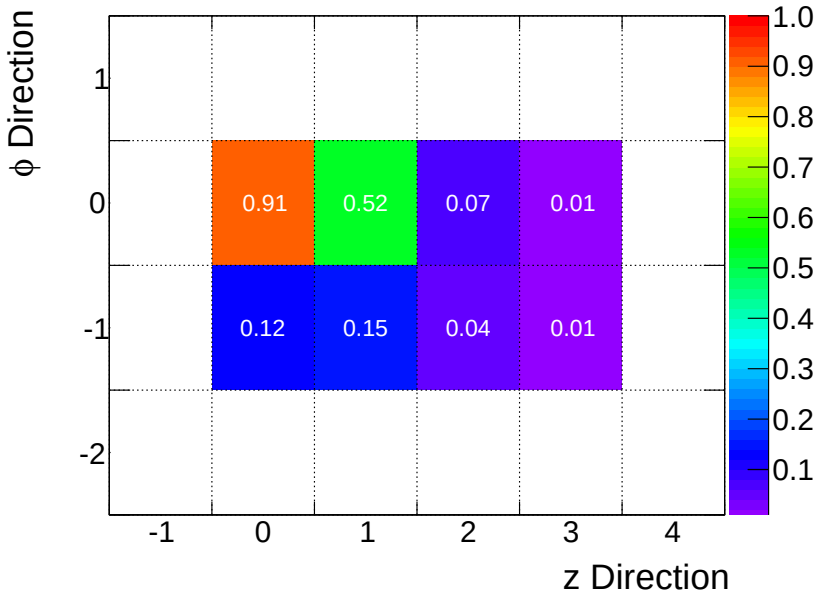

Figure A.6.: Hit cluster: Probability for an e^+ to generate a signal above the detection threshold in a certain channel. The particle impinges at $\phi = 0, z = 0$ with a momentum in z direction. For an electron, the distribution is mirrored along $\phi = 0$, due to the reverse rotational direction.

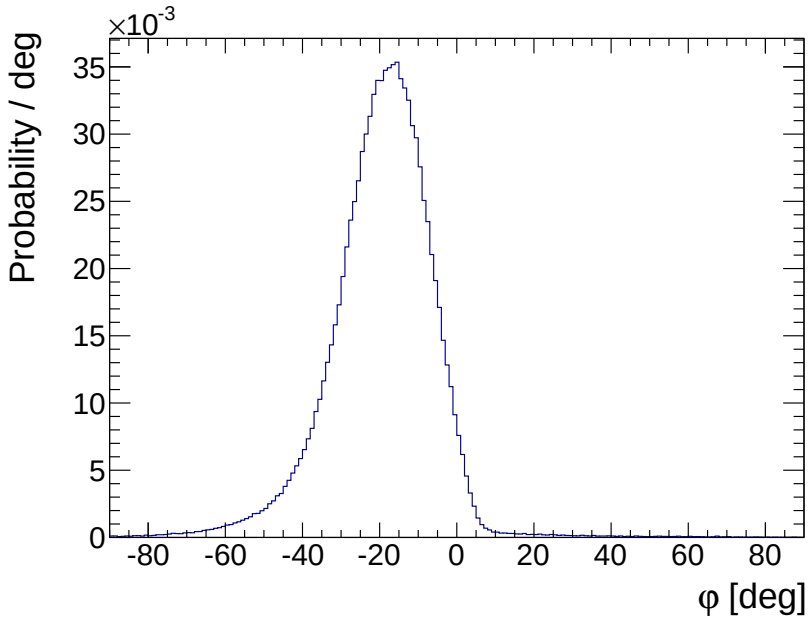

Figure A.7.: Distribution of the impact angel φ of positrons in the Tile Detector. For electrons, the angle has the opposite sign.

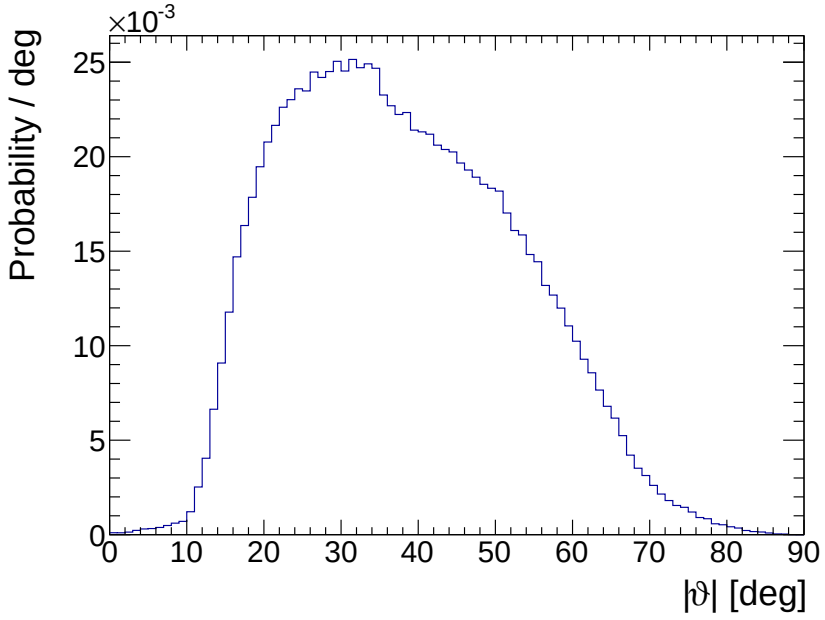

Figure A.8.: Distribution of the impact angel ϑ of positrons in the Tile Detector.

Table A.3.: SiPM input parameters for the simulation of the test-beam measurement.

Parameter	$V_{over} = 1.4\,\mathrm{V}$	$V_{over} = 1.9\,V$
$\mathcal{E}_{pde}\,[\%]$	33.0 ± 0.3	40.0 ± 4.0
$A_{sp}\,[mV]$	0.27 ± 0.03	0.36 ± 0.03
$\sigma_{A_{sp}}/A_{sp}\,[\%]$	9.1 ± 0.2	6.7 ± 0.2
$\tau_{DR}\,[ns]$	566 ± 26	377 ± 18
$\tau_{ap}\,[ns]$	41 ± 2	41 ± 2
$P_{ap}\,[\%]$	15.6 ± 2.0	29.6 ± 2.0
$P_{ct}\,[\%]$	11.0 ± 2.0	15.0 ± 2.0
$\tau_{rise}\,[ps]$	100 ± 20	100 ± 20
$\tau_{dec}\,[ns]$	25 ± 1	25 ± 1
$\tau_{rec}\,[ns]$	10 ± 2	10 ± 2
$\sigma_{en}\,[mV]$	0.45 ± 0.1	0.45 ± 0.1
$\sigma_{av}\,[ps]$	100 ± 50	100 ± 50

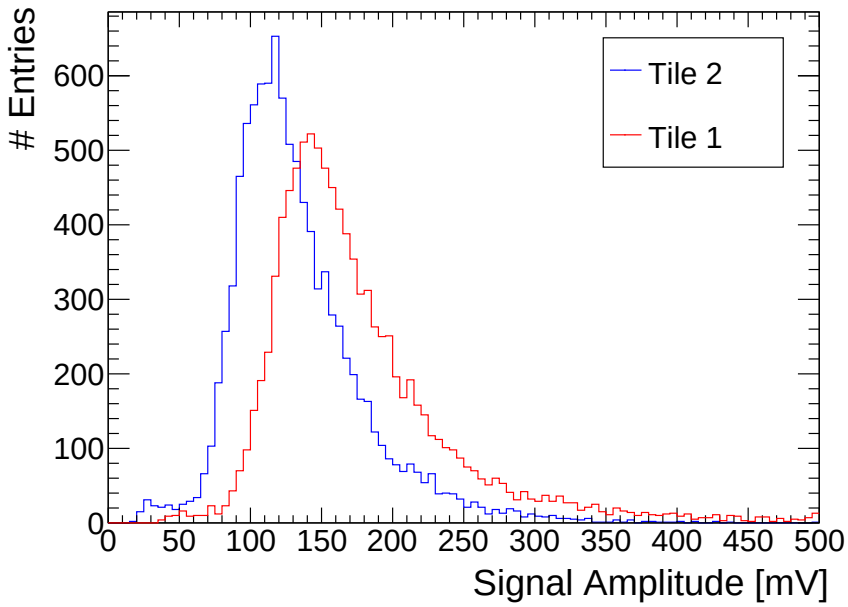

Figure A.9.: Amplitude spectrum for two tiles in response to 3 GeV electrons at the DESY test-beam. The SiPMs are read out with the DRS4 chip.

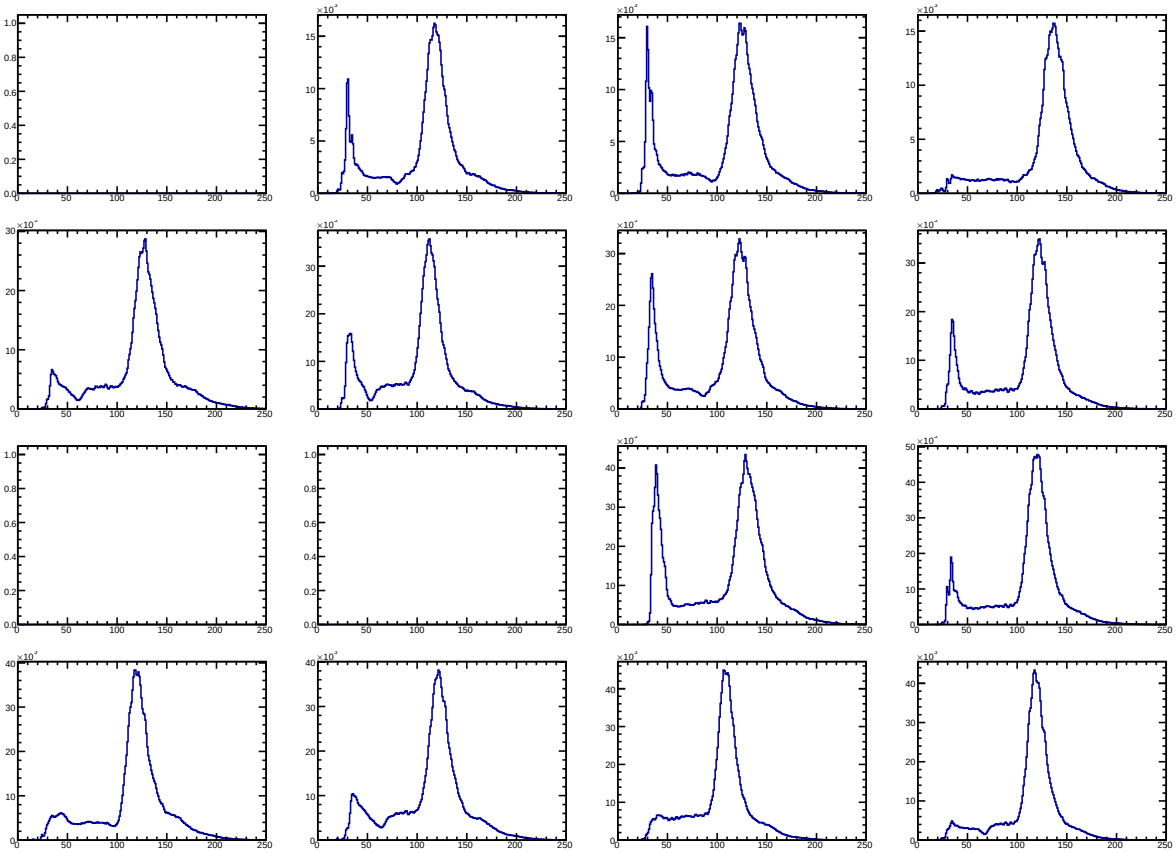

Figure A.10.: Energy spectra for all 16 channels of the tile detector prototype. The x-axis shows the Time-over-Threshold in units of coarse counter bins. The y-axis show the number of entries in the histogram bin.

Table A.4.: STiC settings in the test-beam measurements for data set A,B,C and D

Parameter	Value [Hex]	Parameter	Value [Hex]
GEN IDLE SIGNAL	0	TEMP12 BIT DAC	672
VMON CTL CH0	0	IMON CTL CH0	0
DAC CH0	1f	DAC TTHRESH CH0	6
DAC TBIAS CH0	1	DAC EBIAS CH0	2
DAC ETHRESH CH0	4	LADDER DAC CH0	39
LADDER INPUTBIAS CH0	17	LADDER ICOMP CH0	2d
CHANNEL MASK CH0	0	VMON CTL CH1	0
IMON CTL CH1	0	DAC CH1	1f
DAC TTHRESH CH1	b	DAC TBIAS CH1	5
DAC EBIAS CH1	2	DAC ETHRESH CH1	4
LADDER DAC CH1	39	LADDER INPUTBIAS CH1	17
LADDER ICOMP CH1	2d	CHANNEL MASK CH1	0
VMON CTL CH2	0	IMON CTL CH2	0
DAC CH2	1f	DAC TTHRESH CH2	6
DAC TBIAS CH2	0	DAC EBIAS CH2	2
DAC ETHRESH CH2	4	LADDER DAC CH2	39
LADDER INPUTBIAS CH2	17	LADDER ICOMP CH2	2d
CHANNEL MASK CH2	0	VMON CTL CH3	0
IMON CTL CH3	0	DAC CH3	1f
DAC TTHRESH CH3	8	DAC TBIAS CH3	2
DAC EBIAS CH3	2	DAC ETHRESH CH3	4
LADDER DAC CH3	39	LADDER INPUTBIAS CH3	17
LADDER ICOMP CH3	2d	CHANNEL MASK CH3	0
VMON CTL CH4	0	IMON CTL CH4	0
DAC CH4	1f	DAC TTHRESH CH4	9
DAC TBIAS CH4	1	DAC EBIAS CH4	2
DAC ETHRESH CH4	4	LADDER DAC CH4	39
LADDER INPUTBIAS CH4	17	LADDER ICOMP CH4	2d
CHANNEL MASK CH4	0	VMON CTL CH5	0
IMON CTL CH5	0	DAC CH5	1f
DAC TTHRESH CH5	6	DAC TBIAS CH5	0
DAC EBIAS CH5	2	DAC ETHRESH CH5	4
LADDER DAC CH5	39	LADDER INPUTBIAS CH5	17
LADDER ICOMP CH5	2d	CHANNEL MASK CH5	0
VMON CTL CH6	0	IMON CTL CH6	0
DAC CH6	1f	DAC TTHRESH CH6	9
DAC TBIAS CH6	2	DAC EBIAS CH6	2
DAC ETHRESH CH6	4	LADDER DAC CH6	39
LADDER INPUTBIAS CH6	17	LADDER ICOMP CH6	2d
CHANNEL MASK CH6	0	VMON CTL CH7	0
IMON CTL CH7	0	DAC CH7	1f
DAC TTHRESH CH7	9	DAC TBIAS CH7	2
DAC EBIAS CH7	2	DAC ETHRESH CH7	4
LADDER DAC CH7	39	LADDER INPUTBIAS CH7	17
LADDER ICOMP CH7	2d	CHANNEL MASK CH7	0

Parameter	Value [Hex]	Parameter	Value [Hex]
INDAC	0	CML DAC	0
DISABLE COARSE	0	VMON CTL CH8	0
IMON CTL CH8	0	DAC CH8	1f
DAC TTHRESH CH8	6	DAC TBIAS CH8	0
DAC EBIAS CH8	2	DAC ETHRESH CH8	4
LADDER DAC CH8	39	LADDER INPUTBIAS CH8	17
LADDER ICOMP CH8	2d	CHANNEL MASK CH8	0
VMON CTL CH9	0	IMON CTL CH9	0
DAC CH9	1f	DAC TTHRESH CH9	9
DAC TBIAS CH9	3	DAC EBIAS CH9	2
DAC ETHRESH CH9	4	LADDER DAC CH9	39
LADDER INPUTBIAS CH9	17	LADDER ICOMP CH9	2d
CHANNEL MASK CH9	0	VMON CTL CH10	0
IMON CTL CH10	0	DAC CH10	1f
DAC TTHRESH CH10	6	DAC TBIAS CH10	0
DAC EBIAS CH10	2	DAC ETHRESH CH10	4
LADDER DAC CH10	39	LADDER INPUTBIAS CH10	17
LADDER ICOMP CH10	2d	CHANNEL MASK CH10	0
VMON CTL CH11	0	IMON CTL CH11	0
DAC CH11	1f	DAC TTHRESH CH11	6
DAC TBIAS CH11	0	DAC EBIAS CH11	2
DAC ETHRESH CH11	4	LADDER DAC CH11	39
LADDER INPUTBIAS CH11	17	LADDER ICOMP CH11	2d
CHANNEL MASK CH11	0	VMON CTL CH12	0
IMON CTL CH12	0	DAC CH12	1f
DAC TTHRESH CH12	8	DAC TBIAS CH12	1
DAC EBIAS CH12	2	DAC ETHRESH CH12	4
LADDER DAC CH12	39	LADDER INPUTBIAS CH12	17
LADDER ICOMP CH12	2d	CHANNEL MASK CH12	0
VMON CTL CH13	0	IMON CTL CH13	0
DAC CH13	1f	DAC TTHRESH CH13	9
DAC TBIAS CH13	2	DAC EBIAS CH13	2
DAC ETHRESH CH13	4	LADDER DAC CH13	39
LADDER INPUTBIAS CH13	17	LADDER ICOMP CH13	2d
CHANNEL MASK CH13	0	VMON CTL CH14	0
IMON CTL CH14	0	DAC CH14	1f
DAC TTHRESH CH14	9	DAC TBIAS CH14	2
DAC EBIAS CH14	2	DAC ETHRESH CH14	4
LADDER DAC CH14	39	LADDER INPUTBIAS CH14	17
LADDER ICOMP CH14	2d	CHANNEL MASK CH14	0
VMON CTL CH15	0	IMON CTL CH15	0
DAC CH15	1f	DAC TTHRESH CH15	6
DAC TBIAS CH15	0	DAC EBIAS CH15	2
DAC ETHRESH CH15	4	LADDER DAC CH15	39
LADDER INPUTBIAS CH15	17	LADDER ICOMP CH15	2d
CHANNEL MASK CH15	0	VMON CTL CH16	0

Parameter	Value [Hex]	Parameter	Value [Hex]
IMON CTL CH16	0	DAC CH16	1f
DAC TTHRESH CH16	6	DAC TBIAS CH16	0
DAC EBIAS CH16	2	DAC ETHRESH CH16	4
LADDER DAC CH16	39	LADDER INPUTBIAS CH16	17
LADDER ICOMP CH16	2d	CHANNEL MASK CH16	0
TESTCML DAC	0	SELECT TDCTEST	0
VN D2C	0	VN StampLat	0
VNCntBuffer	0	VNCnt	0
VPCP	0	VNVCODelay	1e
VNVCOBuffer	a	VNHitLogic	0
DAC PFC	0		

Bibliography

[1] Wikipedia, "Woher kommen wir? Wer sind wir? Wohin gehen wir?," 2014.

[2] Wikipedia, "Standard Model," 2014.

[3] P. Ade *et al.*, "Planck 2015 results. XIII. Cosmological Parameters," 2015.

[4] G. Bennett *et al.*, "Measurement of the Negative Muon Anomalous Magnetic Moment to 0.7 ppm," *Phys.Rev.Lett.*, vol. 92, p. 161802, 2004.

[5] R. Pohl, R. Gilman, G. A. Miller, and K. Pachucki, "Muonic Hydrogen and the Proton Radius Puzzle," *Ann.Rev.Nucl.Part.Sci.*, vol. 63, pp. 175–204, 2013.

[6] U. Bellgardt *et al.*, "Search for the Decay $\mu^+ \to e^+e^+e^-$," *Nucl.Phys.*, vol. B299, p. 1, 1988.

[7] A. Blondel, A. Bravar, M. Pohl, S. Bachmann, N. Berger, *et al.*, "Research Proposal for an Experiment to Search for the Decay $\mu \to eee$," 2013.

[8] Y. Fukuda *et al.*, "Evidence for Oscillation of Atmospheric Neutrinos," *Phys.Rev.Lett.*, vol. 81, pp. 1562–1567, 1998.

[9] Q. Ahmad *et al.*, "Measurement of the Rate of $\nu_e + d \to p + p + e^-$ Interactions Produced by ^8B Solar Neutrinos at the Sudbury Neutrino Observatory," *Phys.Rev.Lett.*, vol. 87, p. 071301, 2001.

[10] K. Eguchi *et al.*, "First Results from KamLAND: Evidence for Reactor Anti-Neutrino Disappearance," *Phys.Rev.Lett.*, vol. 90, p. 021802, 2003.

[11] B. Pontecorvo, "Neutrino Experiments and the Problem of Conservation of Leptonic Charge," *Sov.Phys.JETP*, vol. 26, pp. 984–988, 1968.

[12] Z. Maki, M. Nakagawa, and S. Sakata, "Remarks on the Unified Model of Elementary Particles," *Prog.Theor.Phys.*, vol. 28, pp. 870–880, 1962.

[13] A. de Gouvea and P. Vogel, "Lepton Flavor and Number Conservation, and Physics Beyond the Standard Model," *Prog.Part.Nucl.Phys.*, vol. 71, pp. 75–92, 2013.

[14] J. C. Pati and A. Salam, "Lepton Number as the Fourth Color," *Phys.Rev.*, vol. D10, pp. 275–289, 1974.

[15] H. Georgi and S. Glashow, "Unity of All Elementary Particle Forces," *Phys.Rev.Lett.*, vol. 32, pp. 438–441, 1974.

[16] P. Langacker, "Grand Unified Theories and Proton Decay," *Phys.Rept.*, vol. 72, p. 185, 1981.

[17] H. E. Haber and G. L. Kane, "The Search for Supersymmetry: Probing Physics Beyond the Standard Model," *Phys.Rept.*, vol. 117, pp. 75–263, 1985.

[18] R. N. Mohapatra and J. C. Pati, "Left-Right Gauge Symmetry and an Isoconjugate Model of CP Violation," *Phys.Rev.*, vol. D11, pp. 566–571, 1975.

[19] R. Mohapatra and J. C. Pati, "A Natural Left-Right Symmetry," *Phys.Rev.*, vol. D11, p. 2558, 1975.

[20] G. Senjanovic and R. N. Mohapatra, "Exact Left-Right Symmetry and Spontaneous Violation of Parity," *Phys.Rev.*, vol. D12, p. 1502, 1975.

[21] M. Kakizaki, Y. Ogura, and F. Shima, "Lepton Flavor Violation in the Triplet Higgs Model," *Phys.Lett.*, vol. B566, pp. 210–216, 2003.

[22] R. Bayes *et al.*, "Experimental Constraints on Left-Right Symmetric Models from Muon Decay," *Phys.Rev.Lett.*, vol. 106, p. 041804, 2011.

[23] J. Beringer *et al.*, "Review of Particle Physics (RPP)," *Phys.Rev.*, vol. D86, p. 010001, 2012.

[24] Y. Kuno and Y. Okada, "Muon Decay and Physics Beyond the Standard Model," *Rev.Mod.Phys.*, vol. 73, pp. 151–202, 2001.

[25] J. Adam *et al.*, "New Constraint on the Existence of the $\mu^+ \to e^+\gamma$ Decay," *Phys.Rev.Lett.*, vol. 110, p. 201801, 2013.

[26] W. H. Bertl *et al.*, "A Search for Muon to Electron Conversion in Muonic Gold," *Eur.Phys.J.*, vol. C47, pp. 337–346, 2006.

[27] K. Hayasaka, "Tau Lepton Physics at Belle," *Journal of Physics: Conference Series*, vol. 335, no. 1, p. 012029, 2011.

[28] K. Hayasaka *et al.*, "New Search for $\tau \to \mu\gamma$ and $\tau \to e\gamma$ Decays at Belle," *Phys.Lett.*, vol. B666, pp. 16–22, 2008.

[29] B. Aubert *et al.*, "Searches for Lepton Flavor Violation in the Decays $\tau^\pm \to e^\pm\gamma$ and $\tau^\pm \to \mu^\pm\gamma$," *Phys.Rev.Lett.*, vol. 104, p. 021802, 2010.

[30] J. P. Lees *et al.*, "Limits on Tau Lepton-Flavor Violating Decays in Three Charged Leptons," *Phys.Rev.*, vol. D81, p. 111101, 2010.

[31] B. Aubert *et al.*, "Searches for Lepton Flavor Violation in the Decays $\tau \to e\gamma$ and $\tau \to \mu\gamma$," *Phys.Rev.Lett.*, vol. 104, p. 021802, 2010.

[32] B. Aubert *et al.*, "Improved Limits on Lepton Flavor Violating Tau Decays to $\ell\phi$, $\ell\rho$, ℓK^* and $\ell\bar{K}^*$," *Phys.Rev.Lett.*, vol. 103, p. 021801, 2009.

[33] B. Aubert *et al.*, "Search for Lepton Flavour Violating Decays $\tau \to \ell K^0_S$ with the BaBar Experiment," *Phys.Rev.*, vol. D79, p. 012004, 2009.

[34] B. Aubert *et al.*, "Search for Lepton Flavor Violating Decays $\tau^\pm \to \ell^\pm\omega$ $(\ell = e, \mu)$," *Phys.Rev.Lett.*, vol. 100, p. 071802, 2008.

[35] B. Aubert *et al.*, "Search for Lepton Flavor Violating Decays $\tau^{\pm} \to \ell^{\pm}\pi^0, \ell^{\pm}\eta, \ell^{\pm}\eta'$," *Phys.Rev.Lett.*, vol. 98, p. 061803, 2007.

[36] K. Hayasaka *et al.*, "Search for Lepton Flavor Violating τ Decays into Three Leptons with 719 Million Produced $\tau^+\tau^-$ Pairs," *Phys.Lett.*, vol. B687, pp. 139–143, 2010.

[37] Y. Miyazaki *et al.*, "Search for Lepton Flavor Violating τ^- Decays into $\ell^- K_s^0$ and $\ell^- K_s^0 K_s^0$," *Phys.Lett.*, vol. B692, pp. 4–9, 2010.

[38] Y. Miyazaki *et al.*, "Search for Lepton Flavor and Lepton Number Violating tau Decays into a Lepton and Two Charged Mesons," *Phys.Lett.*, vol. B682, pp. 355–362, 2010.

[39] Y. Miyazaki *et al.*, "Search for Lepton-Flavor-Violating Tau Decays into Lepton and $f_0(980)$ Meson," *Phys.Lett.*, vol. B672, pp. 317–322, 2009.

[40] Y. Miyazaki *et al.*, "Search for Lepton Flavor Violating Tau Decays into Three Leptons," *Phys.Lett.*, vol. B660, pp. 154–160, 2008.

[41] Y. Nishio *et al.*, "Search for Lepton-Flavor-Violating $\tau \to \ell V^0$ Decays at Belle," *Phys.Lett.*, vol. B664, pp. 35–40, 2008.

[42] Y. Miyazaki *et al.*, "Search for Lepton Flavor Violating τ^- decays into $\ell^-\eta$, $\ell^-\eta'$ and $\ell^-\pi^0$," *Phys.Lett.*, vol. B648, pp. 341–350, 2007.

[43] Y. Miyazaki *et al.*, "Search for Lepton Flavor Violating Tau-Decays with a K_S^0 Meson," *Phys.Lett.*, vol. B639, pp. 159–164, 2006.

[44] T. Aushev, W. Bartel, A. Bondar, J. Brodzicka, T. Browder, *et al.*, "Physics at Super B Factory," 2010.

[45] T. Abe, "Belle II Technical Design Report," 2010.

[46] F. del Aguila, J. Illana, and M. Jenkins, "Precise Limits from Lepton Flavour Violating Processes on the Littlest Higgs Model with T-parity," *JHEP*, vol. 0901, p. 080, 2009.

[47] F. del Aguila, J. I. Illana, and M. D. Jenkins, "Lepton Flavor Violation in the Simplest Little Higgs Model," *JHEP*, vol. 1103, p. 080, 2011.

[48] E. Arganda and M. J. Herrero, "Testing Supersymmetry with Lepton Flavor Violating Tau and Mu Decays," *Phys.Rev.*, vol. D73, p. 055003, 2006.

[49] M. Hirsch, F. Staub, and A. Vicente, "Enhancing $l_i \to 3l_j$ with the Z^0-Penguin," *Phys.Rev.*, vol. D85, p. 113013, 2012.

[50] H. Dreiner, K. Nickel, F. Staub, and A. Vicente, "New Bounds on Trilinear R-parity Violation from Lepton Flavor Violating Observables," *Phys.Rev.*, vol. D86, p. 015003, 2012.

[51] A. Abada, D. Das, A. Vicente, and C. Weiland, "Enhancing Lepton Flavour Violation in the Supersymmetric Inverse Seesaw Beyond the Dipole Contribution," *JHEP*, vol. 1209, p. 015, 2012.

[52] M. Hirsch, W. Porod, L. Reichert, and F. Staub, "Phenomenology of the Minimal Supersymmetric $U(1)_{B-L} \times U(1)_R$ Extension of the Standard Model," *Phys.Rev.*, vol. D86, p. 093018, 2012.

[53] N. Berger, "Mu3e Simulation and Reconstruction." Talk at the Mu3e Review BVR46, February 2015.

[54] P. Kettle and L. PSI-internal, "Filzbach Meeting," 2010.

[55] I. Peric, "A Novel Monolithic Pixelated Particle Detector Implemented in High-Voltage CMOS Technology," *Nucl.Instrum.Meth.*, vol. A582, pp. 876–885, 2007.

[56] J. B. Birks, "The Theory and Practice of Scintillation Counting," 1964.

[57] F. Sauli, "Instrumentation in High-Energy Physics," 1992.

[58] A. Tadday, *Scintillation Light Detection and Application of Silicon Photomultipliers in Imaging Calorimetry and Positron Emission Tomography.* PhD thesis, Heidelberg University, 2011.

[59] Wikipedia, "Benzene," 2014.

[60] J. B. Birks, "The theory and practice of scintillation counting," 1964.

[61] Wikipedia, "Franck-Condon-Prinzip," 2014.

[62] K. D. Rakes, "Evaluating the response of polyvinyl toluene scintillators used in portal detectors," tech. rep., DTIC Document, 2008.

[63] Saint-Gobain, "Bicron Plastic Scintillation Products Datasheet."

[64] E. Technology, "Plastic Scintillators - Physical and Scintillation Constants."

[65] K. K. Ng, *Complete Guide to Semiconductor Devices.* J Wiley & Sons, 2002.

[66] S. Cova, M. Ghioni, A. Lacaita, C. Samori, and F. Zappa, "Avalanche Photodiodes and Quenching Circuits for Single-Photon Detection," *Applied optics*, vol. 35, no. 12, pp. 1956–1976, 1996.

[67] Hamamatsu, "MPPC Datasheet."

[68] C. Xu, R. Klanner, E. Garutti, and W.-L. Hellweg, "Influence of X-ray Irradiation on the Properties of the Hamamatsu Silicon Photomultiplier S10362-11-050C," 2014.

[69] V. Golovin and V. Savelev, "Novel type of avalanche photodetector with Geiger mode operation," *Nucl.Instrum.Meth.*, vol. A518, pp. 560–564, 2004.

[70] V. Andreev, E. Devitsin, V. Kozlov, P. Smirnov, A. Terkulov, *et al.*, "A High-Granularity Plastic Scintillator Tile Hadronic Calorimeter with APD Readout for a Linear Collider Detector," *Nucl.Instrum.Meth.*, vol. A564, pp. 144–154, 2006.

[71] S. Moehrs, A. Del Guerra, D. J. Herbert, and M. A. Mandelkern, "A Detector Head Design for Small-Animal PET with Silicon Photomultipliers (SiPM)," *Physics in medicine and biology*, vol. 51, no. 5, p. 1113, 2006.

[72] A. Biland, I. Britvich, E. Lorenz, N. Otte, F. Pauss, *et al.*, "First Detection of Air Shower Cherenkov Light by Geigermode-Avalanche Photodiodes," *Nucl.Instrum.Meth.*, vol. A595, pp. 165–168, 2008.

[73] P. Buzhan, B. Dolgoshein, A. Ilyin, V. Kantserov, V. Kaplin, *et al.*, "An Advanced Study of Silicon Photomultiplier," *ICFA Instrum.Bull.*, vol. 23, pp. 28–41, 2001.

[74] S. S. Piatek, "Physics and Operation of an MPPC,"

[75] F. Corsi, A. Dragone, C. Marzocca, P. Delizia, A. Del Guerra, *et al.*, "Modelling a Silicon Photomultiplier (SiPM) as a Signal Source for Optimum Front-End Design," *Nucl.Instrum.Meth.*, vol. A572, pp. 416–418, 2007.

[76] W. Shen, *Development of High Performance Readout ASICs for Silicon Photomultipliers (SiPMs).* PhD thesis, Heidelberg University, 2012.

[77] G. Collazuol, "The Silicon Photo-Multiplier Physics and Technology: A Review," in *Proceedings of the International Workshop on New Photon-detectors (PhotoDet2012). June 13-15, 2012. LAL Orsay, France. Published online at http://pos. sissa. it/cgi-bin/reader/conf. cgi? confid= 158, id. 1*, vol. 1, p. 1, 2012.

[78] K. Arisaka, "New trends in vacuum-based photon detectors," *Nucl.Instrum.Meth.*, vol. A442, pp. 80–90, 2000.

[79] M. A. Green, "Self-Consistent Optical Parameters of Intrinsic Silicon at 300K Including Temperature Coefficients," *Solar Energy Materials and Solar Cells*, vol. 92, no. 11, pp. 1305–1310, 2008.

[80] R. Newman, "Visible Light from a Silicon p-n Junction," *Physical Review*, vol. 100, no. 2, p. 700, 1955.

[81] A. Pifer, T. Bowen, and K. Kendall, "A High Stopping Density mu+ Beam," *Nucl.Instrum.Meth.*, vol. 135, pp. 39–46, 1976.

[82] R. Mirzoyan, R. Kosyra, and H.-G. Moser, "Light Emission in Si Avalanches," *Nuclear Instruments and Methods in Physics Research Section A: Accelerators, Spectrometers, Detectors and Associated Equipment*, vol. 610, no. 1, pp. 98–100, 2009.

[83] S. Cova, A. Lacaita, and G. Ripamonti, "Trapping Phenomena in Avalanche Photodiodes on Nanosecond Scale," *Electron Device Letters, IEEE*, vol. 12, no. 12, pp. 685–687, 1991.

[84] F. Retiere and K. Boone, "Delayed Avalanches in Multi-Pixel Photon Counters," *PoS*, vol. PhotoDet2012, p. 003, 2012.

[85] P. Eckert, "Advanced silicon-photomultiplier characterisation for calorimetric applications," diploma thesis, University of Heidelberg, 2010.

[86] A. Spinelli and A. L. Lacaita, "Physics and Numerical Simulation of Single Photon Avalanche Diodes," *Electron Devices, IEEE Transactions on*, vol. 44, no. 11, pp. 1931–1943, 1997.

[87] A. Lacaita, S. Cova, A. Spinelli, and F. Zappa, "Photon-Assisted Avalanche Spreading in Reach-Through Photodiodes," *Applied physics letters*, vol. 62, no. 6, pp. 606–608, 1993.

[88] A. Lacaita, M. Mastrapasqua, M. Ghioni, and S. Vanoli, "Observation of Avalanche Propagation by Multiplication Assisted Diffusion in p-n Junctions," *Applied physics letters*, vol. 57, no. 5, pp. 489–491, 1990.

[89] K. Yamamoto, K. Yamamura, K. Sato, S. Kamakura, T. Ota, H. Suzuki, and S. Ohsuka, "Development of Multi-Pixel Photon Counter (MPPC)," in *Nuclear Science Symposium Conference Record, 2007. NSS'07. IEEE*, vol. 2, pp. 1511–1515, IEEE, 2007.

[90] G. Collazuol, G. Ambrosi, M. Boscardin, F. Corsi, G. Dalla Betta, A. Del Guerra, N. Dinu, M. Galimberti, D. Giulietti, L. Gizzi, *et al.*, "Single Photon Timing Resolution and Detection Efficiency of the IRST Silicon Photo-Multipliers," *Nuclear Instruments and Methods in Physics Research Section A: Accelerators, Spectrometers, Detectors and Associated Equipment*, vol. 581, no. 1, pp. 461–464, 2007.

[91] C. Piemonte, A. Gola, A. Picciotto, T. Pro, N. Serra, A. Tarolli, and N. Zorzi, "Timing Performance of Large Area SiPMs Coupled to LYSO Using Dark Noise Compensation Methods," in *Nuclear Science Symposium and Medical Imaging Conference (NSS/MIC), 2011 IEEE*, pp. 59–63, IEEE, 2011.

[92] A. Gola, C. Piemonte, and A. Tarolli, "Analog Circuit for Timing Measurements with Large Area SiPMs Coupled to LYSO Crystals," pp. 725–731, 2011.

[93] P. Eckert, R. Stamen, and H. Schultz-Coulon, "Study of the Response and Photon-Counting Resolution of Silicon Photomultipliers using a Generic Simulation Framework," *JINST*, vol. 7, p. P08011, 2012.

[94] S. Agostinelli *et al.*, "GEANT4: A Simulation Toolkit," *Nucl.Instrum.Meth.*, vol. A506, pp. 250–303, 2003.

[95] A. Vacheret, G. Barker, M. Dziewiecki, P. Guzowski, M. Haigh, *et al.*, "Characterization and Simulation of the Response of Multi Pixel Photon Counters to Low Light Levels," *Nucl.Instrum.Meth.*, vol. A656, pp. 69–83, 2011.

[96] S. Sanchez Majos, P. Achenbach, and J. Pochodzalla, "Characterisation of Radiation Damage in Silicon Photomultipliers with a Monte Carlo Model," *Nucl.Instrum.Meth.*, vol. A594, pp. 351–357, 2008.

[97] P. Eckert, H.-C. Schultz-Coulon, W. Shen, R. Stamen, and A. Tadday, "Characterisation Studies of Silicon Photomultipliers," *Nucl.Instrum.Meth.*, vol. A620, pp. 217–226, 2010.

[98] V. Morgunov, "Private discussions."

[99] H. Oide, H. Otono, H. Hano, T. Suehiro, S. Yamashita, *et al.*, "Study of Afterpulsing of MPPC with Waveform Analysis," *PoS*, vol. PD07, p. 008, 2006.

[100] Y. Du and F. Retiere, "After-Pulsing and Cross-talk in Multi-Pixel Photon Counters," *Nucl.Instrum.Meth.*, vol. A596, pp. 396–401, 2008.

[101] H. T. van Dam, S. Seifert, R. Vinke, P. Dendooven, H. Lohner, F. J. Beekman, and D. R. Schaart, "A comprehensive model of the response of silicon photomultipliers," *Nuclear Science, IEEE Transactions on*, vol. 57, no. 4, pp. 2254–2266, 2010.

[102] V. Puill, C. Bazin, D. Breton, L. Burmistrov, V. Chaumat, N. Dinu, J. Maalmi, J. Vagnucci, and A. Stocchi, "Single Photoelectron Timing Resolution of SiPM as a Function of the Bias Voltage, the Wavelength and the Temperature," *Nuclear Instruments and Methods in Physics Research Section A: Accelerators, Spectrometers, Detectors and Associated Equipment*, vol. 695, pp. 354–358, 2012.

[103] S. Butterworth, "On the Theory of Filter Amplifiers," *Wireless Engineer*, vol. 7, pp. 536–541, 1930.

[104] T. E. Linnenbrink, "Waveform Recorder Testing: IEEE Standard 1057 and You," in *Instrumentation and Measurement Technology Conference, 1995. IMTC/95. Proceedings. Integrating Intelligent Instrumentation and Control., IEEE*, p. 241, IEEE, 1995.

[105] Tektronix, "Effective Bits Testing Evaluates Dynamic Performance of Digitizing Instruments."

[106] M. Souders, J. Blair, W. Boyer, *et al.*, "IEEE Std 1057-1994," *IEEE standard for digitizing waveform recorders*, vol. 12, pp. 19–21, 1994.

[107] E.-U. Proposal, "Novel Multimodal Endoscopic Probes for Simultaneous PET/Ultrasound Imaging for Image-Guided Interventions," *European Union 7th*, vol. 186, pp. 2007–2013.

[108] W. Shen, K. Briggl, H. Chen, P. Fischer, A. Gil, T. Harion, M. Ritzert, and H.-C. Schultz-Coulon, "STiC-A Mixed Mode Chip for SiPM ToF Applications," in *Nuclear Science Symposium and Medical Imaging Conference (NSS/MIC), 2012 IEEE*, pp. 877–881, IEEE, 2012.

[109] W. Shen, K. Briggl, H. Chen, P. Fischer, A. Gil, T. Harion, V. Kiworra, M. Ritzert, H.-C. Schultz-Coulon, and V. Stankova, "STiC2-characterization Results of a SiPM Readout ASIC for Time-of-Flight Applications," in *Nuclear Science Symposium and Medical Imaging Conference (NSS/MIC), 2013 IEEE*, pp. 1–5, IEEE, 2013.

[110] T. Harion, K. Briggl, H. Chen, P. Fischer, A. Gil, V. Kiworra, M. Ritzert, H.-C. Schultz-Coulon, W. Shen, and V. Stankova, "STiC—a Mixed Mode Silicon Photomultiplier Readout ASIC for Time-of-Flight Applications," *Journal of Instrumentation*, vol. 9, no. 02, p. C02003, 2014.

[111] S. Ritt, "The DRS Chip: Cheap Waveform Digitizing in the GHz Range," *Nucl.Instrum.Meth.*, vol. A518, pp. 470–471, 2004.

[112] C. Graf, "A Calibration Scheme for the Mu3e Tile Detector," master's thesis, University of Heidelberg, 2015.

[113] M. A. Green and M. J. Keevers, "Optical Properties of Intrinsic Silicon at 300 K," *Progress in Photovoltaics: Research and Applications*, vol. 3, no. 3, pp. 189–192, 1995.

[114] I. Malitson, "Interspecimen Comparison of the Refractive Index of Fused Silica," *JOSA*, vol. 55, no. 10, pp. 1205–1208, 1965.

[115] C. Licciulli, "Präzise Zeitmessung für das Mu3e-Experiment," master's thesis, University of Heidelberg, 2013.

[116] A. Artikov, J. Budagov, I. Chirikov-Zorin, D. Chokheli, M. Lyablin, G. Bellettini, A. Menzione, S. Tokar, N. Giokaris, and A. Manousakis-Katsikakis, "Properties of the Ukraine Polystyrene-Based Plastic Scintillator UPS 923A," *Nuclear Instruments and Methods in Physics Research Section A: Accelerators, Spectrometers, Detectors and Associated Equipment*, vol. 555, no. 1, pp. 125–131, 2005.

[117] H. Blumenfeld and M. Bourdinaud, "Aging of Plastic Scintillating Fibers," *Applied optics*, vol. 31, no. 15, pp. 2791–2795, 1992.

[118] T. Harion, *Development and Commissioning of STiC (Working Title)*. PhD thesis, Heidelberg University, 2015 (TBP).

[119] K. Yamamoto, K. Yamamura, K. Sato, S. Kamakura, T. Ota, *et al.*, "Newly Developed Semiconductor Detectors by Hamamatsu," *PoS*, vol. PD07, p. 004, 2006.

Danksagung

Ich möchte mich hier bei allen Personen bedanke, die mich bei dieser Arbeit unterstützt haben. An erster Stelle will ich mich bei meinem Doktorvater Herrn Prof. Hans-Christian Schultz-Coulon bedanken, der mir diese Arbeit ermöglicht hat: Vielen Dank für die Unterstützung, das entgegengebrachte Vertrauen und die tolle Arbeitsatmosphäre!
Herrn Prof. Peter Fischer danke ich für die Bereitschaft als Zweitgutachter zur Verfügung zu stehen.
Bei meine Kollegen Tobias, Konrad, Christian, Wei, Huangshan, Vera, Yonathan und der ganzen ATLAS Gruppe will ich mich herzlich bedanken für die tolle Zeit, aufschlussreiche fachspezifische und unspezifische Diskussionen und packende Kickerpartien.
Des Weiteren möchte ich mich bei der ganzen Mu3e Kollaboration bedanken, insbesondere der Gruppe von Prof. André Schöning und Prof. Niklaus Berger, die mich herzlich in die Kollaboration aufgenommen haben. Vielen Dank für die tolle Zusammenarbeit - insbesondere auch bei den Test-beam Kampagnen.
Weiterhin bedanke ich mich besonders bei allen die diese Arbeit Korrektur gelesen haben: Dr. Rainer Stamen, Dr. Monica Dunford, Alessandra Baas, Tobias Harion, und Dr. Veit Scharf.
Ein besonderer Dank geht an meine Familie, die mich schon immer mit viel Liebe und Ruhe Unterstützt hat.
Zum Schluss möchte ich mich bei meiner Freundin Alessandra bedanken, die mich in der Schlussphase dieser Arbeit tapfer ertragen hat und durch die meine Promotionszeit zu etwas Besonderem wurde.